ANNUAL REPORT 1999

DEPARTMENT
OF
OPTOELECTRONICS

UNIVERSITY OF ULM

Contents

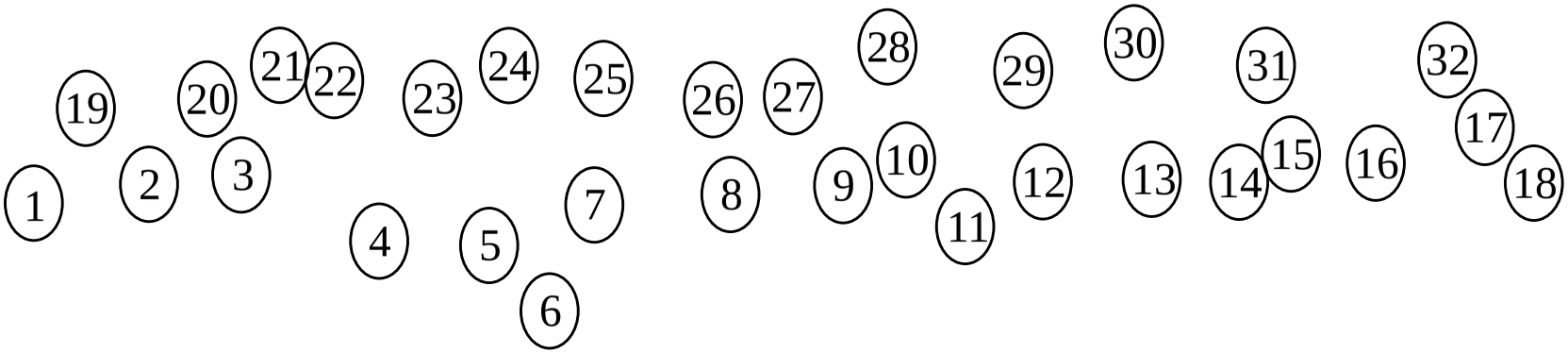

1: Peter Unger
2: Martin Grabherr
3: Matthias Golling
4: Susanne Döttinger
5: Irene Ecker
6: Sükran Kilic
7: Thomas Knödl
8: Marcus Scherer
9: Markus Kamp
10: Veit Schwegler
11: Sophie Pfetsch
12: Frank Demaria
13: Jürgen Joos
14: Josef Theisz
15: Christoph Kirchner
16: Jürgen Mähnß
17: Georgi Stareev
18: Safwat William Zaki Mahmoud
19: Christine Bunk
20: Ulrich Martin
21: Felix Mederer
22: Eckhard Deichsel
23: Hin Yiu Anthony Chung
24: Roland Jäger
25: Karl Joachim Ebeling
26: Wolfgang Schmid
27: Michael Wang
28: Roger King
29: Max Kicherer
30: Matthias Seyboth
31: Selim Ünlü
32: Hansjörg Wolf

Department of Optoelectronics
University of Ulm

Albert-Einstein-Allee 45, D-89069 Ulm, Germany
Fax: +49–731/50–2 60 49
Phone: +49–731/50–

Head of Department:

Prof. Dr.	Karl Joachim Ebeling	–2 60 51	karl.ebeling@e-technik.uni-ulm.de

Assistant Head of Department:

Prof. Dr.	Peter Unger	–2 60 54	peter.unger@e-technik.uni-ulm.de

Senior Research Assistant:

Dr.-Ing.	Rainer Michalzik	–2 60 48	rainer.michalzik@e-technik.uni-ulm.de

Cleanroom Management:

Dr.-Ing.	Jürgen Mähnß	–2 60 53	juergen.maehnss@e-technik.uni-ulm.de

Guest Scientist:

Prof. Dr.	Selim Ünlü	–2 64 54	unlu.selim@e-technik.uni-ulm.de

Secretaries:

	Christine Bunk	–2 60 50	christine.bunk@e-technik.uni-ulm.de
	Sükran Kilic	–2 60 59	suekran.kilic@e-technik.uni-ulm.de

Research Staff:

Dr.-Ing.	Hin Yiu Anthony Chung	–2 61 95	hin-yin.chung@e-technik.uni-ulm.de
Dipl.-Ing.	Eckard Deichsel	–2 60 57	eckard.deichsel@e-technik.uni-ulm.de
Dipl.-Ing.	Frank Demaria	–2 60 46	frank.demaria@e-technik.uni-ulm.de
Dipl.-Ing.	Irene Ecker	–2 60 41	irene.ecker@e-technik.uni-ulm.de
Dipl.-Ing.	Matthias Golling	–2 60 35	matthias.golling@e-technik.uni-ulm.de
Dipl.-Ing.	Martin Grabherr	–2 60 43	martin.grabherr@e-technik.uni-ulm.de
Dipl.-Phys.	Roland Jäger	–2 60 40	roland.jaeger@e-technik.uni-ulm.de
Dipl.-Ing.	Jürgen Joos	–2 60 35	juergen.joos@e-technik.uni-ulm.de
Dr.rer.nat.	Markus Kamp	–2 64 54	markus.kamp@.e-technik.uni-ulm.de
Dipl.-Phys.	Max Kicherer	–2 60 37	max.kicherer@e-technik.uni-ulm.de
Dipl.-Ing.	Roger King	–2 60 40	roger.king@e-technik.uni-ulm.de
Dipl.-Ing.	Christoph Kirchner	–2 60 39	christoph.kirchner@e-technik.uni-ulm.de
Dipl.-Ing.	Thomas Knödl	–2 60 38	thomas.knoedl@e-technik.uni-ulm.de
M.S.	Safwat William Mahmoud	–2 60 44	safwat.mahmoud@e-technik.uni-ulm.de
Dipl.-Ing.	Ulrich Martin	–2 60 46	ulrich.martin@e-technik.uni-ulm.de
Dipl.-Ing.	Felix Mederer	–2 60 37	felix.mederer@e-technik.uni-ulm.de
Dipl.-Phys.	Michael Miller	–2 60 36	michael.miller@e-technik.uni-ulm.de
Dipl.-Ing.	Marcus Scherer	–2 61 95	marcus.scherer@e-technik.uni-ulm.de
Dipl.-Ing.	Wolfgang Schmid	–2 60 44	wolfgang.schmid@e-technik.uni-ulm.de
Dipl.-Ing.	Veit Schwegler	–2 64 52	veit.schwegler@e-technik.uni-ulm.de
Dipl.-Phys.	Matthias Seyboth	–2 64 52	matthias.seyboth@e-technik.uni-ulm.de
Dr.-Ing.	Georgi Stareev	–2 61 95	georgi.stareev@e-technik.uni-ulm.de
Dipl.-Ing.	Heiko Johannes Unold	–2 60 36	heiko.unold@e-technik.uni-ulm.de
PhD.	Michael Wang	–2 64 52	chengxin.wang@e-technik.uni-ulm.de

Technical Staff:

Susanne Döttinger	–2 60 38	susanne.doettinger@e-technik.uni-ulm.de
Susanne Menzel	–2 60 41	
Sophie Pfetsch	–2 60 41	sophie.pfetsch@e-technik.uni-ulm.de
Josef Theisz	–2 60 30	
Hansjörg Wolf	–2 60 39	hansjoerg.wolf@e-technik.uni-ulm.de

Preface

On December 18, 1999, together with the traditional Christmas Party, the Optoelectronics Department celebrated its 10th anniversary. Susanne Menzel and Sophie Pfetsch tried to invite all former members of the institute and we were happy that so many old faces showed up bringing up the crowd to above 120 people attending. It is worthwhile to mention that at the end of 1999 in total 25 students of the Department received their Ph.D. degree in Engineering Sciences. This figure precisely corresponds to one third of the total number of Ph.D. degrees granted by the Faculty of Engineering Sciences since its foundation in 1989.

The year 1999 was another exciting one for the Department. In February and March we had the pleasure of having Katsumi Kishino from Sophia University Tokyo as a distinguished Guest Professor in our group. He helped us a lot in our red laser diode activities and besides gave very nice seminars on short wavelength lasers and related material growth issues. In April the whole Department was busy for quite some days to host the Third Annual Meeting of the European Community MEL-ARI Program. In March Rainer Michalzik left us for one year to become a visiting member technical staff at Lucent´s Bell Laboratories in Holmdel, New Jersey, USA. At the end of June he came back on a short trip to receive the distinguished young scientist Heinz Maier-Leibnitz Award of the German Science Foundation.

Susanne Döttinger and Hansjörg Wolf joined our technical staff partly replacing Rudolf Rösch who left us for helping a start-up enterprise. We like to thank Rudi for his skilled support. In September Michael Wang came as a guest scientist. Seven members of the Department, Jörg Heerlein, Christian Jung, Hin Yiu Anthony Chung, Dieter Wiedenmann, Bernhard Weigl, Jochen Heinrich, and Arthur Pelzmann received their Ph.D. degrees. Five diploma theses and nine semester projects were completed.

Maybe due to our not too unsuccessful work, research funding by various organizations has continued in a generous manner. As a special, with kind support from the Ministry of Science and Technology and the Aixtron Company Aachen, a hydride vapor phase epitaxy system was installed to start growth of free-standing GaN substrates. Last year's research highlights included record 45% external quantum efficiency of batch fabricated LEDs as well as further improvements of GaN LED efficiency and breakthroughs in high-power, edge-emitting and vertical-cavity laser diodes. Furthermore, our early work on 10 Gbit/s data transmission using VCSEL sources has been recognized as an important milestone for future high bit rate datacom links.

It is believed that with the portfolio at hand and the background established the Department is in an excellent position to face future challenges.

The 10-year anniversary Department Christmas Song can be found at the end of this booklet.

Karl Joachim Ebeling January 2000

Hydride Vapour Phase Epitaxy Growth of High Quality thick GaN Layers

Hin Yiu Anthony Chung and Chengxing Michael Wang

In this article, the AIXTRON Low Pressure Hydride Vapour Phase Epitaxy (LP-HVPE) system will be presented. First results show that the HVPE grown GaN layers exhibit excellent electrical, crystallographical and optical qualities. In our work, we successfully use reduced pressure for the growth. A decisive improvment of the background doping (down to 2 $\times 10^{16}$ cm^{-3}) and Hall-mobility (up to 300 cm^2/Vs) is observed. Experiments on the growth of thick ($>$ 200 μm in thickness) free-standing GaN layers and MOVPE over-growth on HVPE GaN layers will also be presented.

1. Introduction

Due to the lack of a suitable substrate, growth and processing of GaN-based devices still has to face major difficulties in High-End productions. The HVPE growth with its high growth rate (up to 100 μm/h) appears to be a very attractive technique for the production of high quality, large diameter and thick GaN layers ($>$ 200 μm in thickness), which can eventuelly be used as free-standing substrates. For the HVPE process development, an AIXTRON Low Pressure HVPE system was installed in march 1999. Up to now a vast amount of experiments have been carried out showing the reliability of the system.

In the first part of our work, we concentrated on the optimization of epitaxial growth of 10 to 20 μm thick GaN layers on MOVPE grown GaN/sapphire templates. HVPE GaN layers showing high electrical, optical and crystallographical qualities are obtained. After these first expriments, the growth of thick and free-standing GaN layers has been initiated. So far, free-standing GaN layers with thickness of 230 μm, and area of up to 10 mm^2 has been achieved.

In order to investigate the possibility of using our HVPE GaN layers as substrate materials for GaN-based lasers, over-growth experiments have been carried out. 2 μm thick GaN is grown on HVPE GaN layer by MOVPE and characterised by low temperature photoluminesence (LT-PL). The PL-spectra reveal all three free exciton levels (FE A, FE B and FE C) without any visible bound excitons. This result clearly shows that high quality MOVPE GaN layers can be obtained by using our HVPE layers as substrate.

2. The epitaxy System

In fig. 1 the reactor of the HVPE system is depicted schemetically. The reactor can be divided into two different zones: the source zone and the growth zone. The whole reactor is surrounded by five heating elements whose temperatures can be regulated independently. Process gases HCl and NH_3 are injected into the reactor through the source zone. As carrier gas, pure N_2 is used. In the source zone, where the working temperature is typically around 860 ^{0}C, HCl is allowed to pass over a crucible containing metallic Ga. At this high temperature, HCl reacts with the Ga and GaCl is formed. Through a shower-head, the resulting GaCl will then be transported down-stream to the growth zone. In the growth zone, GaCl and NH_3 come into reaction on the surface of the substrate and GaN is formed according to the following reaction:

$$GaCl + NH_3 \longleftrightarrow GaN + HCl + H_2$$

The substrates used in all the experiments are c-plane Sapphire wafers covered by 1.5 to 2 μm thick MOVPE GaN layers. The maximum diameter of the substrates used is two inch. The substrate is placed on a rotatable quartz disk mounted on the susceptor. A rotatry pump, installed down-stream of the reactor, enables the system to be evalcuated down to a pressure of 5×10^{-4} mbar.

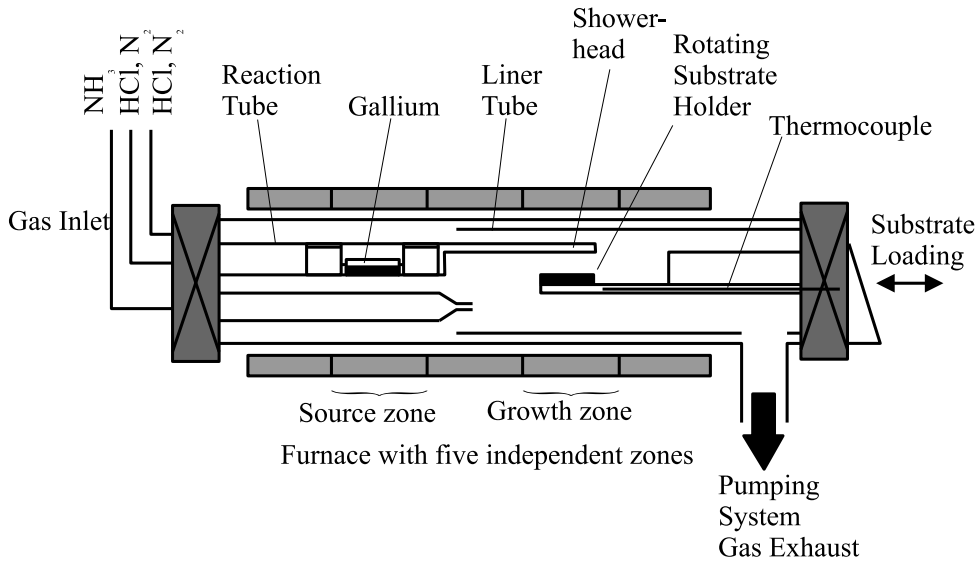

Fig. 1. Schematic diagram of the HVPE reactor of AIXTRON AG

3. Epitaxial growth under various reactor pressures

One of the main problems in GaN HVPE is the parasitic deposition on the reactor wall by NH_4Cl. NH_4Cl deposition generates particles in the reactor which massively hinder the growth

of high quality layers. We observe, however, that by reducing the reactor pressure down to 250 mbar, the NH_4Cl deposition can be reduced significantly. However, very few reports have been published concerning the influences of the reactor pressure on HVPE GaN processes. In order to investigate the impact of reactor pressure on the qualities of HVPE layers, 10 to 20 μm thick GaN layers have been grown under various reactor pressures and are characterized .

The epitaxial growths are carried out with substrate temperatures around 1000 ^{0}C. The flow rates of HCl passing over the Ga melt are chosen to be around 20 sccm. The NH_3 flows are $1\mathrm{l}/\mathrm{min}$ and the total flow rates are around 5 l/min. In our work, the reactor pressures 950 mbar, 550 mbar and 250 mbar are chosen. In fig.2, the background free carrier concentration and the carrier Hall-mobilities are shown as a function of the reactor pressure. By reducing the pressure, a clear reduction of the free carrier concentration can be observed. With the pressure 250 mbar we achieve a free carrier concentration of 2×10^{16} cm^{-3}. The Hall-mobility is found to increase with decreasing reactor pressure. Layers grown at 250 mbar show a Hall-mobility of up to 300 cm^2/Vs (see fig. 3) indicating the high electrical quality of the layers.

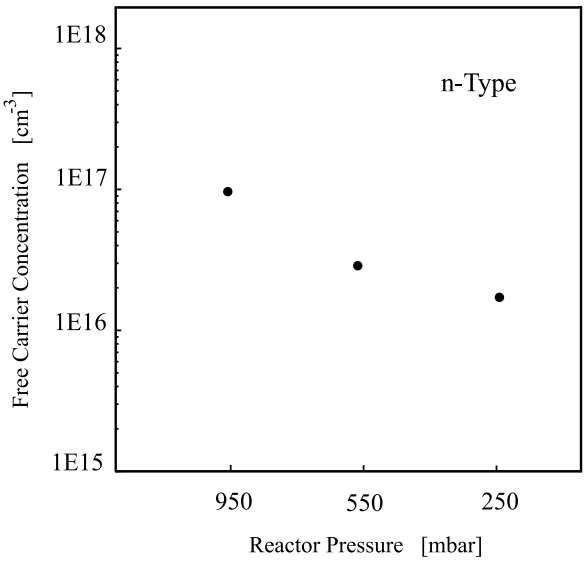

Fig. 2. Room temperature free carrier concentrations of GaN layers grown under various reactor pressures. The layers have thicknesses of 20 μm. The growth rates were between 10 to 20 μm/h and the growth temperature was 1050 ^{0}C.

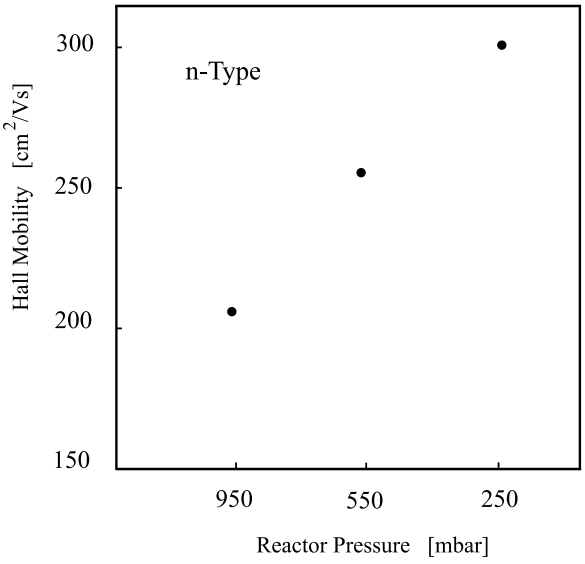

Fig. 3. Room temperature carrier Hall mobilities of GaN layers grown under various reactor pressures. All layers have thickness of 20 μm. The growth rates were between 10 to 20 μm/h and the growth temperature was 1050 ^{0}C.

High resolution X-ray diffraction has been carried out to investigate the crystallographical quality of the GaN layers. For our investigation, the $Cu_{K\alpha 1}$ line is used. Fig.4 shows the FWHM of the (0002) peak of GaN layers grown under various reactor pressures.
A slight improvement of the FWHM, and therefore the crystal quality of the layers, can been seen by reducing the reactor pressure. The minimum FWHM, achieved at 250 mbar, is around 230 arc sec. In contrast to the electrical and crystal quality, no significant change in optical

quality has be found in the GaN layers grown under different reactor pressures. The low temperature photoluminesence spectrum of the layers show roughly the same features irrespective of the applied reactor pressure. In fig. 5, a typical 16 K PL-spectrum is shown. The spectrum is dominated by an intense D^0X peak. On the high energy side of the D^0X peak a shoulder corresponding to the free exciton level FE A can be recognised. On the low energy side of the spectrum, phonon-replica of the D^0X level and of the step dislocation level (L) can also be seen clearly. The appearance of the FE A level shows that the optical quality of the GaN layer is rather high. The phonon-replica indicate that the GaN layer is compact.

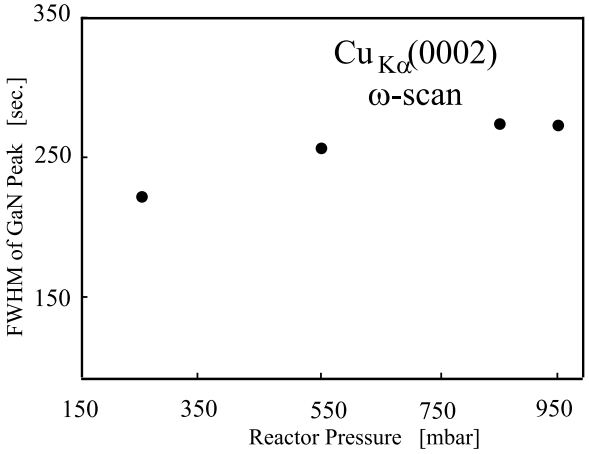

Fig. 4. Full width at half maximum of the (0002) peak of 20 μm thick GaN layers grown under various reactor pressures. The growth rate was around 20 μm/h and the growth temperature was 1050 ^{0}C.

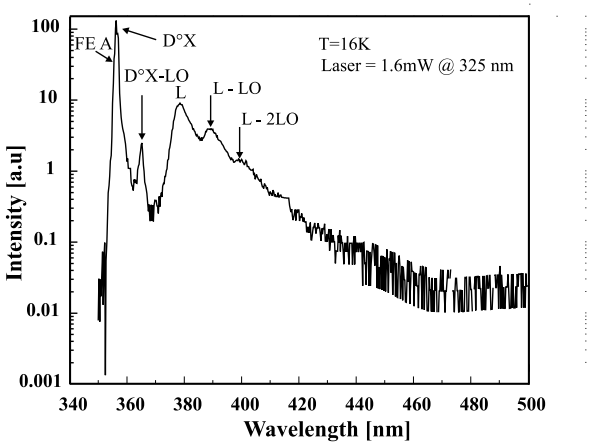

Fig. 5. Typical low temperature photoluminesence spectrum of 20 μm thick GaN layers grwon under reduced reactor pressure. The growth rate was around 20 μm/h and the growth temperature was 1050 ^{0}C.

4. Growth of thick GaN layers (Thickness $>$ 200μm)

The goal of our HVPE GaN activities is the growth of GaN substrates. These substrate layers should have thicknesses above 100 μm in order to garantee mechanical stability. First GaN layers with thicknesses of 230 μm have been grown by the HVPE system and optically characterized by LT-PL. These layers are grown with a growth rate of up to 60 μm/h and with a reactor pressure of 250 mbar. Owning to the high stress between the thick GaN layer and the Sapphire substrate, the layer lifted off from the Sapphire and pieces of GaN films formed. So far, the maximum size of the pieces is around
10 mm^2. Fig.6 shows the SEM micrograph of a GaN film with a thickness of 230 μm. With the exception of the rim region, this piece of GaN is nearly free of cracks. The optical quality of the pieces are investigated by LT-PL. In fig. 7, a typical 16 K PL-Spectrum of the GaN pieces is shown. The spectrum is dominated by an intense D^0X peak with a FWHM of 4 meV. On the high energy side of the D^0X, a shoulder can be observed. This shoulder may correspond to the free exciton level FE A. On the low energy side of the spectrum, numerous peaks can also be

observed. The identity of those peaks is still under investigation. The intense D^0X peak and the appearance of the FE A level, however, strongly indicate that the optical quality of the pieces is very high.

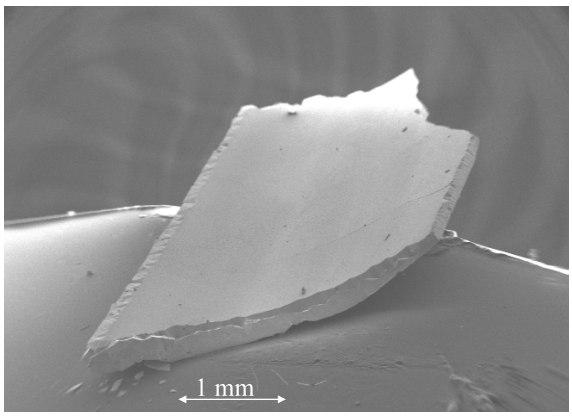

Fig. 6. SEM micrograph of a 230 μm thick free-standing GaN layer. The size of the layer is around 10 mm^2.

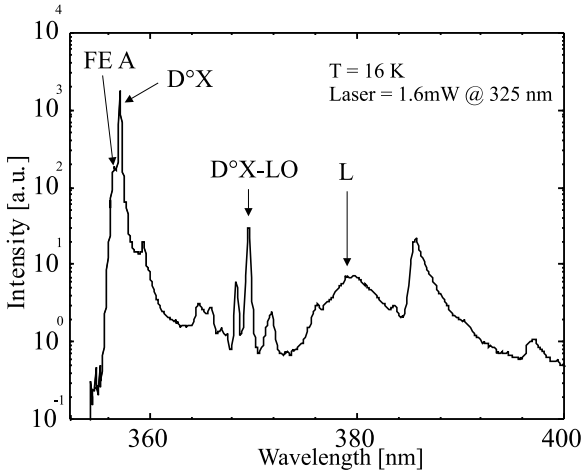

Fig. 7. Low temperature photoluminesence spectrum of a 230 μm thick free-standing GaN layer.

5. MOVPE overgrowth of HVPE GaN layers

To evaluate the suitability of using the HVPE GaN layers as substrate material, 2 μm thick undoped GaN layers are grown on HVPE GaN quasi-substrates by MOVPE. For the MOVPE growth, standard growth parameters which are routinely used for manufacturing LED devices are applied. The optical quality of the over-grown MOVPE layers are characterized by LT-PL. Typical PL spectra measured under various temperatures are shown in fig. 8. All the spectra reveal all three free exciton levels (FE A, FE B and FE C) without showing any trace of bound exciton peaks. This optical quality of the over-growth MOVPE layer is at least as good as those of the best layers grown directly on sapphire.

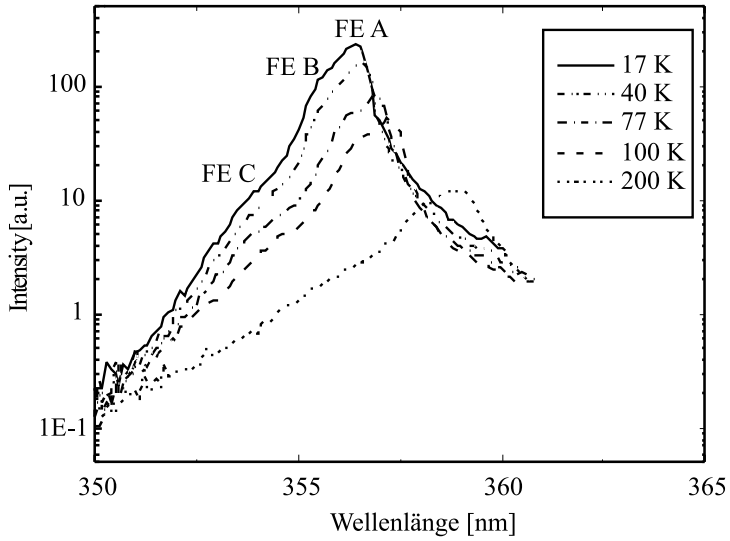

Fig. 8. Temperature dependent photoluminesence spectra of MOVPE GaN layer over-grown on HVPE GaN; In all the spectra, the free exciton levels FE A, FE B and FE C can be observed.

6. Conclusion

In summary, within 9 months we have successfully installed a HVPE system for GaN Growth. We optimized the growth parameters and obtained high quality GaN layers under reduced reactor pressure. These layers show low background carrier concentrations, high carrier Hall mobilities, high optical and crystallographical qualities. 10 mm^2 large and 230 μm thick GaN layers have been successfully grown and characterized. These layers show very good optical quality and contain nearly no cracks. To investigate the suitability of using the HVPE GaN layers as substrate material, experiments on MOVPE over-growth on HVPE layers have been carried out. LT-PL shows that the over-growth MOVPE layers are of excellent optical quality. The results in this report show that the approach of using thick HVPE GaN layers as substrate material for the GaN technology is very promising.

7. Acknowledgement

This work is financed by AIXTRON AG Aachen under the project *Entwicklung massiver GaN Quasi-Substrate* of the German Bundesministerium für Bildung, Wissenschaft und Forschung. The authors would like to thank the support from the EPFL Switzerland and Osram OS Regensburg.

Low Resistance Ohmic Contacts to p-type GaN

Marcus Scherer and Veit Schwegler

To reduce the contact resistance for p-type GaN three different approaches have been investigated. Wet chemical treatment was established to remove the surface oxide and different metal systems as well as the influence of contact annealing were examined. As a significant value for good ohmic contacts, the specific contact resistance was determined from TLM measurements.

1. Introduction

In recent years, a wide range of electrical and optical devices based on galliumnitride (GaN) have been demonstrated [1]. Above all, optical devices such like light-emitting diodes (LEDs) and laser diodes (LDs) are still limited in output power and lifetime due to internal heating. One reason therefore is the low p-type conductivity and as a consequence thereof the poor contact resistances of p-contacts.

2. Experimental

The III-V nitride films used in this study were grown in a horizontal MOVPE reactor on c-plane sapphire substrates. First, a 2 μm thick undoped GaN buffer was grown, followed by a 0.3 μm Mg-doped GaN layer. After activation in a rapid thermal annealer (RTA) at 800 °C for 10 min, the p-concentration was determined to be $3 \cdot 10^{17}$ cm^{-3} by Hall measurements. The contacts were characterized with a 4-probe setup using a HP4145B Semiconductor Parameter Analyzer and the specific contact resistances (ρ_c) were determined by transmission line method (TLM) [2]. The active region for the TLM structures was fabricated with chemically-assisted ion-beam etching (CAIBE) using Cl_2. The metal contacts were deposited by electron beam evaporator and patterned by lift-off technique. The interspacing between the contact pads varied from 10 to 320 μm.

To examine the influence of surface treatment on the contact resistance four different types of samples were prepared. The first one was left untreated, a second immersed into boiling HCl solution. Another sample was prepared by immersing into room temperature (RT) aqua regia (HCl:HNO_3 = 3:1) and the fourth set was dipped into NH_4F for 10 min. All wet chemical treatment was done right before depositing Ni/Au contacts (20/180 nm). In addition, Pd/Au contacts of the same layer thickness were investigated. To show the influence of thermal treatment on contact resistances, the samples were annealed under nitrogen atmosphere for 10 min with temperatures ranging from 350 °C to 650 °C.

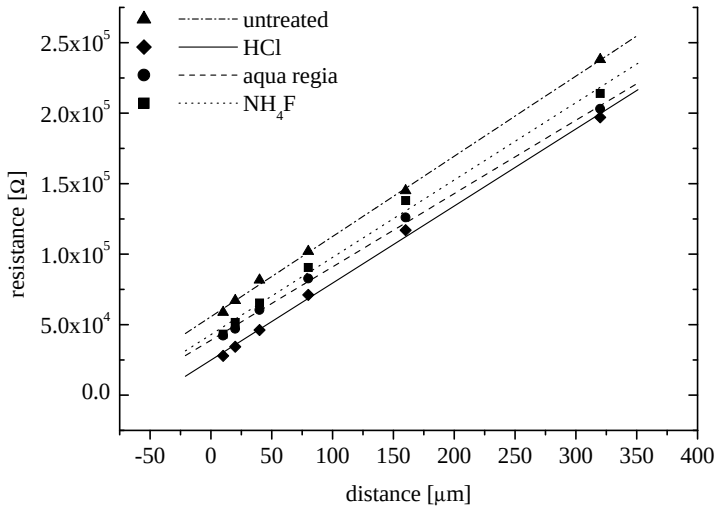

Fig. 1. Comparison of TLM-measurements with the type of surface treatment.

3. Results and Discussion

IV-characteristics of the as deposited Ni/Au-contacts show ohmic behaviour and no influence of the surface treatment is determined. But in TLM measurements, a significant reduction of contact resistance can be seen (Fig. 1). The specific contact resistance is reduced from 1.69 Ωcm^2 for the untreated sample to 0.15 Ωcm^2 for the HCl-immersed one. This improve is due to removal of transparent organic and inorganic contaminations and surface oxid that forms during air exposure [3]. The parallel slope of the regression lines shows clearly, that there is no influence of the wet chemical treatment on the sheet resistance of the semiconductor. All of the further investigated samples were dipped into boiling HCl for 5 min before metal deposition.

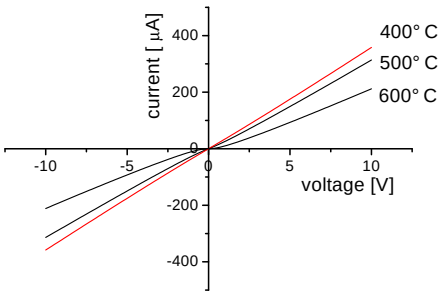

Fig. 2. IV-data of Ni/Au contacts for a contact pad distance of 160 μm.

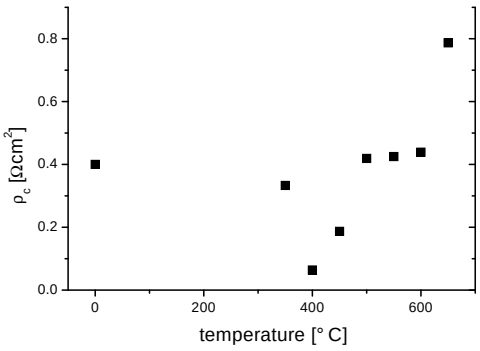

Fig. 3. Specific contact resistances of various heat-treated Ni/Au contacts.

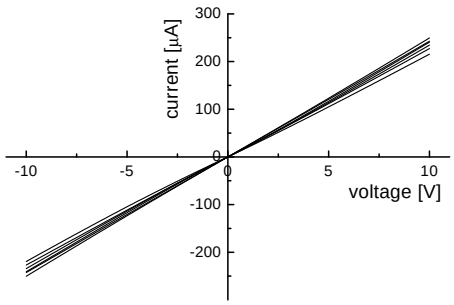

Fig. 4. IV-characteristics of Pd/Au contacts for different anneal temperatures. The contact pad interspacing is 160 μm.

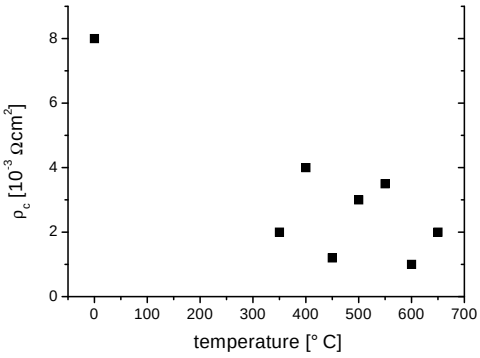

Fig. 5. Influence of temperature treatment on the specific contact resistance of Pd/Au contacts.

As depicted in Fig. 2 the IV-characteristics of Ni/Au contacts show ohmic behaviour for RTA treatment up to 400 °C , but are getting worse for higher anneal temperatures. This coincides well with determined specific contact resistances (Fig. 3), where the lowest value $\rho_c = 3.7 \cdot 10^{-2}\,\Omega\mathrm{cm}^2$ is achieved at 400 °C in this material system. With temperature up to 600 °C the specific contact resistance is getting worse, but is still in the range of the untreated contact. The mercurial increase for temperatures higher than 600 °C is due to balling up and agrees with results published by Trexler et al. [4].

Another promising contact system for p-type GaN due to its high metal work function of 5.2 eV is palladium (Pd) covered by gold [5]. Fig. 4 shows the IV-characteristics of Pd/Au contacts treated with different RTA-temperatures. The IV-characteristics as well as the specific contact resistances show no influence of the anneal temperature, as can be seen in Fig. 5. The determined $\rho_c = 1 - 4 \cdot 10^{-3}\,\Omega\mathrm{cm}^2$ for the Pd/Au contacts is one order of magnitude better than the results obtained for the Ni/Au system.

4. Conclusion

In this study, we presented the influence of wet chemical pre-treatment on contact resistances. With a dip in HCl solution before metal deposition, we were able to reduce the specific contact resistance of as-deposited Ni/Au contacts by a factor of 10 to $\rho_c = 0.15\,\Omega\mathrm{cm}^2$. After a 400 °C anneal step, this value could be improved to $\rho_c = 3.7 \cdot 10^{-2}\,\Omega\mathrm{cm}^2$. With similar treatment Pd/Au contacts on Mg-doped GaN with specific contact resistances as low as $1 \cdot 10^{-3}\,\Omega\mathrm{cm}^2$ have been fabricated.

References

[1] Y.-S. Park, “Current status of group III-nitride semiconductors and future prospects”, *J. Korean Phys. Soc.*, vol. 34, pp. S199–S219, 1999.

[2] G.K. Reeves and H.B. Harrison, “Obtaining the specific contact resistance from transmission line model measurements ”, *IEE Electron. Device Let.* , vol. EDL-3, pp. 111–113, 19828.

[3] Q.Z. Liu, and S.S. Lau, “A review of the metal-GaN contact technology”, *Solid State Electron.*, vol. 42, pp. 677–691, 1998.

[4] J.T. Trexler, S.J. Miller, P.H. Holloway, and M.A. Khan, “Interfacial reactions between metal thin films and p-GaN”, *Mat. Res. Soc. Symp. Proc.*, vol. 395, pp. 819–824, 1996.

[5] J.K. Kim, J.-L. Lee, J.W. Lee, H.E. Shin, Y.J. Park and T. Kim, “Low resistance Pd/Au ohmic contacts to p-type GaN using surface treatment”, *Appl. Phys. Lett.*, vol. 73, pp. 2953–2955, 1998.

Junction Temperature Determination of InGaN LED unter Operation

Veit Schwegler

Heat generated by ohmic losses is a critical parameter for performance and lifetime of light-emitting diodes (LEDs). The temperature of InGaN MQW LEDs during operation has been investigated depending on the forward current using three independent methods. First, the temperature of the active region was derived from the electroluminescence spectra of the devices. Second, temperature dependent micro-Raman scattering by phonons was used to determine the local temperature. Finally, a finite element simulation was performed to get a full temperature profile of the device. While the first method yields the temperature of the active region, the latter two can map the thermal distribution. All three independent methods reveal maximum operation temperatures about 120-130 $^\circ?C$ *at a current density of 300* $\mathrm{A/cm^2}$*, corresponding to a power density of 705* $W\,cm^{-2}$*.*

1. Introduction

Due to improved epitaxial growth the external quantum efficiencies of nitride based LEDs notably increased over the last couple of years. Best values of 12 % for blue and green emitting LEDs were presented by Nakamura et al [1]. However, they are still significantly below external quantum efficiencies known from GaAs based devices (25-30 %) [2]. Together with the high operation voltages, conditional on the wide bandgap, this leads to a severe ohmic heating under operation. The generated heat causes an exponential drop of the output power. Additionally, migration of dislocations as well as diffusion of impurities (e.g. dopands, contact metals), both crucial for device degradation, strongly depend on temperature [3][4].

2. Experimental Setup

The devices under investigation are InGaN multi quantum well LEDs grown on sapphire substrates. Narrow, single peak emission at about 410 nm is observed; the output power of the UV LEDs is in the 0.5 mW range. As buffer layer 2 μm undoped GaN and 1 μm Si-doped GaN are deposited. The active region contains a 4 x InGaN/GaN (1.5 nm/5.5 nm) quantum well structure, followed by 100 nm Mg-doped $\mathrm{Al_{0.08}Ga_{0.92}N}$ and a 300 nm thick p-doped GaN cladding layer. The free carrier concentrations are $p = 2 - 3 \cdot 10^{17}\ \mathrm{cm^{-3}}$ for the Mg-doped GaN and $n = 5 \cdot 10^{18}\ \mathrm{cm^{-3}}$ for the GaN:Si. Chemically assisted ion-beam etching (CAIBE) is used to form a circular mesa structure. A Ni/Au metallization (40 nm/250 nm) is evaporated for p- and

n-contacts to keep processing as simple as possible. The contact geometry of the LED consists of a circular inner contact with windows for micro-Raman measurements and a surrounding n-contact. The series resistance of the device is approximately 30 Ω. The described devices are sawn into pieces of approximately 800 x 1800 μm and are mounted on a teflon plate or a metal heat sink for measurements. Electroluminescence spectra are taken at forward currents of 2 - 40 mA. The temperature of the active region is derived from the short wavelength slope near the maximum of these electroluminescence spectra according to Ref. [5]. For the micro-Raman measurements the 514 nm line of an Ar^+ laser is used as excitation source. The temperature of the InGaN diode under operation is determined from the relative shift of the GaN E2-phonon frequency with respect to its frequency at zero current. The 520.3 cm^{-1} plasma line of the Ar+ laser is used as reference to achieve an exact determination of the E2-phonon frequency. A detailed description of this measurement method including a calibration curve of the GaN temperature versus the E2-frequency shift is given in Ref. [6].The laser beam was focused by a microscope lens system yielding a spot diameter of 0.7 μm, thus enabling a high spatial resolution.

3. Measurements and Results

The current dependent temperature of a LED mounted on a teflon heat sink reveals a significant heating to $160°C$ even at a moderate current of 30 mA, corresponding to a power density of 705 Wcm^{-2} (Fig. 1). Within the scatter Raman spectroscopy and the evaluation of the electroluminescence spectra are in excellent agreement. The influence of the thermal conductivity of the heat sink becomes obvious by replacing the teflon plate against a metal heat sink. Whereas a current of 15 mA leads to a temperature of approximately 100 $°C$ with a LED mounted to a teflon insulator, the same temperature is not reached until a current of 63 mA in the case of a LED mounted to a metal heat sink. Choosing the latter experimental setup, micro-Raman spectroscopy was used to resolve the thermal distribution within the LED and its surrounding (Fig. 2, squares).

The highest gradient is clearly present beneath the p-contact (diameter 160 μm), whereas beyond the n-contact (diameter 240 μm) thermal equilibrium is established very soon. The thermal distribution calculated by the finite element program ANSYS (solid line in Fig. 2) shows a similar spatial temperature behavior like the Raman measurements. For the simulation the geometry of the device as well as the thermal and electrical properties of the contained materials (including contacts) are considered. Within the simulation there is no fitting parameter. The only input parameter besides referenced material and device properties is the backside temperature used as boundary condition. This temperature has been measured to 40°C using a thermal probe. The obtained thermal distribution in the mesa area is shown in Fig. 3.

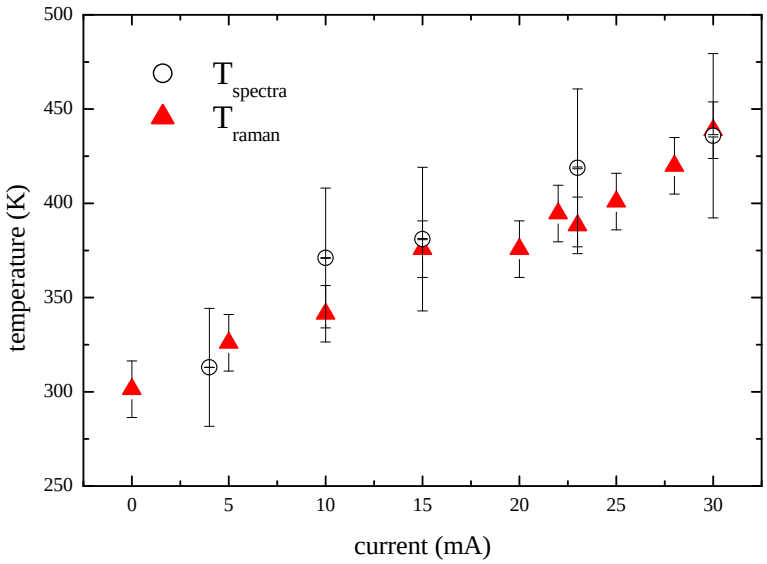

Fig. 1. Temperature of an InGaN-MQW LED under operation deduced from Raman shift of the E2 phonon and derived from the measured electroluminescence spectra.

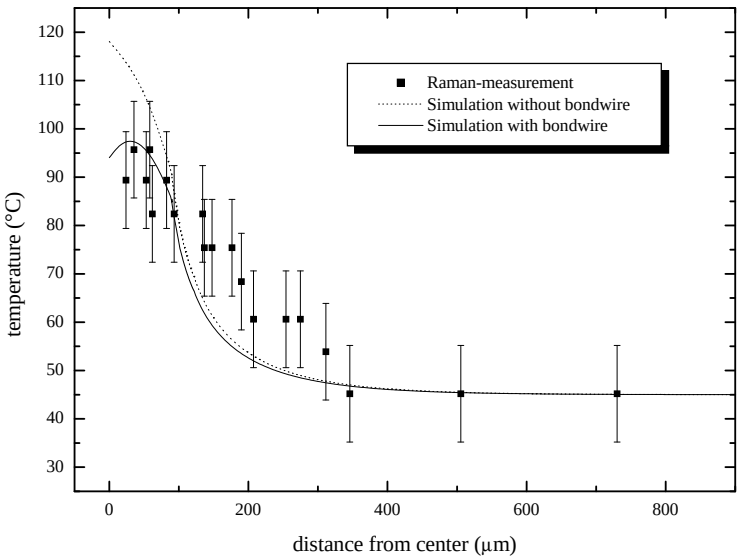

Fig. 2. Spatial temperature distribution within an InGaN-MQW LED obtained by micro-Raman measurements (squares). The solid line shows the temperature distribution calculated by finite element method.

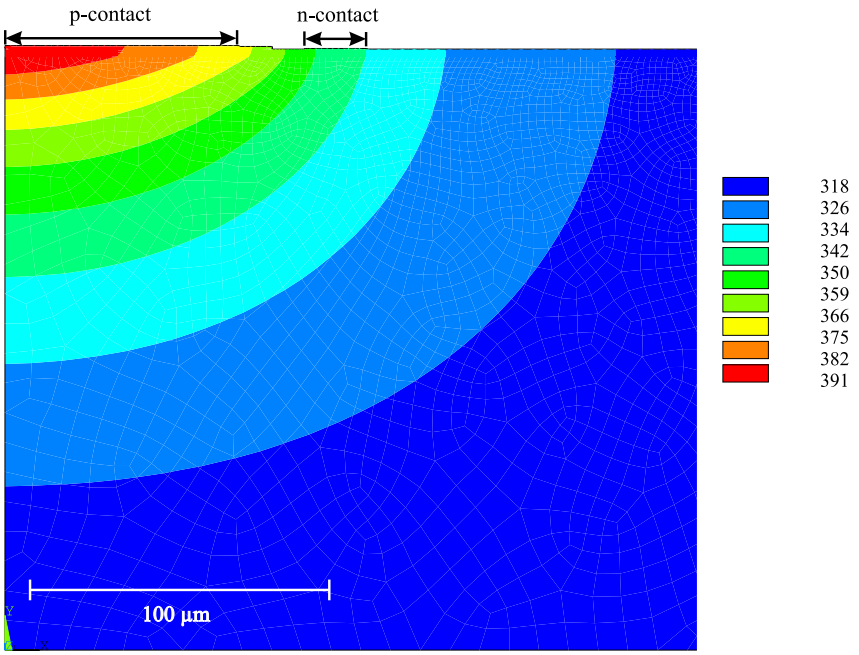

Fig. 3. Temperature distribution of an InGaN-MQW LED according to the finite element calculations.

4. Conclusion

The temperature of InGaN/GaN MQW LEDs under operation have been determined by three independent methods: electroluminescence, Raman measurements, and finite element simulation. Very good agreement is found between these methods. Temperature determination from electroluminescence and Raman scattering agree on the current dependent heating of the device. Spatially resolved μ-Raman and finite element simulations reveal further agreement on the heat distribution within the device. Temperatures as high as $140\,^{\circ}\mathrm{C}$ are found for even moderate currents of 30 mA. The region of elevated temperatures is mainly restricted to the active device area beneath the p-contact. Furthermore, the results show the strong influence of the heat sink employed.

References

[1] S. Nakamura, “InGaN-based violet laser diodes”, *Semicond. Sci. Technol.* **14**, vol. 27, pp. R27–R40, 1999.

[2] G. B. Stringfellow, M .G. Craford (Eds.), “High Brightness Light Emitting Diodes”, Academic Press, 1997.

[3] L. Sugiura, “Dislocation motion in GaN light-emitting devices and its effect on device lifetime ”, *J. Appl. Phys*, vol. 81, pp. 1633–1637, 1997.

[4] M. Osinski, J. Zeller, P.C. Chiu, B.S. Phillips, and D.L. Barton, "AlGaN/InGaN/GaN blue light emitting diode degradation under pulsed current stress ", *Appl. Phys. Lett.*, vol. 69, pp. 898–900, 1996.

[5] A.E. Yunovich, V.E. Kudryashov, A.N. Turkin, A.N. Kovalev, and F.I. Manyakhin, "Electroluminescence Properties of InGaN/AlGaN/GaN Light Emitting Diodes with Multiple Quantum Wells", *MRS Internet J. Nitride Semicond. Res.* **4S1**, G6.29, 1999.

[6] A. Link, K. Bitzer, W. Limmer, R. Sauer, C. Kirchner, V. Schwegler, M. Kamp, D.G. Ebling, and K.W. Benz, "Temperature dependence of the E_2 and $A_1(LO)$ phonons in GaN and AlN", *J. Appl. Phys*, vol. 86, pp. 6256–6260, 1999.

In-Situ Characterization During MOVPE Growth of III-Nitrides using Reflectrometry

Christoph Kirchner and Matthias Seyboth

The suitability of in-situ reflectrometry during low pressure Metal Organic Vapor Phase Epitaxy (MOVPE) growth of GaN was examined using a commercial fiber reflectometer. Reflectrometry was succesfully used for determining deposition rates in a horizontal MOVPE reactor during nitride growth. The initial growth stages such as deposition of low temperature nucleation layer and the initial nucleation of crystalline GaN can be observed in the obtained reflectance spectra as changes in reflectance.

1. Introduction

Nitride based materials comprise today's fastest developing III-V compound semiconductor (InAlGaN) technology. Excellent optical and electrical properties, a wide and direct bandgap in combination with high thermal, mechanical, and chemical robustness make GaN and its alloys a well suited material system for optoelectronic devices in the UV to visible range (e.g. light emitting diodes (LEDs), laser, photodetectors) [1], [2], [3].

Successfull epitaxial growth of such multilayered device structures requires precise control of the growth parameters (temperatures, flows, pressures) to achieve reproducible results. In particular, the heteroepitaxial GaN growth on highly mismatched substrates requires a two-step growth process consisting of low temperature nucleation layer and annealing step prior to the device growth to achieve high quality epitaxial GaN layers. Deposition and subsequent annealing of the nucleation layer is a critical, highly sensitive process. Reproducibility remains a problem due to the fact that small variations of substrate temperature and slightly different sapphire morphologies strongly influence properties of the nucleation layer and subsequent GaN growth. In-situ characterization methods would be very helpful to control the initial growth stages of GaN. Due to the lack of high vacuum conditions, RHEED (reflection high electron energy deflection) systems, as widely used in MBE to control two-dimensional growth, growth rates and composition of ternary layers, cannot be applied in MOVPE. However, in-situ reflectrometry can provide a similar access to the growth process during gas phase epitaxy. In this article we describe the use of in-situ reflectrometry during MOVPE GaN epitaxy to control the growth parameters.

2. Experimental

Epitaxial growth of GaN is conducted in a horizontal, radio-frequency heated, water cooled quartz MOVPE reactor (AIXTRON AIX 200 RF) operated at low pressure. Trimethylgallium (TMGa), Trimethylindium (TMIn), Trimethylaluminum (TMAl) and ammonia are used as group III and group V precursors, respectively. The mostly used substrate material is sapphire (Al_2O_3). The MOVPE system was equipped with a commercially available reflectometer system consisting of a white light source and a CCD spectrometer (Filmetrics F 30). The spectrometer is a 512-element photodiode array with a spectral range of 400 nm - 1100 nm and a resolution of 2 nm. The spectrometer is controlled by a computer and the spectrometer software allows calculation of deposition rates, the refractive index n, the extinction coefficient k and reflectivity from the measured data. For this purpose, material data libraries are contained in the software. Reflectance spectra can be displayed versus time or wavelength. The setup allows simultaneous measurements of reflectivity at three different wavelengths. Fig. 1 shows the complete setup. To enable optical measurements on the sample surface, an optical access to the substrate with the growing nitride layer in the MOVPE reactor is mandatory. The reaction chamber of the employed MOVPE system is a liner tube made of quartz glass. Due to the horizontal configuration of the reactor, the ceiling of the liner gets coated with Nitride deposits during growth, making it intransparent for visible light. Therefore, a hole with a diameter of 5 mm was drilled in the liner ceiling. The liner is located inside a quartz cylinder (outer reactor tube), which is surrounded by the water cooling jacket made of quartz, too. Both the incident and reflected light has to pass all the quartz walls and the cooling water. Disturbing reflections from the quartz walls can be eliminated by reference measurements. The spectrometer and the light source are connected to the measuring head (lens system) by optical fibers. With the lens system, the light is focused on the sample and the reflected light is coupled into the spectrometer. The lens system is designed for normal incidence, the fiber is of coaxial type as depicted in Fig. 1 (upper left insert). The reflectance of the sample surface, recorded during the growth process, is continuously monitored. Substrate material for all in-situ controlled growth processes is c-plane ([0001]) oriented sapphire. After loading into the reactor, substrates are heated up to 950 °C under a steady flow of a nitrogen / hydrogen mixture. Following this sapphire surface cleaning step, the substrate temperature is lowered to 520 °C for the deposition of the low temperature nucleation layer. After the nucleation layer is deposited, reactor temperature is increased to 1050 °C for growth of undoped bulk GaN. The effects of these growth steps on the sample surface reflectance are described in the following section.

3. Results and Discussion

Reflectance spectra obtained with the above mentioned setup from MOVPE GaN growth processes on sapphire are shown in Fig. 2. The two curves were recorded during GaN growth on sapphire substrates with slightly different polishing delivered from different manufacturers. The deposition of the nucleation layer causes the first increase in reflectivity. During the following annealing step, while the polycrystalline nucleation layer is partially crystallizing, the reflection increases slightly and then drops. At this point the main GaN layer growth is started,

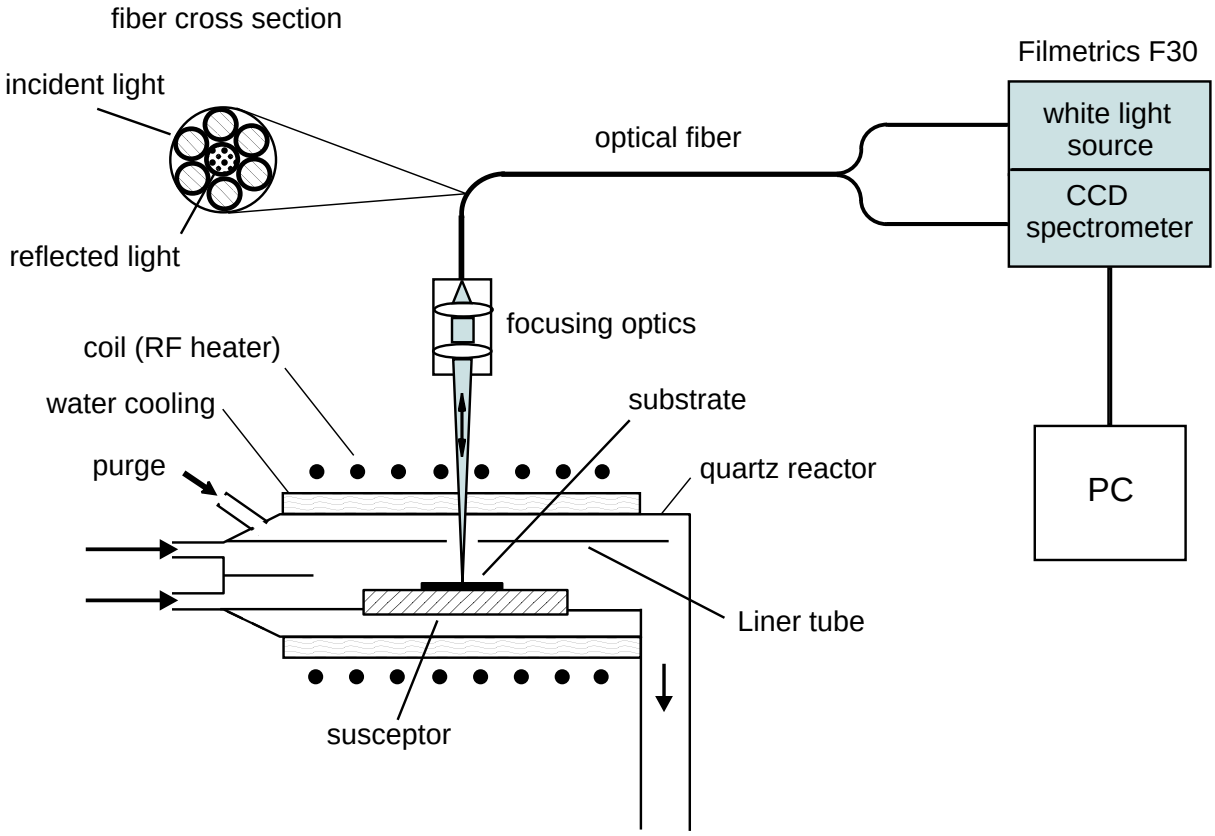

Fig. 1. In-situ reflectance setup at the AIX 200 RF horizontal MOVPE reactor

revealing small oscillations with increasing amplitude due to decreasing surface roughness. In spite of the fact, that all growth parameters were kept constant, in the initial stages of GaN growth, the course of oscillations amplitudes in the two curves is totally different. While in the upper curve, the maximum amplitude is reached after two oscillations, the lower curve reaches maximum after four oscillations. This confirms, that heteroepitaxial GaN growth processes are very sensitive against every small variation of sapphire substrate properties. Development of the surface morphology is indicated by the course of amplitudes in the reflectance spectrum. After a few oscillation periods, the growth conditions are stabilized. The shown oscillations of the GaN growth correspond to a growth rate of 2 μm/hr. The thickness of the GaN which is grown during one oscillation can be approximately calculated using the following equation [4]:

$$d_{GaN}[nm] = \frac{\lambda_m}{2n} \tag{1}$$

where λ_m is the measuring wavelength of the spectrometer in nm and n is the refractive index of GaN at the measuring wavelength. The oscillations are resonances of the layer system, where the resonator is formed by the GaN layer and the refractive index steps of the transitions GaN/sapphire and GaN/gas phase, respectively. In Fig. 2, one oscillation corresponds to a GaN layer thickness of around 118 nm, according to Eq. (1). The refractive index of GaN at

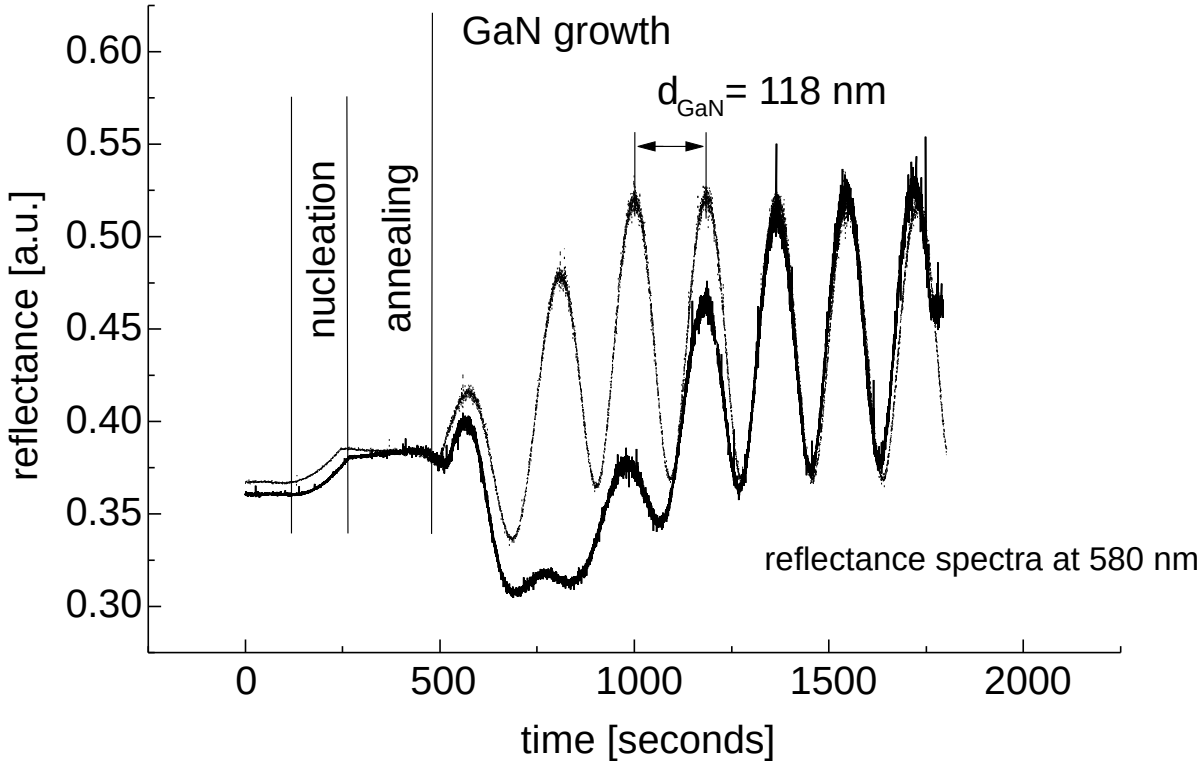

Fig. 2. In-situ reflectance spectra obtained during MOVPE growth of GaN. The two curves represent sapphire substrates from different suppliers, revealing strong differences in the initial stages of growth.

the spectrometer wavelength of 580 nm is 2.45 [5] and does not change much with temperature [4]. Thus the values for thickness calculated during growth (hot substrate) agree well with data measured at room temperature using SEM. During ternary layer growth (InGaN, AlGaN), prereactions in the reactor between the different group III molecules and ammonia can occur, strongly affecting growth rates and composition . The intensity of the prereactions is dependent of pressure and temperature in the reactor during growth and the type and amount of group III molecules (e. g. TMGa, TEGa, TMAl). In-situ reflectrometry provides direct information on any change of growth parameters (pressure, temperature, fluxes) affecting either growth rate (change of oscillation width) and/or surface roughness (change of oscillation amplitude).

4. Conclusion

In-situ reflectrometry was succesfully applied to an existing MOVPE system. The reflectance changes of the GaN surface provide important information about Nitride growth. Growth rates can be controlled in-situ, allowing adjustment of group III flows to achieve the desired growth rate. The initial growth stages of GaN growth, being very important for good material quality, have been monitored succesfully.

References

[1] S. Nakamura, M. Senoh, N. Iwasa and S. Nagahama, “High - brightness InGaN blue, green and yellow light emitting diodes with quantum well structures”, *Jpn. J. Appl. Phys.*, vol. 34, pp. L 797–L 799, 1995.

[2] S. Nakamura, M. Senoh, S. Nagahama, N. Iwasa, T. Yamada, T. Matsushita, H. Kiyoku, Y. Sugimoto, T. Kozaki, H. Umemoto, M. Sano and K. Chocho, “InGaN/GaN/AlGaN-based laser diodes with modulation-doped strained-layer superlattices grown on an epitaxially laterally overgrown GaN substrate”, *Appl. Phys. Lett.*, vol. 72, pp. 211–213, 1997.

[3] S. Nakamura, M. Senoh, S. Nagahama, N. Iwasa, T. Yamada, T. Matsushita, H. Kiyoku, Y. Sugimoto, T. Kozaki, H. Umemoto, M. Sano and K. Chocho, “Continous-wave operation of InGaN/GaN/AlGaN-based laser diodes grown on GaN substrates”, *Appl. Phys. Lett.*, vol. 72, pp. 2014–2016, 1998.

[4] S. Nakamura and G. Fasol, “The Blue Laser Diode - GaN Based Light Emitters and Lasers”, *Springer*, Berlin Heidelberg, 1997.

[5] J. H. Edgar, S. Strite, I. Akasaki, H. Amano and C. Wetzel (Eds.), “Properties, Processing and Applications of Gallium Nitride and Related Semiconductors”, EMIS Datareview Series No. 23, *INSPEC*, The Institution of Electrical Engineers, London, UK, 1999.

Parasitic Reactions in MOVPE Growth of AlGaN: Experiment and Modelling

Matthias Seyboth and Christoph Kirchner

Experiments on the growth pressure dependence of the aluminum content in MOVPE grown AlGaN have been performed. Under the assumption of strong premature reactions between ammonia and TMAl we were able to derive a powerful yet simple model for growth of AlGaN. Beside an improved predictability this model allows a better understanding of growth processes.

1. Introduction

$\mathrm{Al_xGa_{1-x}N}$ is a critical component in several GaN based devices. It is used as electron barrier in light emitting diodes (LEDs) and lasers ($x \approx 15\,\%$) [1], serves as waveguide structure in lasers ($x \approx 8\,\%$) [1] and is employed as material for FETs (x up to $100\,\%$). Therefore a wide range of Al-content has to be realized by epitaxial growth.

A major problem for metalorganic vapor phase epitaxy (MOVPE) growth of AlGaN are parasitic reactions in the gas phase. It is well known that these premature reactions can be reduced with lower growth pressures [2]. In our study we show the relation of pressure and Al-content and derive a model for quantitative prediction for our particular reactor system.

2. Experimental

For our growth experiments we used an Aixtron AIX 200 RF horizontal MOVPE reactor. On c-plane sapphire we grew structures with 2μm GaN buffer and AlGaN layer (100 – 300 nm) at 1030 °C. AlGaN layers were grown with different reactor pressures (ranging between 25 and 220 mbar) and molecular TMAl to TMGa ratios (0.28 to 4).

The Al-content was derived mostly from X-ray diffraction measurements ((0002)-reflex in $\omega - 2\Theta$-scan). Samples with a microscopically visible (magnification $\geq$100) cross hatch pattern are regarded as relaxed material. In some cases the Al-content was determined from in situ reflectance measurements. The Al-content was judged from the increase of growth rate when TMAl was added to the gas phase. Figure 1 shows the rocking curves for AlGaN layers grown at 50 and 100 mbar with aluminum contents of 56 % and 32 %, respectively. The two curves which are not normalized show well separated peaks with FWHM of about 300 arcsec both for AlGaN and GaN.

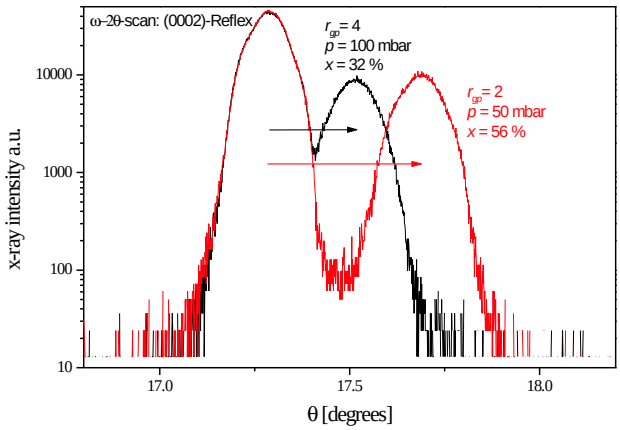

Fig. 1. Rocking curves of AlGaN grown at different pressures p and gas phase compositions r_{gp}

3. Results and Discussion

For performing epitaxial growth the relation between the composition in the supplied gas phase and the resulting solid state composition is decisive. So we compare the ratio of TMAl to TMGa molecules injected into the gas phase (r_{gp}) with the ratio of Al to Ga in the solid state $Al_xGa_{1-x}N$ ($r_{ss} = x/(1-x)$). Assuming no prereactions in the gas phase the ratio of solid state composition to gas phase composition r_{ss}/r_{gp} is given by the ratio of incorporation efficiencies of Al (i_{Al}) to Ga (i_{Ga}):

$$\frac{r_{ss}}{r_{gp}} = \frac{i_{Al}}{i_{Ga}} \tag{1}$$

In Fig. 2. r_{ss}/r_{gp} is plotted versus the growth pressure (p) for different r_{gp} injection ratios.

We find a strong decrease of r_{ss}/r_{gp} with increased pressure, which means with higher pressure the aluminum content of the structure is reduced. This behavior is observable for the different gas phase compositions in the same way.

We can explain this behavior with the asumption of a homogeneous gas phase reaction between ammonia and TMAl (cf. [1]). There are no indications for such a reaction with TMGa. After mixing hydrids and metal organics the TMAl concentration in the gas phase is reduced on the way to the sample, so there is a reduced ratio r'_{gp} in the growth region. With the excess of NH_3 compared to TMAl we presume a first order reaction, leading to a time dependence according to

$$r'_{gp} = r_{gp}e^{-\alpha t} \tag{2}$$

where the reaction constant α, depending on pressure, temperature, V/III ratio, etc., describes the amount of effective collisions between TMAl and NH_3. From the ideal gas we take $\alpha \propto p^2$ as the number of reactions per times is proportional to the number of collisions per time given

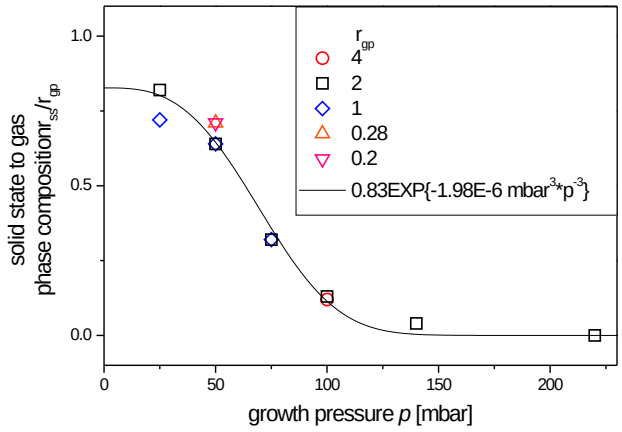

Fig. 2. Pressure dependence of solid state to gas phase composition ratio r_{ss}/r_{gp}

by the volume collision rate proportional to p^2 [3]. The time for a volume in our gas phase from reactor inlet to substrate is proportional to the growth pressure ($t \propto p$). This results in:

$$r'_{gp} = r_{gp} e^{-\alpha' p^3} \tag{3}$$

As the solid state composition is determined by the gas phase composition at the growth zone r'_{gp} and the incorporation efficiencies, this yields

$$r_{ss} = \frac{i_{Al}}{i_{Ga}} r'_{gp} = \frac{i_{Al}}{i_{Ga}} r_{gp} e^{-\alpha' p^3}. \tag{4}$$

In Fig. 1. we displayed

$$\frac{r_{ss}}{r_{gp}} = \frac{i_{Al}}{i_{Ga}} e^{-\alpha' p^3}. \tag{5}$$

At p =0 mbar (no prereactions) we should find for different r_{gp} always the same value i_{Al}/i_{Ga}, which complies with the experimental data. Describing the data in Fig. 1. with Eq. (5), we obtain i_{Al}/i_{Ga}=0.83, a lower incorporation of Al in respect to Ga. For α' we get 1.98·10^{-6},mbar^{-3}, a value difficult to estimate because of the variety of parameters described with this one constant (effective reaction cross section, reactor constants, distance from mixture to substrate, etc.). The overall agreement of the experimental data to the deduced formula is quite good.

For epitaxial growth the aluminum content x is the value we want to control. So in Fig. 3. aluminum content versus growth pressure for varied r_{gp} settings is depicted together with the functions:

$$x = \frac{r_{ss}}{1 + r_{ss}} = \frac{1}{1 + \frac{i_{Ga}}{i_{Al} r_{gp}} e^{\alpha' p^3}} \tag{6}$$

For evaluation of Eq. 6 the obtained fitting parameters for i_{Al}/i_{Ga} and α' were used. Fig. 3. replicates the accordance of experimental data to our model and allows an easy way to adjust aluminum content in structures with settings of r_{gp} and p.

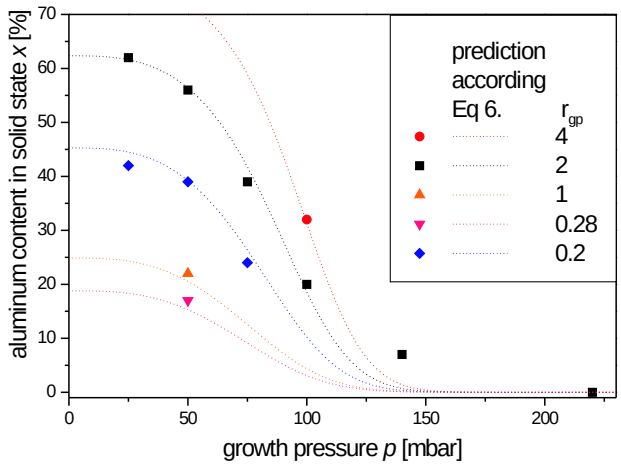

Fig. 3. Pressure dependence of Al content x for different gas phase compositions r_{gp}

4. Conclusion

Based upon the reasonable assumption of homogenous parasitic reactions between ammonia and TMAl we were able to develop a model for the growth of AlGaN. It enables quantitative predictions in a wide pressure and gas phase composition range. Beyond this we saw a different incorporation efficiency for Al and Ga (i_{Ga}/i_{Al}=0.83).

References

[1] S. Nakamura, G. Fasol, “The blue Laser Diode”, Springer, 1997.

[2] B. Gil, “Group III Nitride Semiconductor Compounds”, Oxford Science Publications, 1998.

[3] C.H. Chen, H. Liu, D. Steigerwald, W. Imler, C.P. Kuo, M.G. Craford, M. Ludowise, S. Lester, and J. Amano, “A Study of Parasitic Reactions Between NH_3 and TMGa or TMAl”, *Journal of Electronic Materials*, Vol. 25, No 6, pp. 1004–1008, 1996.

[4] M. Wutz, H. Adam, and W. Walcher, “Handbuch Vakuumtechnik”, Vieweg, 1997.

Optimized Epitaxial Structure of Laser Diodes for High-Power and High-Brightness Applications

Eckard Deichsel and Frank Demaria

A design strategy for the optimization of high-power broad-area epitaxial material is presented, which gives a good compromise between high efficiency and beam quality. The optical confinement has been reduced leading to broader vertical near fields, narrower far fields, reduced filamentation, and an increase in the COMD level. The disadvantages, e.g. the increase of the intrinsic absorption can be compensated by an accurate control of epitaxial doping profile. The characteristics of lasers fabricated from optimized material prove this statement.

1. Introduction

The demand for high-power laser diodes permanently increases, since they offer lots of applications, like material processing, pumping of solid-state lasers and erbium-doped fiber amplifiers, and the use in medical systems. All high-power applications require high power densities. Usually the optical power of broad-area lasers is very high but the beam profile is poor. To focus a high-power laser to a small spot, e.g. for optical fiber coupling, the quality of the beam needs to be improved. The transverse modes in edge-emitting devices can be assumed to be single mode with Gaussian shape. In the lateral direction however, the near field of high-power broad-area laser usually tends to be multi mode leading to a poor horizontal far field. There are different ways to influence the lateral beam propagation in a laser in order to get improved beam qualities, e.g. unstable cavities or MOPAs. But the basic for all high-brightness laser devices is the epitaxial layer structure which should be optimized to meet the requirements for high-power applications.

2. Epitaxy

The investigated epitaxial structures consist of a single-quantum-well graded-index separate-confinement heterostructure (SQW-GRINSCH). The regions of interest are the quantum well, the bounding layers, the shape and slope of the gradings, the doping, and the cladding layers. Starting from a working epitaxial structure, layer thicknesses and compositions have been varied systematically in order to understand the influence on the characteristics of the laser device. For some parameters, a compromise has to be found. For example, an improvement of the electrical behavior of the device by increasing the doping level will increase the intrinsic absorption. An increase in the quantum efficiency by decreasing the reflectivity of the coatings

results in an increase in the threshold current which is an unwanted result. An optimization on high efficiencies [1], for example, means short devices, reduced intrinsic absorption by reducing the near field, and high dopings. But for high-power devices this is an improper solution, as shown in the next section.

3. Improvements

A limiting factor for the high-power lasers is the catastrophic optical mirror damage (COMD). These failures are caused by the high optical intensities at the laser facet. Suitable coatings can raise the COMD level. Another approach to increase this level is to reduce the maximum intensity at the laser facet by broadening the transverse near field. This can be done by a reduced confinement, which is shown in Fig. 1, where two transverse near fields are scaled to the same integral intensities showing different maximum intensities at the laser facet. The reduction of the confinement decreases the maximum facet intensity by 20 % and therefore raises the COMD level.

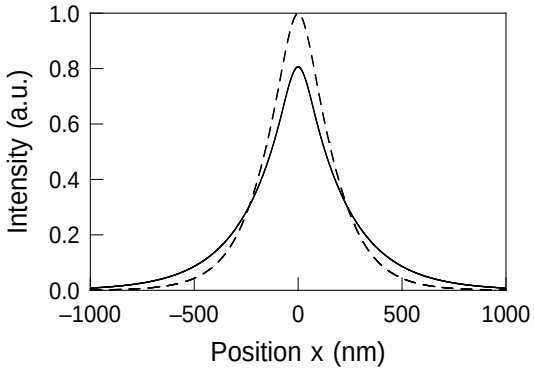

Fig. 1. Two simulated transverse near fields scaled to the same integral intensities. A reduced confinement leads to a broader near field (solid line) while the other structure (dashed line) gives a very narrow near field with higher peak intensity.

Because of the Fourier correlation of near and far fields, a reduced confinement leads to a decreased vertical far-field angle. Fig. 2 shows two measured vertical far fields with full-width-at-half-maximum angles reduced from 40 ° to 30 °. In some cases, this provides advantages when using optics with limited numerical apertures.

A very important advantage of the reduced confinement is the decrease of the confinement factor and the influences on the linewidth enhancement factor as described in [2]. The consequence is a reduction of filamentations. Fig. 3 compares two measured lateral near fields of power amplifiers. The near field of a device with $\Theta_{\mathrm{FWHM}} = 30\,^{\circ}$ and 1035 mW output power shows much less filamentations than the $40\,^{\circ}$ device with only 878 mW. Additionally reduced filamentations raise the COMD level and lead to better beam profiles. This is a prerequisite for high brightness devices.

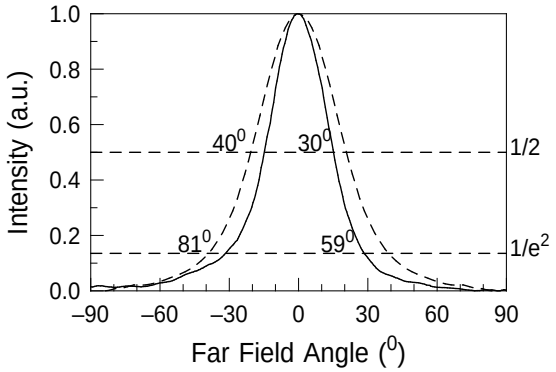

Fig. 2. Two measured vertical far fields. The reduced confinement leads to a decreased vertical far field angle. The full-width-at-half-maximum angle is reduced from 40 ° (dashed line) to 30 ° (solid line).

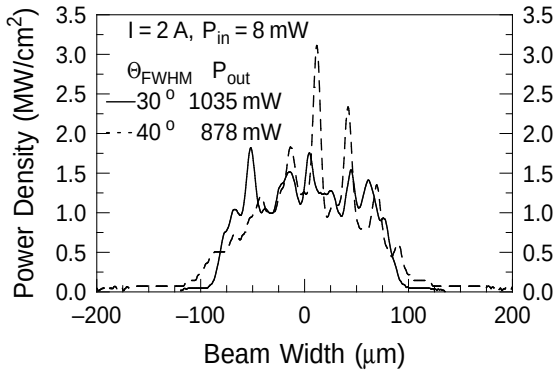

Fig. 3. Lateral near fields of the output facets of a power amplifier at 2 A driving current and 8 mW optical input power. The reduced confinement factor leads to decreased filamentations. The near field of a device with $\Theta_{\mathrm{FWHM}} = 30\,^\circ$ and 1035 mW output power (solid line) shows less filamentations than the 40 ° device (dashed line) with only 878 mW.

Of course, the reduced confinement provides disadvantages. The broader near field causes higher optical absorption which decreases the efficiency of the device. So a reasonable compromise is necessary, but with an accurately controlled epitaxial structure and doping profile the disadvantages can be kept reasonable.

4. High-power broad-area laser

Lasers have been fabricated from high-brightness optimized epitaxial material. The AR/HR-coated $900 \times 200\,\mu\mathrm{m}^2$ devices have been mounted junction-side down on a diamond heat-spreader and measured with a calibrated integrating sphere. The characteristics of one device is shown in Fig. 4.

Despite of the increased absorption, a differential slope efficiency of 70 % has been obtained

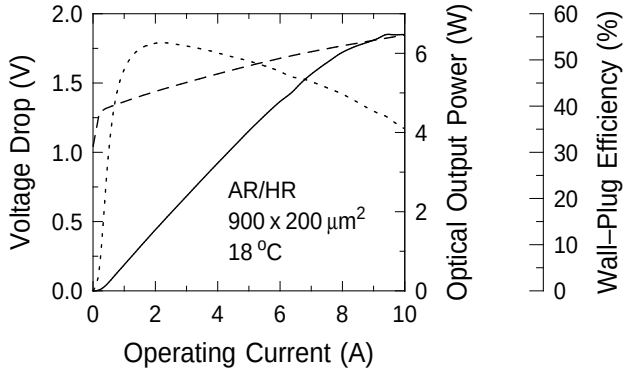

Fig. 4. Output characteristics of an AR/HR-coated $900 \times 200\,\mu\text{m}^2$ laser diode mounted junction-side down and measured with a calibrated integrating sphere. Plotted are the *L-I* (solid line) and the *V-I* (dashed line) characteristics together with the wall-plug efficiency (dotted line).

in the *L-I* curve. The threshold current density is as low as $140\,\text{Acm}^{-2}$ and the maximum optical power of 6.5 W is limited by thermal roll over. The device shows no facet damage even after several measurements. Other devices show the same characteristics which proves the reproducibility. This epitaxial material seems to be very promising for high-power and high-brightness applications.

5. Conclusion

The optimization of the epitaxial layer structure for high-power high-brightness applications has been discussed. A reduced optical confinement leads to broadened near fields with 20 % reduction in maximum facet intensity. The far-field angle is decreased down to 30 ° and filamentations are reduced, leading to a raised COMD level and improved beam quality. Characteristics of laser devices fabricated from high-brightness optimized epitaxial material are presented, showing good efficiencies despite of the increased absorption. The maximum output power of 6.5 W is not limited by facet damages.

References

[1] J. Heerlein, E. Schiehlen, R. Jäger, and P. Unger, "63 % wall-plug efficiency InGaAs/AlGaAs broad area laser diodes and arrays", in *Proc. CLEO/Europe 98, CThG2*, p. 267, Glasgow, UK, Sept. 1998.

[2] M. Osinski and J. Buus, "Linewidth broadening factor in semiconductor lasers - An overview", *IEEE J. Quantum Electron.*, vol. 23, pp. 9-29, Jan. 1987.

Fabrication and Characterization of Broad-Area Lasers with Dry-Etched Mirrors

Franz Eberhard and Eckard Deichsel

Using reactive ion-beam etching (RIBE) we have fabricated InGaAs/AlGaAs broad-area lasers with flat dry-etched mirrors. Optical output powers up to 1.5 W per facet at room temperature under continuous-wave operation have been measured. The results are comparable to lasers with cleaved facets made of the same epitaxial material. Monolithically-integrated monitor diodes show a linear responsivity to the optical output power of the laser. This advanced technology is a basic concept for future applications.

1. Introduction

Lasers with dry-etched facets have many advantages compared to conventionally-fabricated lasers. Optoelectronic integration becomes possible like the integration of a monitor photodiode for controlling the optical output power of the laser during operation. Another advantage is the ability of full-wafer processing and testing, that allows fabrication and characterization of lasers without separating the chips, leading to VLSI-type automation [1]. Therefore, the manipulation of the cleaved laser bars and chips, for example for the mirror-coating process, can be reduced to a minimum. Finally, the orientation and shape of the mirrors is no longer dependent on the crystal orientation. This enables new laser designs including unstable resonators [2], [3] and curved mirrors [4]. On the other hand, there are strict requirements for the dry-etched facets. Vertical, flat, smooth, and damage-free laser mirrors are necessary for good device performance. Tilted facets or corrugation of mirror surfaces lead to increased threshold currents, reduced efficiencies, and far-field distortions. Only an optimized etching process can fulfill these requirements.

2. Fabrication

The layer sequence of the lasers is a MBE-grown graded-index separate-confinement heterostructure (GRINSCH). The active region consists of two 8-nm-thick strained $In_{0.2}Ga_{0.8}As$ quantum wells resulting in an emission wavelenght of 980 nm. The p- and n-dopants are C and Si, respectively. In Fig. 1, the fabrication steps are schematically shown.

The lateral structure of the gain-guided broad-area lasers is defined by wet-chemical etching of the highly p-doped surface layer. These structures are covered with a Si_3N_4-passivation layer deposited by ion-beam sputter deposition. The contact areas are opened using a subsequent

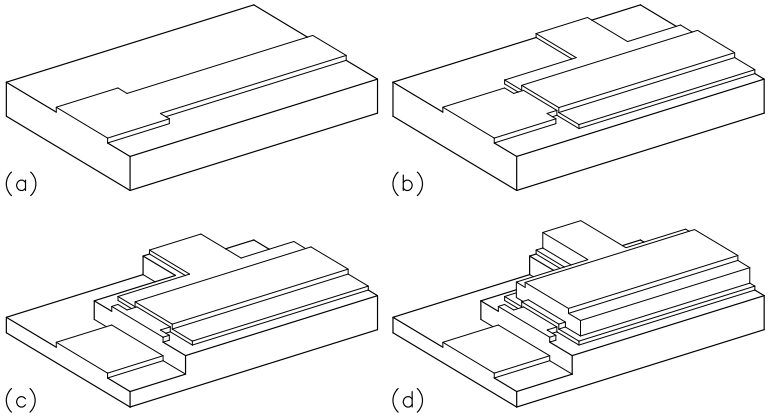

Fig. 1. Fabrication process of lasers with dry-etched mirrors: (a) wet chemical etching of the ridge and deposition of the Si_3N_4 passivation, (b) evaporation of the p-contact metalization, (c) dry etching of the mirror using RIBE, and (d) deposition of galvanic heat spreader.

lift-off process. The p contact is formed by Ti/Pt/Au metalization. These first steps are similar to the fabrication of cleaved lasers.

For the fabrication of vertical and smooth dry-etched mirrors, there are strict requirements regarding the etch mask. Characteristics of a good etch mask are high mechanical and chemical resistance, vertical profile in order to avoid facet roughening by edge erosion, and smooth facets [5], [6]. A trilevel-resist system has been utilized as etch mask. A hard-baked photoresist is used as bottom polymer, covered with a 50-nm-thick Ge intermediate layer. The imaging layer is formed by a positive photoresist, which is structured by contact printing. The pattern transfer into the intermediate layer and the bottom polymer is done by CHF_3/O_2 plasma etching (PE) and O_2 reactive ion etching (RIE), respectively. During the oxygen RIE, the top resist is also removed. The sidewalls of the 2.4-μm-thick remaining hard-baked bottom polymer are nearly vertical. In contrast to a standard photoresist, this trilevel resist can withstand high temperatures and high ion energies without undergoing severe degradation [7]. After etching, the mask can be removed in an organic solvent.

For the fabrication of the laser-diode facets, an etching system equipped with an electron-cyclotron-resonance (ECR) ion-beam source and load lock is used. The sample stage is temperature controlled in the range of -25 °C to 125 °C. In addition, the stage can be rotated and tilted. The base pressure of the turbo-molecular-pumped stainless-steel chamber is below $5 \cdot 10^{-8}$ mbar. A residual gas analysis shows that the main peak is caused by water vapor. For unselective etching of AlGaAs over GaAs such a low moisture content is highly desirable [6]. The etching system can be operated in reactive ion-beam etching (RIBE) mode by introducing chlorine into the ion source or in chemically-assisted ion-beam etching (CAIBE) mode by using argon as feed gas for the ion source and injecting chlorine through a gas ring located above the sample stage. In the etching tool we use, there is only small difference in the etching results between these two modes.

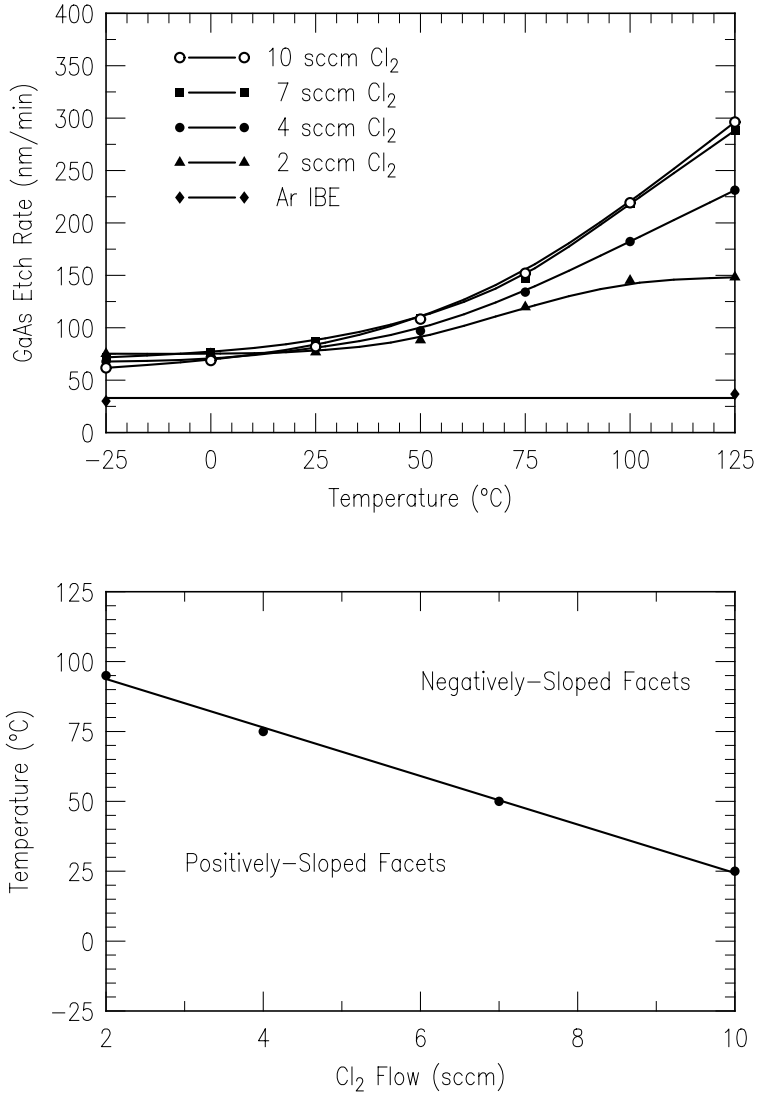

Fig. 2. Etch rate dependence of GaAs versus temperature for different chlorine gas flows (top). The viewgraph at the bottom shows combinations of chlorine flows and substrate temperatures to achieve vertical facets.

The upper viewgraph of Fig. 2 shows the etch-rate dependence of GaAs on temperature for different chlorine gas flows. Chlorine is used as feed gas for the ion source (RIBE), the ion energy is 400 eV. By increasing the substrate temperature from -25 °C to 125 °C the etch rate increases from about 75 nm/min up to 300 nm/min at high chlorine flows. At low substrate temperatures, the etch rate is limited by reaction or desorption of the etch products whereas at high temperatures the supply with etchant seems to limit the rate, as can be seen for chlorine flows of 2 sccm. At high chlorine flows, an increased number of collisions of ions with chlorine molecules in the reaction chamber causes energy losses [5], which compensate the increase in the chemical component.

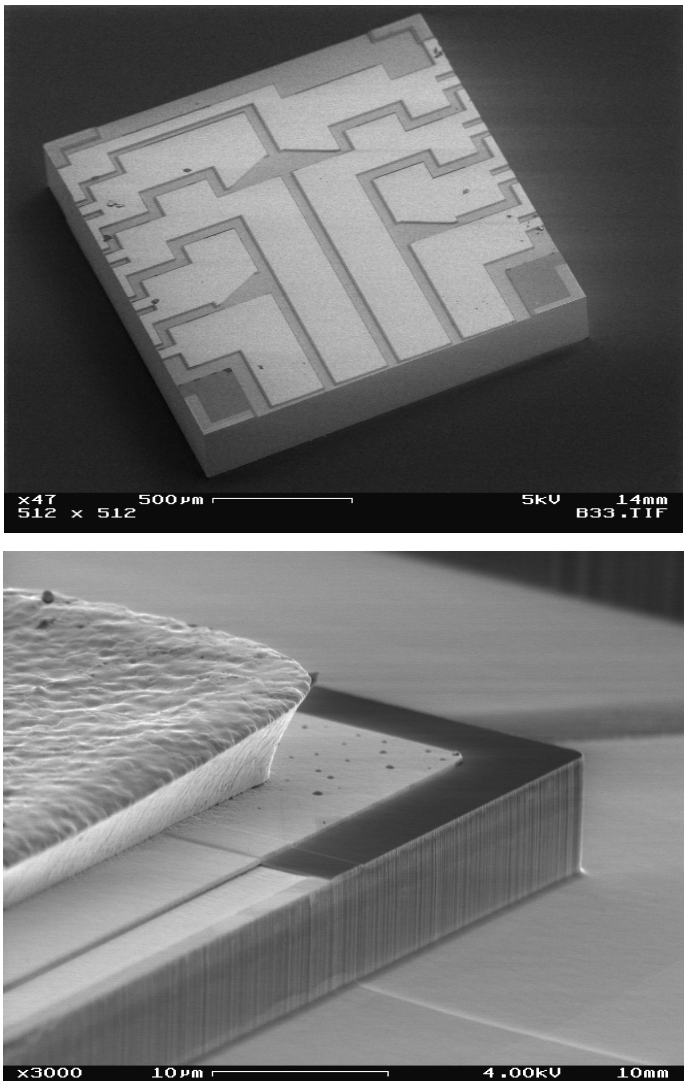

Fig. 3. The SEM micrograph at the top shows an integrated optoelectronic laser chip with dry-etched facets. The chip consists of 4 monitor photodiodes and 2 pairs of lasers with cavity lenghts of 500 μm and 1000 μm. The micrograph at the bottom provides a detailed view of the dry-etched laser facet. On the top of the structure the electroplated gold heat spreader is clearly visible.

The etch rate of ion-beam etching (IBE) using argon ions reaches only approximately 30 nm/min. Equirate etching of AlGaAs and GaAs is achieved even for an aluminum content of 90 % indicating that water vapor is not a problem in our etching system. The slope of the etched facets can be influenced by changing the ratio of physical to chemical etch component. Ion energy and current density determine mainly the physical etch component, the chemical part is given by substrate temperature and reactive gas flow. The lower part of Fig. 2 shows combinations of chlorine flows and substrate temperatures that yield vertical profiles.

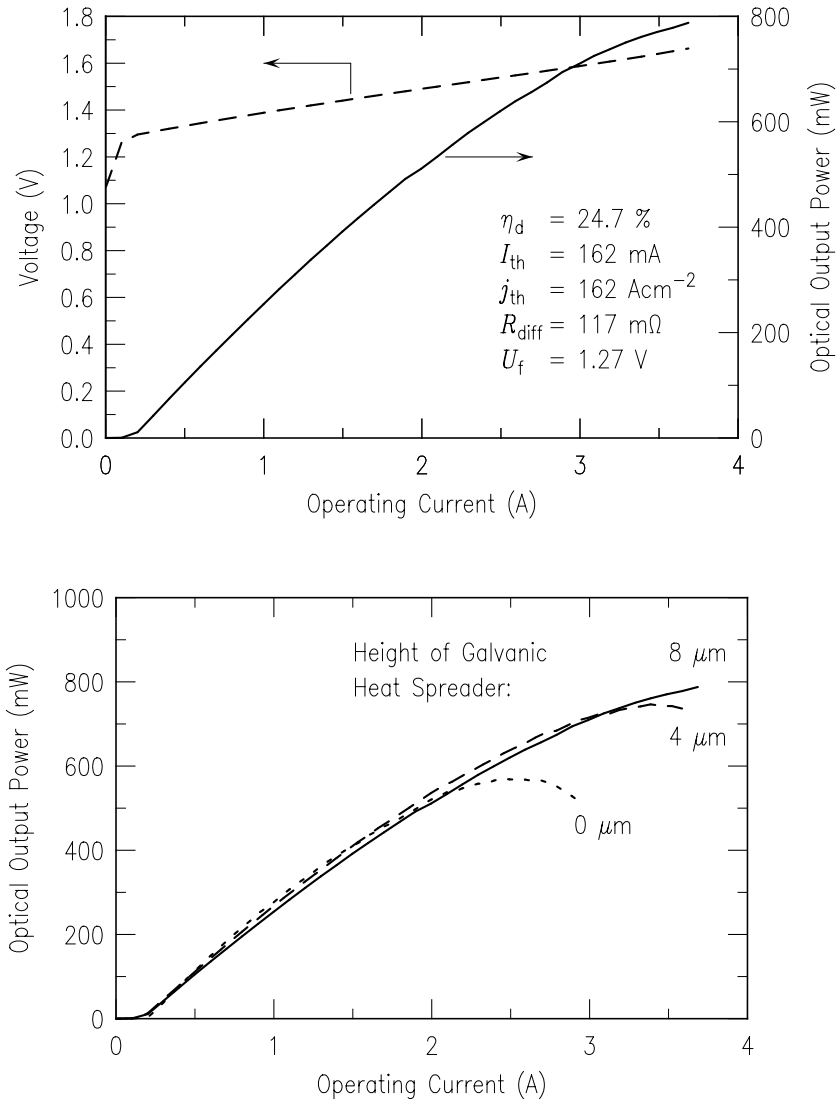

Fig. 4. At the top, the CW output power per facet (solid line) and the I-V characteristic (dashed line) of a 1000 μm · 100 μm broad-area laser with dry-etched facets are plotted. At the bottom, the influence of the heat spreader thickness on output power is shown for the same laser.

To etch the mirrors and to perform electrical and optical isolation of the devices, 7-μm-deep grooves are formed by reactive ion-beam etching. Vertical, flat, and smooth facets are achieved using a substrate temperature of 75 °C, an ion energy of 400 eV, and a chlorine flow of 4 sccm as can be seen in the SEM micrograph at the bottom of Fig. 3. This deep grooves are necessary to avoid back reflections of the laser beam at the bottom surface in front of the mirrors.

After dry etching the laser facets, a thick gold layer is electroplated on the p contact to reduce thermal and electrical resistance of the devices. For easier cleaving and improved heat removal, the wafer is thinned to a thickness of approximately 120 μm. The n contact is formed by evaporating and alloying a Ge/Au/Ni/Au metalization. The last step is cleaving the sample into single chips.

The SEM micrograph at the top of Fig. 3 shows such a chip with 4 broad-area lasers and the integrated photodiodes. The light-emitting facets are orientated to the front of the chip. The two central lasers have an area of 1000 μm $\cdot$ 100 μm, the length of the two outer lasers is 500 μm. To avoid reflection back into the lasers, the facets of the photodiodes are slanted. On the right and left sides of the chip, bond pads with an area of 200 μm $\cdot$ 200 μm are located. Since the p contact is used as plating base for the galvanic deposition of the heat spreading layer, the contact layout provides electrical connections between all devices on the wafer during fabrication. These interconnects can be seen at the left and right hand side of laser chip. Isolation is performed when the wafer is cleaved into single chips [8].

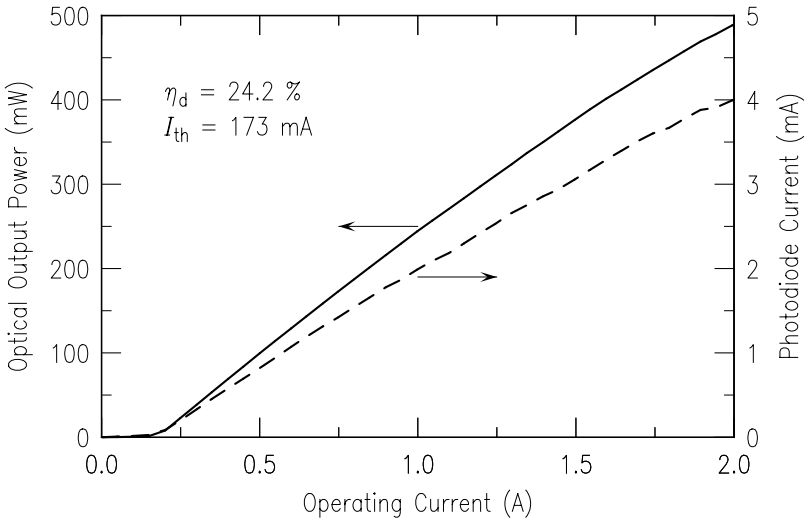

Fig. 5. Comparison of the optical output power (solid line) and the current of the integrated monitor diode (dashed line).

3. Characterization

Figure 4 shows the cw characteristics of a 1000 μm $\cdot$ 100 μm uncoated device at room temperature. To remove the dissipated heat, the laser chip is glued junction-side up by a two-component epoxy on a copper heat sink. An optical output power of approximately 800 mW per facet is achieved measured with an calibrated integrating-sphere detector. The threshold current density and the differential quantum efficiency are $j_{\mathrm{th}} = 162\,\mathrm{Acm}^{-2}$ and $\eta_{\mathrm{d}} = 24.7\,\%$ per facet, respectively. At the bottom of Fig. 4 the optical output powers of 1000 μm $\cdot$ 100 μm lasers having different galvanic heat spreader thicknesses are compared.

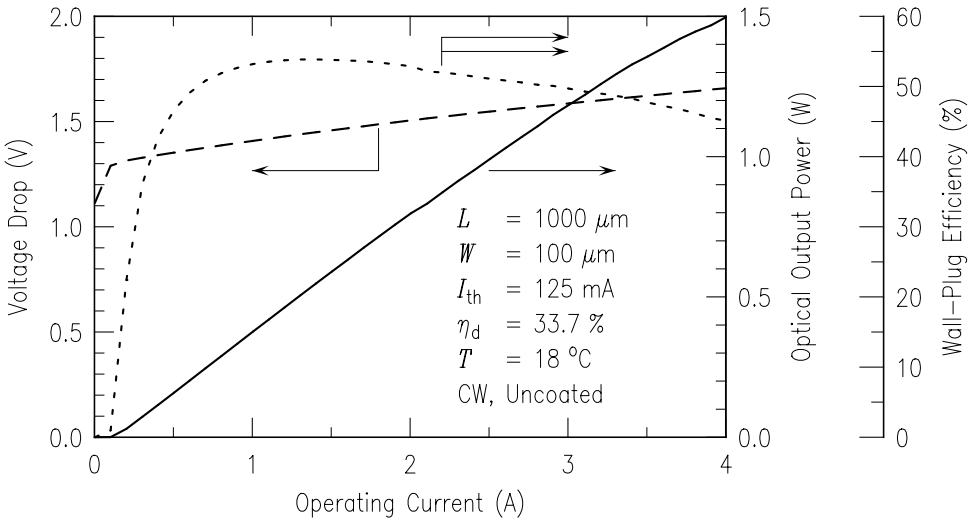

Fig. 6. Continuous operation of a junction-side-down mounted broad area laser with uncoated dry-etched facets having a cavity length of $L = 1000\,\mu$m and a lateral width of $W = 100\,\mu$m. Shown are the output power per facet (solid line), the I-V characteristic (dashed line) and the wall-plug efficiency (dotted line) of the device.

The integrated monitor diode can be used to control the optical output power of the laser during operation. Figure 5 shows the dependence of the measured monitor diode current on the operating current of the laser. For this measurement, the photodiode has been reverse biased. The monitor diode current I_{ph} increases linearly with optical output power P_{opt} according to $I_{\mathrm{ph}} = 8.2\,\mathrm{mA/W} \cdot P_{\mathrm{opt}}$.

To achieve even higher output power, the devices have been mounted junction-side down on diamond heat sinks. The resulting characteristics for continuous-wave operation are shown in Fig. 6. At an operating current of 4 A, an output power per facet of 1.5 W has been achieved for a $1000\,\mu\mathrm{m} \cdot 100\,\mu$m broad area laser with uncoated dry-etched facets. The I-V characteristic shows a kink voltage of 1.3 V and a differential resistance of $0.109\,\Omega$. The wall-plug efficiency has been calculated by dividing the optical output power of both facets by the product of operating current and voltage drop. A maximum wall-plug efficiency of 54 % has been achieved at a current of 1.2 A.

References

[1] P. Vettiger, M. K. Benedict, G.-L. Bona, P. Buchmann, E. C. Cahoon, K. Dätwyler, H.-P. Dietrich, A. Moser, H. K. Seitz, O. Voegeli, D. J. Webb, and P. Wolf, "Full-wafer technology — A new approach to large-scale laser fabrication and integration," *IEEE J. Quantum Electron.*, vol. 27, no. 6, pp. 1319–1331, 1991.

[2] S. A. Biellak, C. G. Fanning, Y. Sun, S. S. Wong, and A. E. Siegman, "Reactive-ion-etched diffraction-limited unstable resonator semiconductor lasers," *IEEE J. Quantum Electron.*, vol. 33, no. 2, pp. 219–230, 1997.

[3] M. L. Tilton, G. C. Dente, A. H. Paxton, J. Cser, R. K. DeFreez, C. E. Moeller, and D. Depatie, "High power, nearly diffraction-limited output from a semiconductor laser with unstable resonator," *IEEE J. Quantum Electron.*, vol. 27, no. 9, pp. 2098–2108, 1991.

[4] P. Unger, V. Boegli, P. Buchmann, and R. Germann, "Fabrication of curved mirrors for visible semiconductor lasers using electron beam lithography and chemically assisted ion-beam etching," *J. Vac. Sci. Technol. B*, vol. 11, no. 6, pp. 2514–2518, 1993.

[5] M. Hagberg, B. Jonsson, and A. G. Larsson, "Investigation of chemically assisted ion beam etching for the fabrication of vertical, ultrahigh quality facets in GaAs," *J. Vac. Sci. Technol. B*, vol. 12, no. 2, pp. 555–566, 1994.

[6] P. Buchmann, H. P. Dietrich, G. Sasso, and P. Vettiger, "Chemically assisted ion beam etching process for high quality laser mirrors," *Microelectron. Eng.*, vol. 9, pp. 485–489, 1989.

[7] F. Eberhard, M. Schauler, E. Deichsel, C. Kirchner, and P. Unger, "Comparison of the etching behavior of GaAs and GaN in a chemically-assisted ion-beam etching system," *Microelectron. Eng.*, vol. 46, pp. 323–326. 1999.

[8] P. Unger, V. Boegli, P. Buchmann, and R. Germann, "High-resolution electron-beam lithography for fabricating visible semiconductor lasers with curved mirrors and integrated holograms," *Microelectron. Eng.*, vol. 23, pp. 461–464, 1994.

COMD Behavior of Semiconductor Laser Diodes

Ulrich Martin

The lifetime of semiconductor laser diodes is reduced by facet degradation and catastrophical optical mirror damage (COMD). To increase the lifetime of such devices, a suitable facet coating combined with a suitable preparation before the coating process is necessary. The determination of the time-to-COMD behavior provides a measure for the quality of the facet coating.

1. Introduction

Edge-emitting semiconductor lasers are used for different applications in our daily work. When making a telephone call over long distance, an optical fiber transmission system is used with a semiconductor laser as transmitting source. Printing systems and data storage applications often use semiconductor lasers as light source. Considering all these applications, laser diodes have to work reliable without sudden failures and degradation effects. Especially the very high power densities at the facet of a semiconductor laser can destroy the device itself. So, a suitable protection to reduce chemical and thermal effects at the laser facet is necessary to increase the lifetime of the devices.

2. COMD Mechanisms

The mechanisms of facet-related degradation are illustrated in Fig. 1. The COMD-behavior can be schematically illustrated by a number of related loops and has been described by many researchers [1],[2]. A facet oxidation loop, a loop for dislocations at the facet, and some related phenomena are physically connected with the overall COMD loop. When light is absorbed at the facet, electron-hole paires are generated and this pair generation enhances the bond breaking. The generated electrons and holes recombine nonradiatively and the temperature is increased at the facet. By this way, the band gap energy is reduced and the light absorption at the facet increases and more electron-hole pairs are generated. In the final stage, the temperature rise reaches the melting point of the laser material and COMD occurs. On the other hand facet oxidation is enhanced by the increase in bond breaking resulting in even more electron-hole pair generation. This photo-enhanced oxidation process can be understood as a defect injection process in the active area of the laser [1]. Fig. 2 shows the active area of a $4\,\mu$m ridge waveguide laser after COMD occurs. For lasers with facet coating, nonradiative recombination also occurs via the electronic states at the interface between the laser material and the coating.

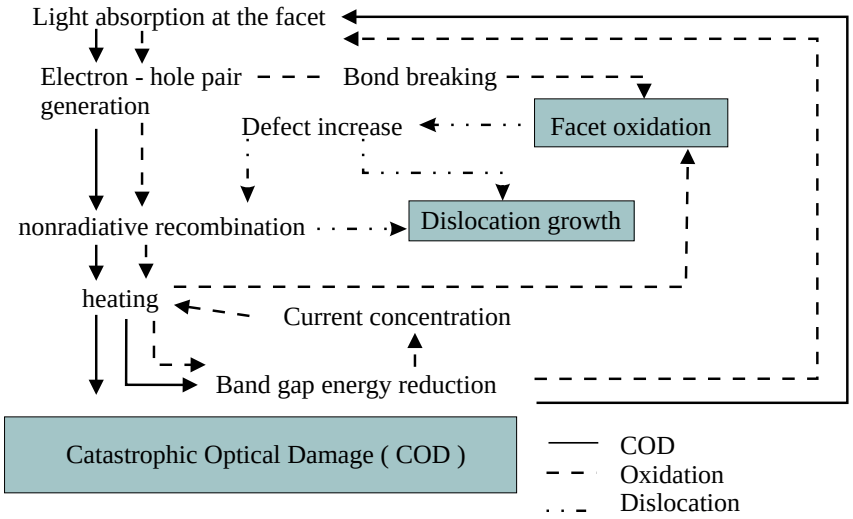

Fig. 1. The mechanisms of facet-related degradation of edge- emitting lasers.

Consequently, COMD also occurs in lasers with facet coating films although the COMD power level increases because of the lower density of the interfacial states compered to the density of the surface states and because of thermal conductivity of the films [3],[4],[5]. So a suitable design with respect to good thermal contactivity at the facet and good adhesion to the facet together with chemical and mechanical stability can shift the COMD level to high output power and increases the lifetime of the device.

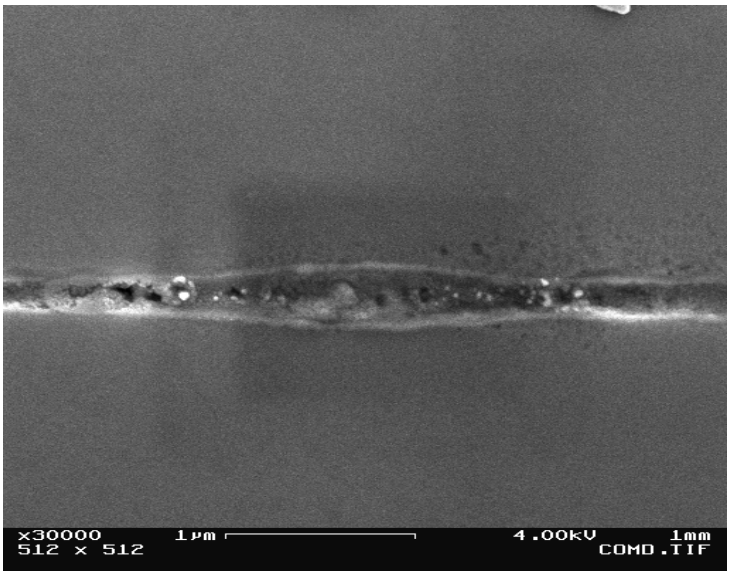

Fig. 2. Active area of a 4-μm ridge waveguide laser after COMD occurs

3. Devices for Lifetime Tests

To measure the COMD behavior, single-mode ridge-waveguide lasers are used. Fig. 3 schematicaly shows the structure of such a ridge-waveguide laser.

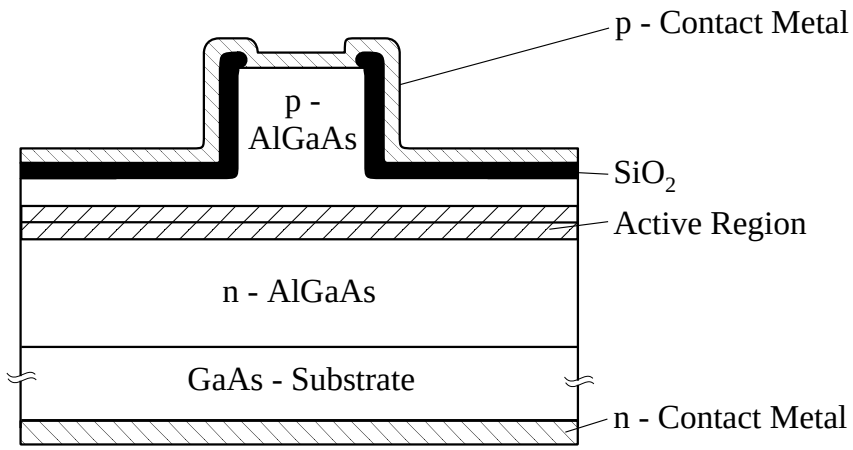

Fig. 3. Schematic structure of a ridge waveguide laser

The active region consists of an epitaxially grown graded-index separate confinement heterostructure (GRINSCH) with an InGaAs quantum well. The lateral emission region is defined by an etched laser ridge at the semiconductor surface which builds an optical waveguide because of the resulting index step. The device is contacted by a p-contact on top of the ridge and an n-type contact at back side of the substrate material. The output characteristic of such a device is shown in Fig. 4.

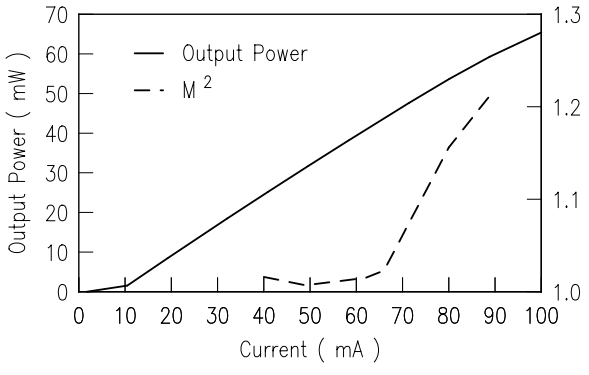

Fig. 4. Output power and beam quality versus laser current for a 4-μm ridge-waveguide laser.

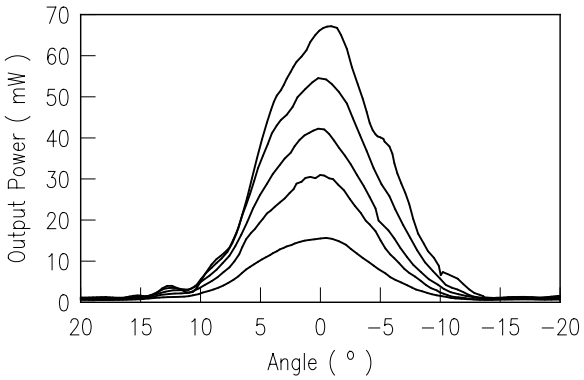

Fig. 5. Lateral far-field pattern of the 4-μm ridge-waveguide laser.

The device has a threshold current of about 12 mA and a differential efficiency of about 78 %. The beam quality which is descibed by the M^2 value is nearly 1 if the output power is below 10 mW. Up to an output power of less than 55 mW, the M^2 value increases to 1.2 . The picture

on the righthand side (Fig. 5) illustrates the lateral far-field behavior of this device at different output power levels. So the lateral full width at half maximum angle is less than 14^0 .

4. Time to COMD Measurement

The correlation between time to COMD and the aging condition has been studied for InGaAs/GaAs strained quantum well lasers by a group at IBM Zurich [6]. They have reported the following empirical relationship for InGaAs/GaAs strained QW lasers.

$$1/t_{\mathrm{COMD}} = \nu e^{-\frac{E_a}{kcPD}}, \tag{1}$$

where $1/t_{\mathrm{COMD}}$ represents an Arrhenius like "COMD reaction rate", k and c are the Boltzmann constant and the temperature proportionally term. PD is the optical power per unit μm ridge width. The pre-exponential factor (ν) and the activation energy (E_{a}) are characteristic for the materials and for the procedure used to prepare the facet of the InGaAs/GaAs lasers, namely cleaving with air exposure. Before trying to influence these parameters with the aim to get a better COMD behaviour, we have measured an uncoated laser as reference device. A laser bar has been mounted on a copper heat sink. Each laser on the bar has been operated at a different output power and the time to COMD has been determined. An example for such a measurement at 75 mW output power is shown in Fig. 6.

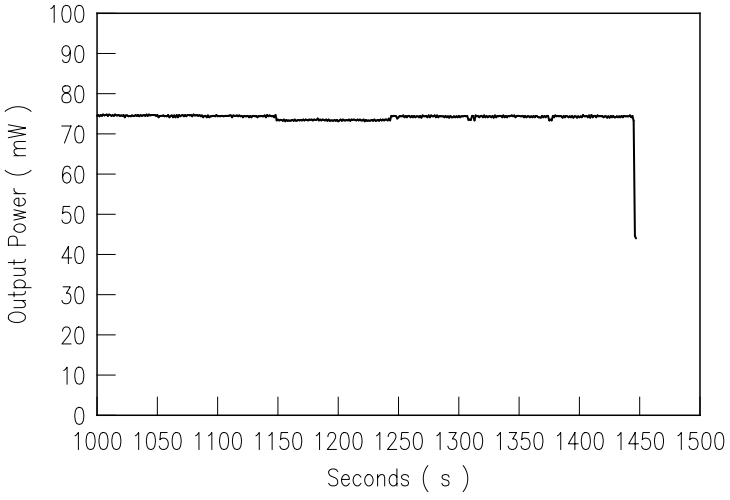

Fig. 6. Output power versus lifetime of a 4-μm ridge-waveguide laser.

The resulting output power is constant over a long time until the COMD occurs and the device is destroyed. All the results of these measurement were plotted in Fig. 7. By fitting the measured values, the pre-exponential factor ν and the activation energy E_{a} can be determined. To reduce the fit error of this plot, measurements for long time at low power levels are needed which will be done next. After this, different kinds of facet preparations will be done to get a better facet quality.

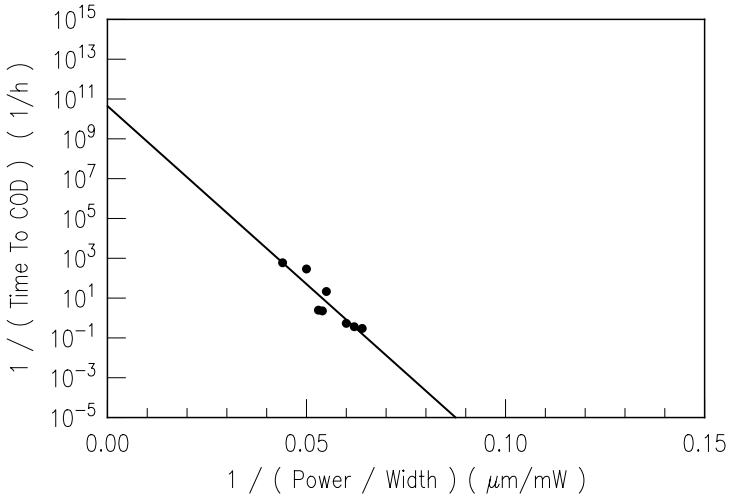

Fig. 7. Arrhenius plot of 4-μm ridge-waveguide lasers cleaved at air exposure without any coating.

References

[1] M. Fukada, *Reliability and Degradation of Semiconductor Lasers and LEDs*, Artech House, 1991.

[2] O. Ueda, "Degradation of III-V optoelectronic devices", *J. Electrochem. Soc.*, vol. 135, 11C–22C, 1988.

[3] H. Imai, M. Morimoto, H. Sudo, T. Fujiara, and M. Takusagawa, "Catastrophic degradation of GaAlAs DH laser diodes", *Appl. Phys. Lett.*, vol. 33, pp. 1011–1013, 1978.

[4] H. Brugger, P. W. Epperlein, S. Beeck, and G. Abstreiter, "Local operating temperatures in GaAs quantum well lasers", *Inst. Phys. Conf. Ser.*, vol. 106, pp. 771–776, 1989.

[5] H. Brugger, P. W. Epperlein, "Mapping of local temperature on mirrors of GaAs/AlGaAs laser diodes", *Appl.Phys. Lett.*, vol. 56, pp. 372–3732, 1979.

[6] A. Moser, A. Oosenbrug, E. E. Latta, Th. Forster, and M. Grasser, "High-power operation of strained InGaAs/AlGaAs single quantum well lasers", *Appl. Phys. Lett.*, vol. 59, pp 2642–2644, 1991.

High-Power Semiconductor Laser Amplifiers with Optimized Active Material

Frank Demaria, Eckard Deichsel and Roland Jäger

The amount of diffraction limited power that can be obtained from broad-area semiconductor laser amplifiers is limited by filamentation. Lateral inhomogeneities in the effective refractive index and the lateral intensity distribution interact in a way that results in a number of narrow filaments. Filamentation also decreases the COMD optical power level because of increased maximum intensities at similar optical powers. Devices with broad optical near field with an effective transverse mode size of 0.474 μm have been investigated at optical output powers beyond 2 W. The pattern of the lateral intensity at its transversal maximum has been determined by measuring the lateral power distribution and taking into account the shape of the vertical mode.

1. Background

Optical waveguide structures with broad near field decrease the maximum intensity at the output facet of edge-emitting semiconductor laser devices in two ways.

- The filamentation is weaker because of the reduced interaction of the optical intensity with the effective refraction index.
- A given linear optical power density (in W cm^{-1}) results in smaller intensities (in W cm^{-2}) because of the broader effective mode size.

In combination with a spatial single-mode edge emitting laser diode, tapered laser amplifiers based on such structures show high reliability and the ability to obtain high output powers at reasonable optical intensities. Accurate junction-side-down mounting is necessary for good cooling of the facets.

The waveguide properties of the structure which has been characterized at high currents and optical powers can be described by specific quantities of its near and far field. The far-field angle of the structure is measured to be 30°. The calculated full width of the near field shown in Fig. 1 is 904 nm at its $1/e^2$-value. Normalizing the near field intensity distribution leads to a maximum value $J^0_{\mathrm{v,max}} = 2.11\,\mu\mathrm{m}^{-1}$. This is the factor, the linear optical power density has to be multiplied with to obtain the intensity value at its transversal maximum. The inverse of $J^0_{\mathrm{v,max}}$ is called the effective mode size w_{eff} [1] or equivalent transverse spot size [2]. In terms

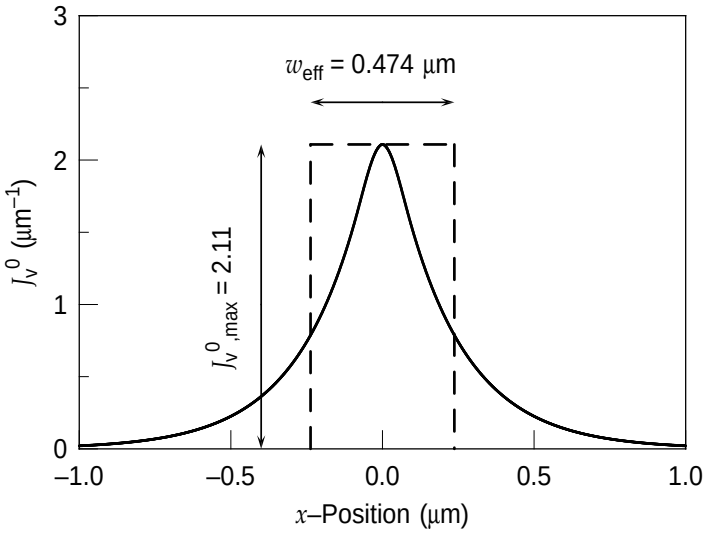

Fig. 1. Calculated and normalized transverse intensity distribution. The dashed lines show how the effective transverse mode size w_{eff} is derived from the maximum value by assuming an rectangular mode with unity integral.

of the confinement factor Γ and the width of the quantum well b_{qw} the effective mode size can be approximated as

$$w_{\text{eff}} = \frac{1}{J^0_{\text{v,max}}} \approx \frac{b_{\text{qw}}}{\Gamma}. \tag{1}$$

The width of the quantum well under discussion is 8 nm, the exact value of Γ is calculated from the overlap of J_{v}^0 (see Fig. 1) with the quantum well to be 1.67 %. The value of w_{eff} is 0.474 μm, calculated from $J^0_{\text{v,max}}$.

2. Results

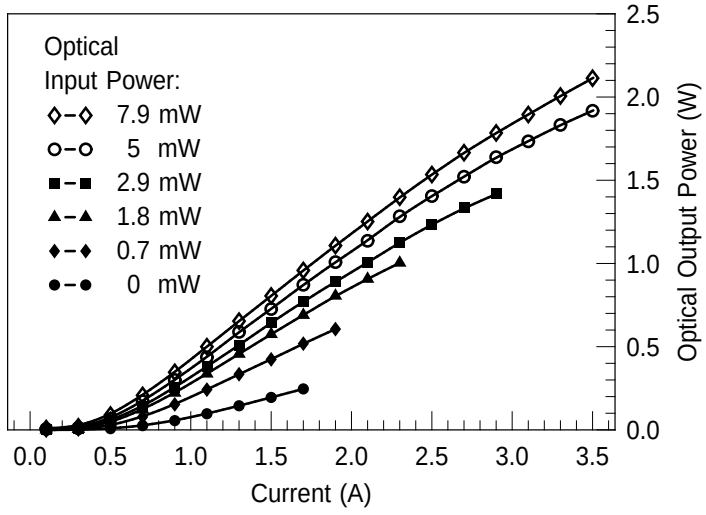

Fig. 2. Output characteristics of a laser amplifier with 7° full taper angle and a length of 2 mm. The near field distributions of the device are shown in Fig. 1 and Fig. 3 .

The output characteristics of amplifiers with the described waveguide structure and different taper angles has been determined with an computer-controlled measurement setup. In order to

keep the thermal stress caused by nonradiative recombination low, the maximum current has been limited for low optical input power. The result depicted in Fig. 2 has been achieved with a taper angle of 7 °. An output power above 2 W could be reached with a current of 3.5 A at a moderate optical input power below 8 mW. No significant thermal roll over takes place which is evidence for good mounting. The threshold current density at which amplification starts is about 25 % higher than that of comparable amplifiers with smaller w_{eff} values of 0.39 μm [3].

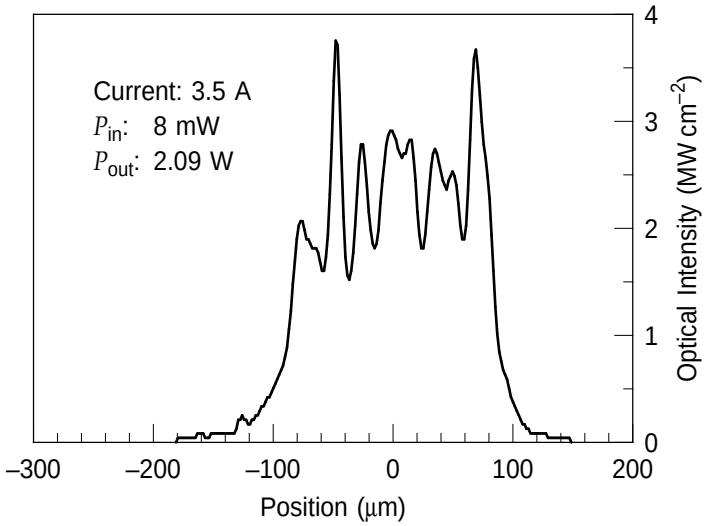

Fig. 3. Lateral intensity distribution at the output facet of the laser amplifier with 7° full taper angle and a vertical mode as depicted in Fig. 1.

The optical near field of the amplifier has been measured by scanning the optical image of the output facet. Several measurements have been performed at different currents and optical input powers. Though the device has been characterized intensively at high power levels no degradation has been observed. The result of the measurement above 2 W is depicted in Fig.3. Because of the filamentation, the maximum value of the intensity of 3.8 MW cm^{-2} is much higher than the average value of about 2.2 MW cm^{-2}. However, the tendency for filamentation is still reduced in comparison to amplifiers with smaller w_{eff} values [3].

3. Conclusion

We have shown the ability of semiconductor laser amplifiers with GRIN waveguide structures and broad optical near field to achieve optical output powers above 2 W. The w_{eff} value of 0.474 μm is comparable to that of LOC laser diodes with the capability to achieve very high output powers, $w_{\text{eff}} = 0.54\,\mu$m [1]. By taking into account the effective transverse mode size we are able to determine the accurate value of the maximum intensity from a simple measurement of the lateral optical power distribution. This is a useful concept for comparing and estimating the stress of the output facet for different waveguide structures.

References

[1] S. O'Brien, H. Zhao, A. Schoenfelder, and R. J. Lang, "9.3 w cw (In)AlGaAs 100 μm wide lasers at 970 nm", *Electron. Lett* vol. 33, no. 22, pp. 1869–1870, 1997.

[2] L. J. Mawst, A. Bhattacharya, J. Lopez, and D. Boetz, "8 W continuous wave front-facet power from broad-waveguide Al-free 980 nm diode lasers", *Appl. Phys. Lett.* vol. 69, no. 11, pp. 1532–1534, 1996.

[3] F. Demaria, *Halbleiter-Laserverstärker zur Erzeugung hoher, einfrequenter optischer Ausgangsleistung mit beugungsbegrenzter Strahlqualität*. Diploma Thesis, Dept. of Semiconductor Physics, University of Ulm, 1999.

45% Quantum Efficiency Light-Emitting Diodes with Radial Outcoupling Taper

Wolfgang Schmid

We have investigated efficient light outcoupling from light-emitting diodes (LEDs) by introducing lateral tapers. The concept is based on light generation in the very central area of a circularly symmetric structure. After propagating between two highly reflecting mirrors light is outcoupled in a tapered mesa region. By proper processing we achieve quantum and wallplug efficiencies of almost 30% for outcoupling via a planar surface or, respectively, 45% and 44% for encapsulated devices.

1. Introduction

One of the cardinal problems limiting the performance of light emitting diodes (LEDs) is their low external efficiency caused by total internal reflection of light in semiconductor material. Various approaches already exist to overcome this problem. Among those are resonant cavity LEDs with their modified internal direction of spontaneous emission [1], surface textured devices with a back side mirror where photons repeatedly try to escape [2], or the use of transparent substrates [3]. We introduced a new method of efficient light outcoupling from LEDs by introducing lateral tapers [4]. The concept is based on light generation in the very central area of a circularly symmetric structure. After propagating between two highly reflecting mirrors light is outcoupled in a tapered mesa region. In this paper we present a systematic improvement of our devices leading to record high 45% and 44% quantum and wallplug efficiencies, respectively. Devices studied use InGaAs active quantum wells and GaAs cladding layers. Emission occurs at 980 nm wavelength.

2. Principle of Operation

Fig. 1 shows the general structure of the devices studied. The active area is restricted to the center of a circularly symmetrical structure and surrounded by a tapered ring. The generated light is intended to couple out at the lower semiconductor surface.

Light can only escape the semiconductor for a small incident angle to the surface. In terms of wave vector $\vec{k}$ the in-plane part has to be small, i.e.

$$\sqrt{k_{\varphi,\mathrm{in}}^2 + k_{r,\mathrm{in}}^2} \leq \left|\vec{k}_{\mathrm{out}}\right| \ ,$$

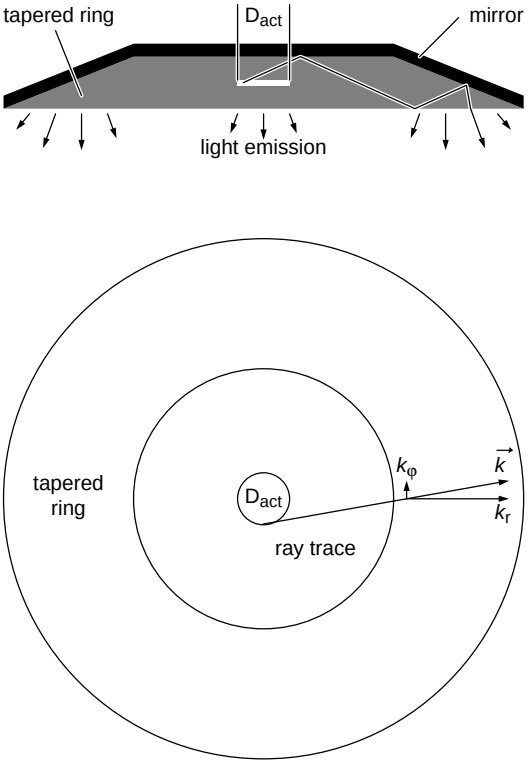

Fig. 1. The upper part indicates the simplified cross-sectional structure of the circularly symmetrical device investigated. The semiconductor has a shape of an extremely flat truncated cone, which is covered by a mirror. The light is guided radially towards a taper where it is redirected. Outcoupling is only effective when light hits the taper surface with small azimuthal wave vector component k_φ. The lower sketch indicates that this condition is simply met by restricting the cross section of the active area.

where $k_{\varphi,\mathrm{in}}$ and $k_{r,\mathrm{in}}$ are the azimuthal and radial component inside the semiconductor, respectively, and $\vec{k}_{\mathrm{out}}$ is the wave vector outside. Since outcoupling requires both components to be small only a negligible part of light is emitted directly below the active area. The major part of the generated light undergoes total internal reflection and is guided to the taper using an effective back-side reflector. Since the azimuthal component is inversely proportional to the distance from the center it is kept small simply by restricting the active area. The radial component is reduced by successive reflections at the taper surface. Therefore, each initial elementary ray can contribute to the optical output power. A more detailed description is presented in [4] where rough design rules are given.

3. Device Processing

Fig. 2 shows the processing route to form the tapered structure. After MBE growth a few hundred nm thick pedestal with the outer diameter corresponding to the intended device is wet chemically etched. Photoresist is deposited and circularly structured with a slightly smaller size. In a reactor with a well defined temperature and organic solvent concentration the photoresist reflows to the edge of the pedestal and takes a lens shaped form due to surface tension [5]. Using ion beam etching with low selectivity the structure is partially transferred into the semiconductor. The remaining photoresist is removed leading to a flat top surface surrounded by a tapered ring as shown in the SEM picture in Fig 3.

A GeNiAu metallization is deposited on the outer n-type part of the taper serving as n-contact.

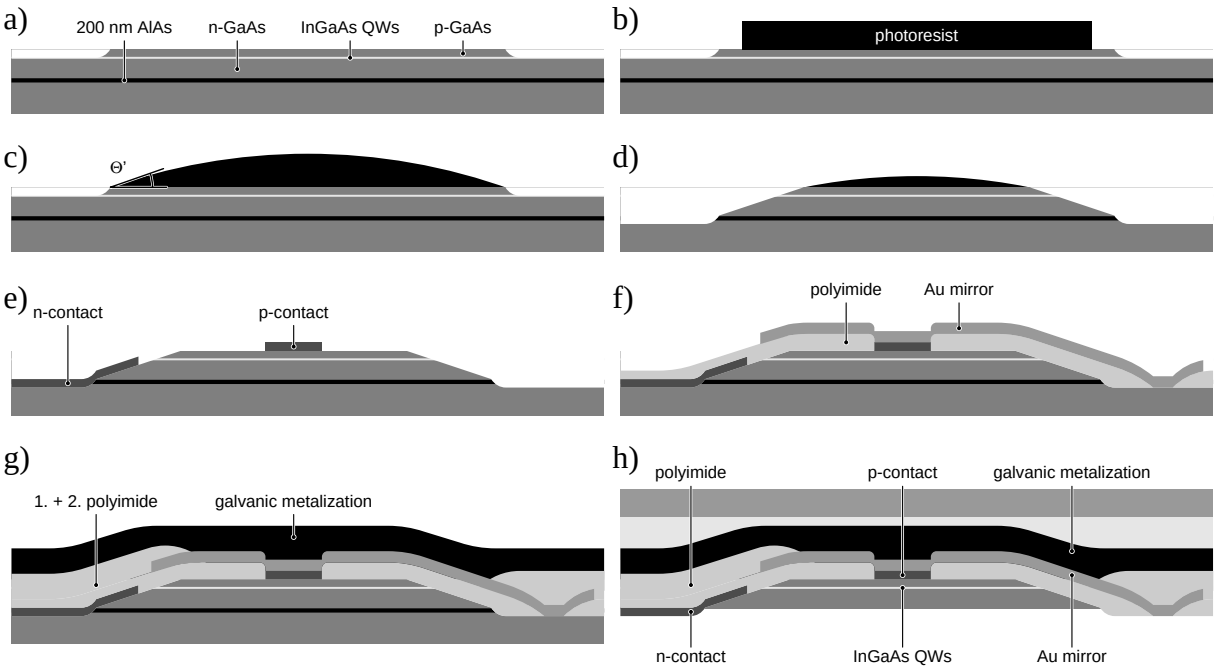

Fig. 2. Processing steps for a tapered LED. After wet-etching of a pedestal in the upper p-type GaAs cladding layer (a) a structured photoresist (b) becomes lens-shaped after treatment in a solvent atmosphere (c). Using chemical-assisted ion-beam etching the structure is partly transferred into the semiconductor; (e) n- and p-contact are deposited, (f) an Au mirror is deposited onto a first passivation layer, (g) a homogeneous metallization is deposited onto a second passivation layer and galvanically enhanced, (h) substrate and etch stop layer are removed.

Since the reflectivity of the contact metallization is low only a small fraction, more precisely a quarter of the ring is covered by the metal. The p-type contact is realized as a small circle on the center of the top surface. Moderate p-doping and high n-doping levels of the cladding layers prevent current spreading in the active layer. Light generation occurs in an area just slightly larger than the p-contact size.

For passivation of the pn-junction at the taper surface we use polyimide layers which are opened at the central p-contact area. As shown later, outcoupling is improved by thin polyimide layers. However, the typical thickness of 400 nm is not sufficient to passivate the n-contact. Therefore, we have to avoid lateral overlap of the following mirror metallization with the n-contact, as indicated in Fig. 2f). Fig. 2g) illustrates that a second thicker passivation layer is used to cover the n-metallization. The thickness of a top metallization is galvanically increased to form a quasi substrate. After gluing the wafer upside down on a glass carrier, the substrate is chemo-mechanically thinned down to 50 μm. Finally the substrate is selectively etched with an H_2O_2:NH_4OH solution where the pH is adjusted to 8.1 [6]. In this way the n-contact appears at the surface and can be used for independent addressing current supply.

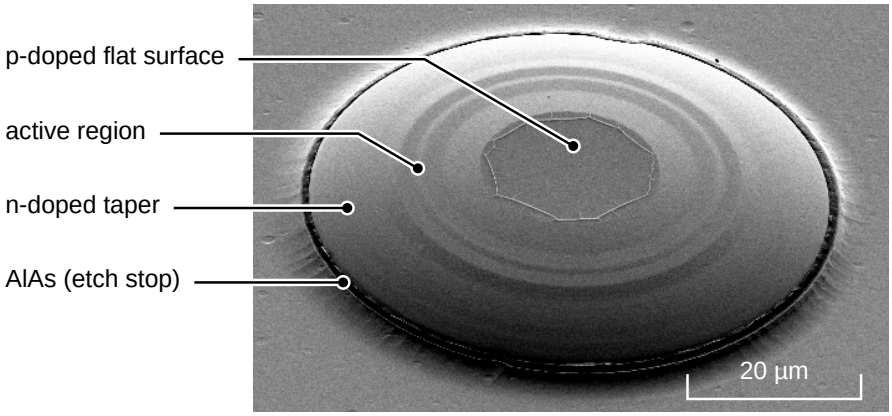

Fig. 3. SEM picture of a structured semiconductor.

4. Optimization of Efficiency

Early devices based on lateral taper outcoupling have shown quantum and wallplug efficiencies of about 15% [4]. Here we want to show our systematic improvement of the device characteristics. We consider p-type contact, advanced passivation technique, and lateral device size.

For measurement of the optical output power we use an integrating sphere. The spectrum is recorded with a conventional spectrum analyzer. For simple calibration we take the sensitivity of the photodiode-sphere system at the peak wavelength. Since the spectrum has a large short wavelength tail this method is not very precise. The calculated efficiencies are therefore not very accurate but nevertheless should give a good indication of the relative influences of various processing methods.

For comparison a state-of-the-art device was analyzed at OSRAM, Regensburg, using a calibrated power meter which takes the shape of the spectrum into account. As shown in Section 5. this analysis leads to optical output powers being about 10% larger than in preliminary measurements. The efficiencies given in this section may therefore be only 90% of calibrated figures.

A) P-type contact

Since lateral current confinement is realized by suitable doping of n- and p-layers, the p-contact has to be close to the active area. The usual Ti/Pt/Au contact metallization shows low reflectivity. Therefore we expect considerable re-absorption of light lowering the efficiency.

In order to estimate the influence, a sample was partially covered during Ti/Pt/Au p-contact deposition. Subsequently we deposited pure Au onto the primarily unmetallized structures. In this way same processing of the remaining steps is ensured. Fig. 4 compares output characteristics of both kinds of devices. The influence on the IV-characteristics is negligible. While the Ti/Pt/Au-contacted devices have maximum quantum efficiencies η_q of 15% the high reflectivity of Au raises quantum efficiencies up to 18%.

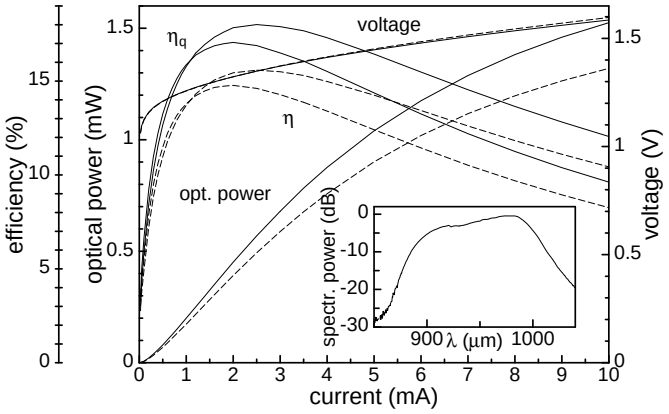

Fig. 4. Comparison of 100 μm devices with conventional Ti/Pt/Au-p-contact (dashed line) and Au-p-contact (solid line). The increased efficiency of the latter device clearly shows the improvement of using highly reflecting p-metallization.

B) Passivation

The upper left sketch in Fig. 5 illustrates strong parasitic waveguiding of polyimide passivation. This undesired effect is additionally enhanced since planarising polyimide increases its thickness especially in the critical area at the tip of the outcoupling taper. The guided light is absorbed in the adjacent Au mirror and therefore can no longer contribute to the optical output power.

In order to reduce waveguide absorption two modifications were introduced. First, polyimide of very low viscosity was used to obtain thin passivation layer as indicated in the lower left part of Fig. 5. Second, finite lateral extent of the passivation layer results in additional light ejection by endfire-like radiation. The CCD picture in Fig. 5 of a device under operation therefore shows a second luminous ring. The efficiency is improved to nearly 22% for a 100 μm diameter device.

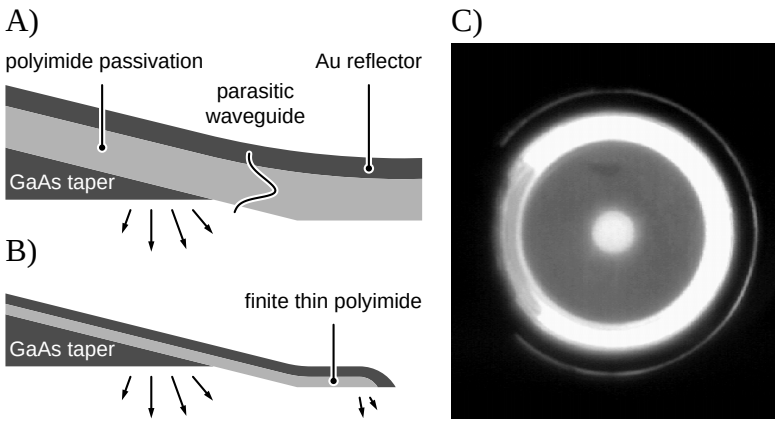

Fig. 5. A) illustrates parasitic waveguiding in the polyimide passivation layer. The influence of waveguide absorption is reduced when polyimide is of finite lateral extent and has a smaller thickness as indicated in B). In the CCD scan in C) a second illuminating ring appears due to the finite polyimide diameter.

C) Lateral size of devices

As shown in section 2., efficient outcoupling requires a small azimuthal component of the wave vector, to be realized by a small ratio of active to overall diameter. In our devices we use p-

contacts with 20 μm diameter to restrict the active area. Further lowering of the contact area is not suitable since current spreading would avoid effective reduction of active area but series resistances would increase. A better way is to enlarge the overall lateral size.

In earlier studies [4] we already presented output characteristics in dependence on up to 100 μm device diameter. Since we did not observe saturation of the maximum efficiencies versus diameter up to these sizes, larger devices were fabricated. Fig. 6 shows output characteristics for devices of 100 to 140 μm diameter. As expected, for the largest devices the highest quantum and wallplug efficiencies are achieved with values of 26% and 25%, respectively. Measurements show that the increase of efficiency starts to saturate for devices in the 140 μm range. In the future, new masks have to be designed to study size dependence in even more detail.

An obvious advantage of larger devices is the reduced saturation of output power for higher currents. This behavior can be explained by different effects. Thermal conductivity to the homogeneous top metallization increases with overall lateral size. Lower temperature means lower leakage current over non-perfect heterobarriers and therefore larger internal efficiencies. Also the extraction efficiency of a large device is less sensitive to the slight increase of the effective active diameter occurring for increased currents.

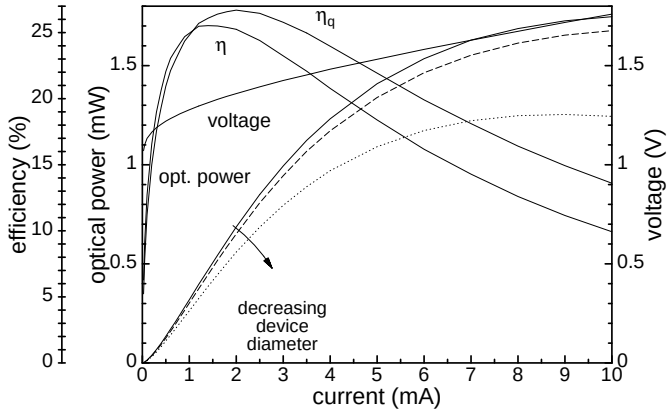

Fig. 6. Output characteristics for devices of 100 (dotted), 120 (slashed) and 140 μm diameter (solid).

5. Encapsulation

Commercial LEDs of planar geometry rely upon their efficiency from encapsulation in material with high refractive index to provide reasonably high external efficiencies. To apply encapsulation to our substratless devices minor changes in the final processing route are required. To this end the galvanic metallization is deposited with small ditches allowing separation of individual devices after removing of the substrate. The devices are mounted upside down on a TO-46 socket using silver glue or Pb/Sn solder. The n-contact is bonded to a pin. For casting we use UV sensitive glue of 1.48 refractive index. A drop of glue is simply put on the sample and hardened with UV light. Compared to epoxy casting this technique has the disadvantage of giving a not perfect hemispherical shape but handling is much easier.

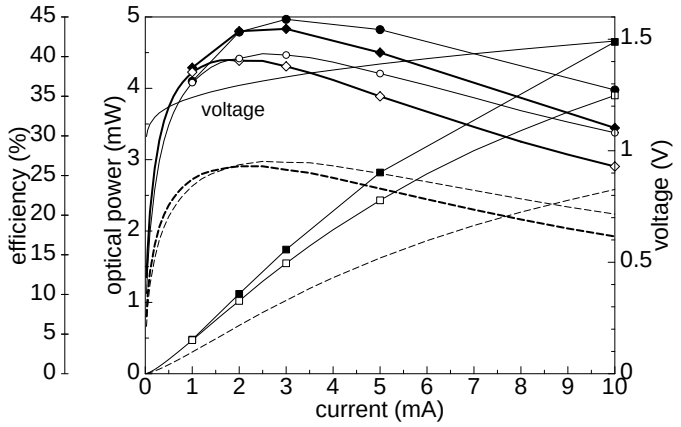

Fig. 7. Device characteristics of a 140 μm diameter device encapsulated in a medium with a refractive index of 1.48. Dashed (solid) lines are characteristics before (after) encapsulation. Open symbols represent own measurements calibrated on the peak wavelength of the emission spectrum while filled symbols are more exact measurements performed at OSRAM taking the whole emission spectrum into account for calibration.

Fig. 7 compares output characteristics before and after casting. Casting raises the output power by a factor of about 1.5. leading to quantum and wallplug efficiencies of about 40% applying our simple measurement method. As mentioned at the beginning of section 4. we performed calibrated optical power measurements at OSRAM which are assumed to be more accurrate. These measurements result in quantum and wallplug efficiencies of 45 and 44%, respectively, which are the highest reported so far in the 980 nm emission wavelength regime. Assuming the same inaccuracy in the measurements of non-encapsulated devices quantum and wallplug efficiencies in this case should be close to 30%.

6. Conclusion

We have presented a detailed processing route for fabricating efficient tapered LEDs. By systematic changes of processing we have achieved quantum and wallplug efficiencies near 30% for outcoupling via planar surface. Encapsulation in a medium with a refractive index of 1.48 raises quantum and wallplug efficiencies up to 45% and 44%, respectively.

Acknowledgment

The authors like to thank Dr. C. Jung and M. Scheubeck at OSRAM, Regensburg, for calibrated measurements. This work is supported by the “Deutsche Forschungsgemeinschaft” under contract No. EB 83/10-1.

References

[1] H. D. Neve et al., “Recycling of guided mode light emission in planar microcavity light emitting diodes,” *Appl. Phys. Lett.* **70**, pp. 799–801, 1997.

[2] R. Windisch et al., "Light-emitting diodes with 36 % external quantum efficiency operating at 600 Mbit/s," *ECOC'99* **II**, pp. 306–307, 1999.

[3] M. R. Krames et al., "High-power truncated-inverted-pyramid $(Al_xGa_{1-x})_{0.5}In_{0.5}P$/GaP light-emitting diodes exhibiting $>$50% external quantum efficiency," *Appl. Phys. Lett.* **75**, pp. 2365–2367, Oct. 1999.

[4] W. Schmid et al., "Infrared light-emitting diodes with lateral outcoupling taper for high extraction efficiency," in *Light-Emitting Diodes: Research, Manufacturing, and Applications III*, *SPIE 99* **3621**, pp. 198–205, SPIE, 1999.

[5] L. Erdmann and D. Efferenn, "Technique for monolithic fabrication of silicon microlenses with selectable rim angles," *Opt. Eng.* **36**, pp. 1094–1098, 1997.

[6] J. LePore, "An improved technique for selective etching of GaAs and $Ga_{1-x}Al_xAs$," *J. Appl. Phys.* **51**, pp. 6441–6442, 1980.

Growth of InGaAs VCSELs with Gas Source Molecular Beam Epitaxy

Matthias Golling

1. Introduction

Vertical-cavity surface-emitting laser diodes (VCSELs) are well-established optoelectronic devices nowadays. The complicated layer structure of these lasers demands a sophisticated epitaxial method. The two growth techniques widely used are the Metal-Organic Vapor Phase Epitaxy (MOVPE) and the Solid Source Molecular Beam Epitaxy (SSMBE). By using SSMBE, our department has for many years successfully grown state of the art VCSELs showing excellent output and threshold properties. Recently there is a growing interest in evaluating the possibility of using GSMBE to grow VCSELs showing similar high quality.

In this work we explore the growth of InGaAs VCSELs by GSMBE. Standard characterizations on the as-grown structures which are relevant to the VCSEL-performances will be discussed. VCSELS of different sizes were fabricated and characterized. A device with a diameter of $3.8\ \mu m$ shows CW operation at room temperature and a threshold current as low as $0.5\ mA$.

2. MBE system setup

For the growth of the samples, a modified MBE-32 system of RIBER was used. The group-III-elements aluminum, gallium and indium were evaporated from standard crucibles. As dopants, we used silicon and carbon, both provided as bromides, injected through a low temperature gas injector. The group-V-element, Arsenic, was provided by AsH_3 which was thermally decomposed into As_2 and H_2 by a high temperature gas injector. To maintain ultra high vacuum conditions during the injection of the process gas, an efficient pumping system equipped with a turbo pump and a cryo pump was used.

3. Laser design and characterization

For the evaluation of the optical quality of the materials grown described above, InGaAs quantum wells were grown. Fig. 1 shows the $10\ K$ photoluminescence spectrum of an InGaAs/GaAs single quantum well. Compared with samples grown by other MBE machines, the emission charateristic showed reasonable intensity and FWHM results. The next step towards a surface emitting laser was the design of the Bragg mirrors. In order to obtain high reflectivity, the index step chosen between the quarter wavelength thick layers has to be as high as possible. In the

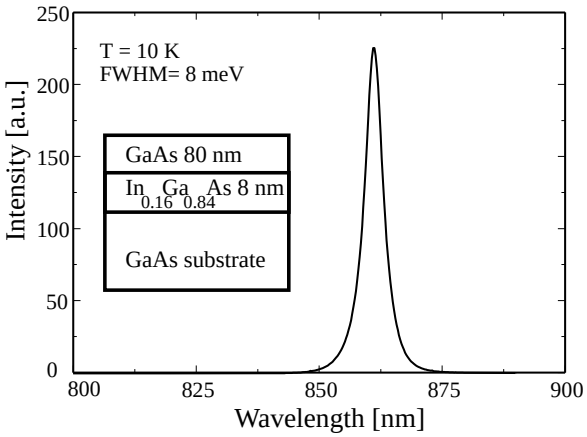

Fig. 1. PL-characteristic of InGaAs/GaAs-SQW

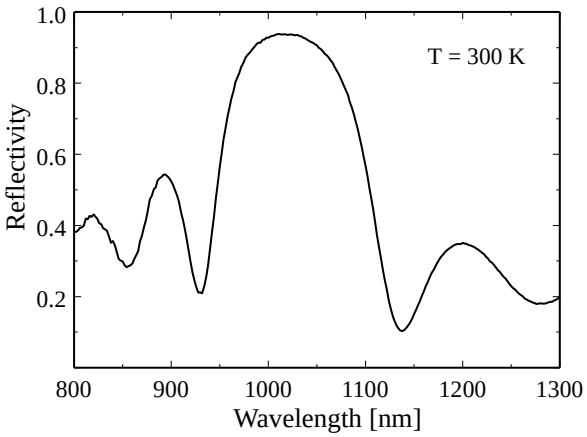

Fig. 2. Reflectance spectrum of an 8 pairs test mirror

AlGaAs system, the highest step can be achieved by using GaAs and AlAs. Considering the design of the complete VCSEL structure, we however used AlGaAs with $10\ \%$ gallium instead of pure AlAs. Fig. 2 shows a typical reflectance spectrum of an 8 pairs test mirror designed for a wavelength of $1020\ nm$.

The complete VCSEL structure consists of the active zone with three compressively strained InGaAs/GaAs quantum wells, embedded in GaAs cladding layers. On top of this cladding layer a thin AlAs layer, which serves as a current aperture by successive selective oxidation, is situated. 22 pairs of p-type doped Bragg stack form the top mirror. For the n-type bottom mirror, a Bragg stack of 32 pairs is employed.

When the wafer was processed to VCSEL devices, most of the parameters were similar to those of the devices grown by SSMBE. However, the oxidation rate of the AlAs current aperture was twice as high as for the SSMBE-grown material as illustrated in Fig. 3. The reason for this behavior has not been investigated into detail up to now. One possible influence might be the presence of hydrogen during the epitaxial growth in GSMBE.

VCSELs with diameters of $3.5\ \mu m$ to $20\ \mu m$ were fabricated. Laser diodes of all sizes showed continuous wave (CW) operation at room temperature. In Fig. 4, the output characteristics of a device with a diameter of $3.8\ \mu m$ is shown. The device shows a low threshold current around $0.5\ mA$, whereas the voltage drop of the mirrors, which are not optimized in respect of their doping profiles, is considerable. For these measurements, the lasers were not mounted on a heatsink, but measured on chip, contacted with needles. The results still leave room for improvements. However, CW operation at room temperature is a promising start for further developments.

4. Summary

We demonstrate the CW operation of InGaAs/GaAs VCSELs grown by GSMBE. In the GSMBE system used, both the Group-V-component and the dopants were provided gaseous. The pro-

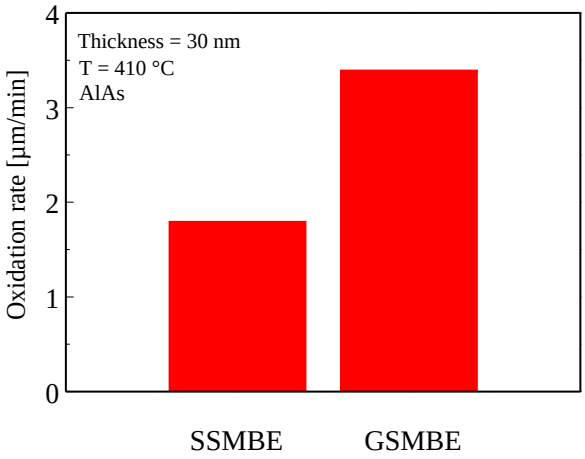

Fig. 3. Comparison of AlAs oxidation rate grown by SSMBE and GSMBE

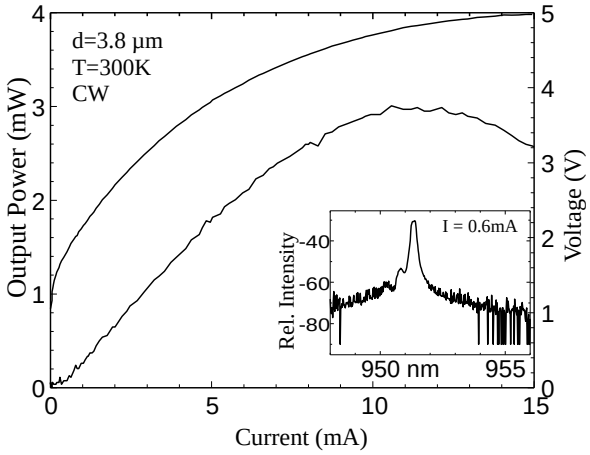

Fig. 4. CW output characteristics of InGaAs VCSEL

cessing parameters were similar to SSMBE grown material, except the oxidation rate of the AlAs layer, that was twice as high for the GSMBE grown structure. VCSELs of different size showed CW operation at room temperature with low threshold currents.

Improving Single-Mode VCSEL Performance by Introducing a Long Monolithic Cavity

Heiko Johannes Unold

We report on the improvement of several selectively oxidized VCSEL characteristics by introducing a long monolithic cavity. The samples compared are grown with various cavity lengths using solid-source MBE. The 980 nm-regime is chosen as emission wavelength to facilitate growth by using binary GaAs cavity spacers. A record high single-transverse mode output power of 5 mW at a series resistance of 98 Ω is obtained for a 7 μm aperture device with a 4 μm cavity spacer. Using an 8 μm cavity spacer, devices up to 16 μm aperture diameter emit 1.7 mW of single-mode power with a FWHM far-field angle below 3.8°.

1. Introduction

Single-mode operation in longitudinal as well as transverse direction is one of the most distinguished advantages of the vertical-cavity surface emitting laser (VCSEL). Applications for single-mode VCSELs range from Gbit/s data transmission [1] and storage over chemical analysis [2] to medical applications [3]. While longitudinal single-mode operation is inherent to the short cavity design of VCSELs, transverse mode behavior depends strongly on layer structure and device size. To date, the single-mode VCSELs with the largest lateral dimensions use proton-implanted designs [4],[5]. Selectively oxidized VCSELs offer much improved electrical and optical properties [6], except for the fact that the increased optical guiding requires much smaller aperture diameters for single-mode operation. However, small apertures cause increased series and thermal resistances, may affect device lifetime, and make mass production difficult due to tight aperture tolerances. It has already been shown that a long monolithic cavity can significantly reduce the far field angle [7]. We present the improvement of various VCSEL characteristics such as increased single-mode output power and increased-area single-mode operation due to increased diffraction losses for higher-order transverse modes and improved thermal resistance by using a long monolithic cavity.

2. Light-Current Characteristics and Transverse Mode Behavior

Fig. 1 shows a comparison of the light-current characteristics of 7 μm-aperture selectively oxidized VCSELs with 0, 2, 4, and 8 μm cavity spacers, respectively. The 0-spacer structure corresponds to our standard VCSEL structure with $In_{.19}Ga_{.81}As$-quantum wells, emitting at 975 nm, as described e. g. in [8]. The GaAs cavity spacers are incorporated between the active region

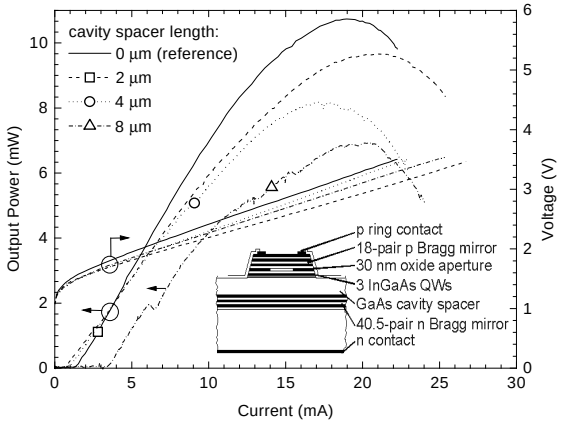

Fig. 1. Light-current and voltage-current characteristics for 7 μm-aperture devices with cavity spacer lengths 0, 2, 4 and 8 μm. Single-transverse mode operation ranges are indicated by the marked data points. The inset depicts the general VCSEL structure.

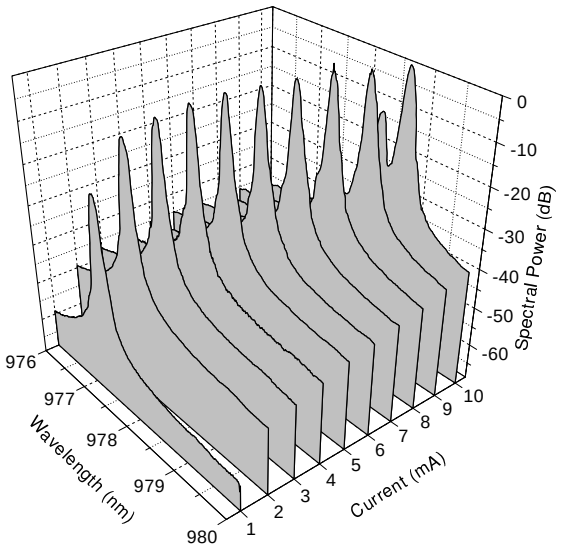

Fig. 2. Spectra of a 7 μm-aperture, 4 μm cavity spacer device for various driving currents. Single-transverse mode emission is observed up to a current of 9 mA, corresponding to a record single-mode output power of 5 mW.

and the n-type mirror as depicted in the inset of Fig. 1, allowing to obtain low resistance even for low doping levels which minimize absorption. It is seen that for cavity spacer lengths below 8 μm, the general characteristics are very similar, although there appears to be a continuous decrease in output power with increasing spacer length. For the 8 μm spacer device, threshold current is significantly increased and the general form of the curve is distorted. The increase of threshold current can be attributed to increased diffraction losses that now concern not only higher-order transverse modes but also the fundamental transverse mode. The kink between about 6 and 6.5 mA is caused by longitudinal mode switching. Smaller bumps can be attributed to transverse mode changes. Even though the cavity spacer layer is only lightly doped, series resistance shows no significant increase with increasing cavity length. For the following spectra measurements, a spectrum analyzer with a maximum resolution of 0.1 nm is used; maximum single-mode output is determined by 30 dB side-mode suppression ratio (SMSR). Maximum single-transverse mode operation conditions also indicated in Fig. 1 by the marked data points reveal that the 8 μm-spacer device possesses the largest transverse single-mode current range but exhibits longitudinal mode switching as mentioned before. The 4 μm-spacer device, however, oscillates on one longitudinal and transverse mode up to a current of 9 mA and therefore exhibits the largest single-mode output power. The maximum value of 5 mW is to our knowledge the highest single-mode VCSEL output power reported to date. Additionally, since this device is significantly larger than conventional single-mode devices, the series resistance of 98 Ω is the lowest value measured for such a high single-mode output power.

Fig. 2 shows spectra for this device for various driving currents, revealing that the first higher-

order mode is suppressed below measurement capabilities, meaning well below 30 dB up to a current of 9 mA. Here, one of the main advantages of the cavity spacer becomes apparent: due to the increased diffraction losses of higher order modes, caused by their larger diffraction angle, the single-mode current range of standard VCSELs can be increased significantly. Whereas standard devices exhibit multi-mode emission already at threshold for aperture diameters exceeding about 6 μm, even 16 μm-aperture devices have shown a significant single-mode current range for the 8 μm cavity spacer sample. Since these large devices possess a very small transverse mode spacing, single-mode operation cannot be easily derived from common spectra measurements anymore. Single-mode emission is therefore determined by recording the far field profile, yielding a maximum distinguishable SMSR of about 20 dB (see section 3.).

3. Far-Field Measurements

In addition to standard characterization and spectra measurements, the different samples are also analyzed using near-field and far-field profile analysis. The scanning near-field analysis clearly shows that index guiding decreases with increasing cavity spacer length. Also, the additional longitudinal modes show significantly increased guiding as expected from the standing wave patterns. Apart from identifying individual transverse modes, measurement of the far-field full-width half-maximum (FWHM) angle versus device current can also serve as a means to determine transverse single-mode emission, especially for larger devices where transverse mode spacing is too small to be clearly distinguished in spectra. Fig. 3 shows the far-field FWHM angle for different devices of about 12 μm aperture as a function of current. The reference device without cavity spacer represented by the filled squares exhibits a large angle already at threshold, which increases strongly with current, indicating transverse multi-mode emission. For devices with cavity spacers, the angle remains almost constant for a certain current range, until it increases abruptly. Comparing this to spectra measurements on smaller devices, it is found that this kink occurs at about 20 dB SMSR. Therefore, using long enough cavity spacers serves to increase the transverse single-mode range of large devices as well. Using this approach, we have found devices with up to 16 μm apertures emitting 1.7 mW of single-mode output power with a FWHM far-field angle of below 3.8 °.

Assuming a Gaussian index distribution in the VCSEL, the far-field angles can be normalized using the square root of the aperture diameter. This results in a layer structure specific diffraction angle independent of device size. When comparing these normalized far-field angles for the different device structures, it is found that the length of the cavity spacer is of no significant influence. Therefore, the long monolithic cavity itself does not influence the far field angle but is just responsible for the fact that larger area single-mode devices can be obtained which show low-divergence angle emission [7].

The normalized thermal resistance, on the other hand, decreases continually with increasing cavity spacer length, namely by a factor of 2 from 1.50 Kcm/W for a 0 μm spacer to 0.78 Kcm/W for a 8 μm spacer. This indicates that the additional homostructure of the cavity spacer effectively acts as a heat spreading layer which reduces the amount of heat accumulated in the active area.

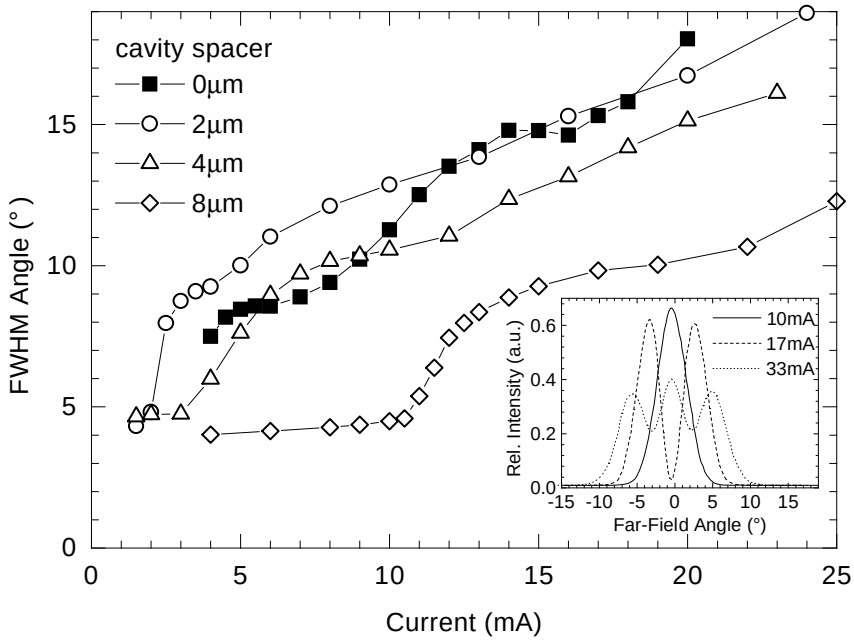

Fig. 3. FWHM far-field angle versus current for 12 μm aperture devices from all four samples of 0, 2, 4, and 8 μm spacer length. Single-mode emission with a SMSR of about 20 dB is characterized by the sudden increase of far-field angle. The inset shows the measured far-field cross-sections of the 8 μm-spacer device for currents of 10, 17, and 33 mA, corresponding to the three lowest-order modes.

4. Conclusions

We have successfully fabricated long monolithic cavity VCSELs in the 980 nm wavelength regime using n-GaAs cavity spacers of various lengths. The devices reveal significant improvements in transverse single-mode behavior and thermal resistance as a result of the increased cavity length. The far field angle is significantly reduced by realizing increased-area single-mode devices. A record single-mode output power of 5 mW is achieved for an exceptionally large device of 7 μm aperture diameter, resulting in a low series resistance of 98 Ω. A quick means of determining single-mode emission from far-field measurements with a SMSR of about 20 dB is presented, which allows to determine single-mode ranges even for large diameter devices. Longitudinal modes are observed for certain mismatch conditions of cavity resonance and gain peak, therefore providing the possibility to control them by adjusting mismatch accordingly.

References

[1] F. Mederer, C. Jung, R. Jäger, M. Kicherer, R. Michalzik, P. Schnitzer, D. Wiedenmann and K.J. Ebeling *12.5 Gbit/s data rate fiber transmission using single-mode selectively oxidized GaAs VCSELs at* $\lambda = 850\,\mathrm{nm}$, in Proc. LEOS Annual Meeting 1999, Vol. 2, pp. 697–698, San Francisco, USA, 1999.

[2] *Chip Performs Chemical Analysis,* Laser Focus World, Vol. 35, Issue 3, 1999. http://www.sandia.gov/LabNews/LN08-15-97/vcsel_story.html

[3] *Lasers Shed Light on Age-Related Blindness,* Laser Focus World, Vol. 35, Issue 3, 1999.

[4] K.D. Choquette, K.L. Lear, R.P. Schneider, Jr., and K.M. Geib *Cavity characteristics of selectively oxidized vertical-cavity lasers,* Appl. Phys. Lett., Vol. 66, pp. 3413–3415, 1995.

[5] M. Grabherr, B. Weigl, G. Reiner and K.J. Ebeling *Comparison of proton implanted and selectively oxidized vertical-cavity surface-emitting lasers,* in Proc. Conf. on Lasers and Electro-Optics Europe, CLEO'96 Europe, Hamburg, Germany, 1996.

[6] D.L. Huffaker, D.G. Deppe, K. Kumar, T.J. Rogers, *Native-Oxide Defined Ring Contact for Low Threshold Vertical-Cavity Lasers,* Appl. Phys. Lett., Vol. 65, pp. 97–99, 1994.

[7] D.G. Deppe and D.L. Huffaker, *High Spatial Coherence Vertical-Cavity Surface-Emitting Laser Using a Long Monolithic Cavity,* Electron. Lett., Vol. 33, pp. 211–213, 1997.

[8] H.J. Unold, M. Grabherr, F. Eberhard, F. Mederer, R. Jäger, M. Riedl and K.J. Ebeling, *Increased-Area Oxidised Single-Fundamental Mode VCSEL With Self-Aligned Shallow Etched Surface Relief,* Electron. Lett., Vol. 35, pp. 1340–1341, 1999.

Analysis of Longitudinal Lasing Modes in Long Cavity VCSELs

Safwat William Zaki Mahmoud

Lasing mode switching between two longitudinal modes is observed in transverse single-mode from vertical-cavity surface-emitting lasers (VCSELs) with an extended cavity through the incorporation of an n-doped GaAs spacer of thickness L_s between the active region and the n-type mirror. From measurements of the different spot sizes of the oscillating Gaussian modes with a near field scanning system, the amount of index guiding induced by the oxide layer in the VCSEL structure is determined. When $L_s = 2\,\mu$m, the fundamental longitudinal mode experiences an effective lateral index difference $\Delta n_{ox} = 4 \cdot 10^{-4}$, while this value is increased by a factor of ten for the higher order longitudinal mode. The corresponding spot size shrinkage is $17\,\%$. The thermally induced index difference decreases with increasing spacer thickness.

1. Introduction

In recent years, the performance of vertical-cavity surface-emitting lasers (VCSELs) has significantly advanced. Using selectively oxidized current apertures for fabrication, low threshold current [1] and high efficiency [2] VCSELs have been achieved. Oxide layers influence the optical field distribution in the cavity by their reduced index of refraction, producing efficient mode guiding by the induced lateral effective index difference [3]. There has been extensive interest in large area single-mode VCSELs of low electrical resistance which are especially attractive for high-speed optical communications and array applications. In particular, one approach based on a long monolithic cavity has resulted in single-mode devices with far field divergence angle of only 1.6° (e^{-2}-beam half angle) for a 30 μm aperture device [4]. In recent work [5] the incorporation of a lightly n-doped GaAs spacer of thickness $L_s = 4\,\mu$m directly underneath the active region of a 7μm aperture device has led to the highest single-mode VCSEL output power of 5mW with continuous wave (cw) operation reported to date. With this kind of device, we have observed lasing mode switching between two longitudinal modes in VCSELs with 2 and $8\,\mu$m cavity spacers. Here we report on near and far field measurements analyzing this effect in detail.

2. Device Structure and Output Characteristics

The selectively oxidized VCSEL structures for this work are grown using solid-source MBE. The standard 980 nm structure consists of a 40.5-pair n-doped $Al_{.93}Ga_{.07}As$/GaAs Bragg mirror,

three 8 nm $In_{.19}Ga_{.81}As$ quantum wells, 30 nm AlAs-aperture layer in the p-mirror pair closest to the active region and an 18-pair p-doped $Al_{.93}Ga_{.07}As$/GaAs Bragg mirror. For long monolithic cavity, a lightly n-doped GaAs spacer of thickness L_s is added directly underneath the active region. From a theoretical point of view, based on the transfer matrix method, it is found that the number of longitudinal modes is increased by increasing the cavity length. The dashed curve in Fig. 1 shows for example that for $L_s = 2\,\mu$m there exist three resonance wavelengths in the stop band of the reflectivity spectrum for such VCSEL structure. This corresponds to nearly equally spaced three longitudinal modes, labeled as $LP_{01}^{(0)}$ and $LP_{01}^{(\pm 1)}$ for fundamental and higher order longitudinal modes, respectively. We are interested here in the fundamental and one of the neighboring modes because these are the only ones producing significant laser output power. The curves in the lower part of Fig. 1 illustrate the observed emission spectra of a $4\,\mu$m aperture device with a $2\,\mu$m cavity spacer at 3.5 (dotted curve) and 4 mA (solid curve) driving current, where mode switching takes place. The mode separation of these observed modes is different from the value obtained from transfer matrix calculations by ~ 2 nm. Having

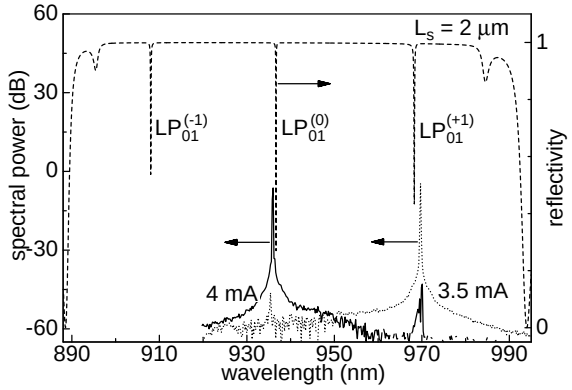

Fig. 1. Calculated reflectivity spectra (dashed curve) of our VCSEL structure with $L_s = 2\,\mu$m, measured spectra at 3.5 mA (dotted curve) and 4 mA (solid curve) for the same VCSEL structure with $D_a = 4\,\mu$m.

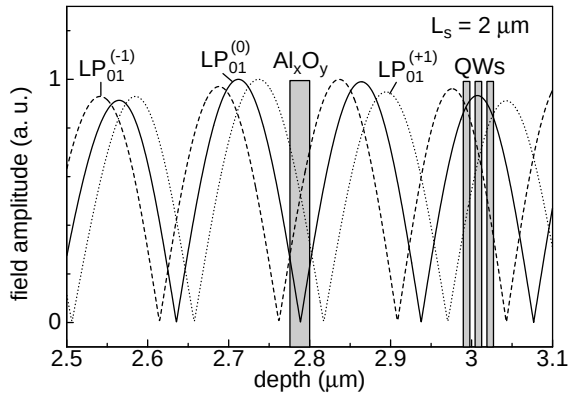

Fig. 2. The resonant standing wave patterns in the same VCSEL corresponding to the fundamental and the higher order longitudinal modes.

done the simulation of reflectivity spectrum, the electric field intensity are calculated under the assumption of a plane wave with a propagation constant defined by the respective resonance wavelengths. As seen from Fig. 2, the oxide layer Al_xO_y is centered at a node of the $LP_{01}^{(0)}$ optical field while it is shifted from the node for the $LP_{01}^{(\pm 1)}$ fields and as a result, the latter experience much larger index guiding. Figure 3 shows light output characteristics of $4\,\mu$m aperture VCSEL devices with $2\,\mu$m spacer length. Emission is in the Gaussian-like fundamental transverse mode up to 7 mA. It is seen that the output power exhibits a dip at 4 mA at which switching between the $LP_{01}^{(+1)}$ and $LP_{01}^{(0)}$ modes takes place as illustrated also by the spectra in Fig. 1.

3. Experiment and Analysis

A) Near field analysis

Near field measurements are done with a fiber tip scanning technique. In Fig. 4 the setup for near filed measurements is depicted. It mainly consists of a high precision 3-dimensional piezoelectrically driven stage and digital control electronics. Within the travel range of $100\,\mu$m for the three directions, the spatial resolution is better than 50 nm. The optical output power from the VCSEL is launched into a single-mode optical fiber whose tip has a semispherical lens with radius of curvature R. By placing the sample at the focal plane of the lens, the optical power coupled into the fiber is maximum and the distance to the beam waist is the focal length $f = R/n - 1$ [6], where n is the refractive index of the fiber. The 2 m long fiber used for this purpose has $6\,\mu$m core diameter and a fiber tip lens with $R = 6\,\mu$m. A multi-wavelength meter is employed to detect the frequency-resolved laser input signal with a sensitivity and frequency resolution in the order of -25 dBm and 20 GHz, respectively, for the wavelength range of interest. The system yields a complete spectrally and spatially resolved

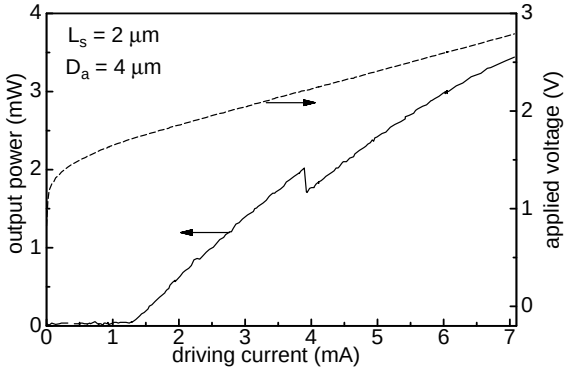

Fig. 3. Light output characteristic for a VCSEL with $D_a = 4\,\mu$m and $L_s = 2\,\mu$m.

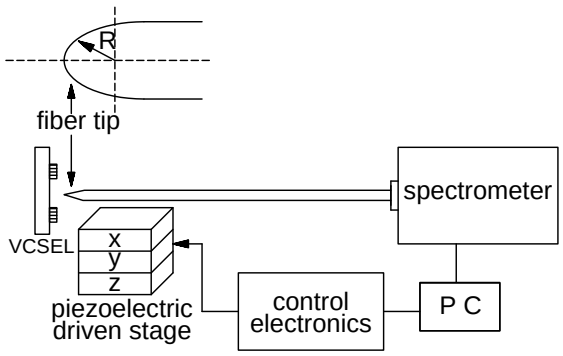

Fig. 4. Experimental setup for near field approach.

near field image of VCSEL eigenmodes. Figure 5 shows the measured e^{-2}-beam half width of the fundamental Gaussian modes versus driving current in single transverse mode with cw operation for a VCSEL with aperture diameter $D_a = 4\,\mu$m and spacer length $L_s = 2\,\mu$m. The open squares represent the data for $LP_{01}^{(+1)}$ mode and the open circles for $LP_{01}^{(0)}$ and show a sudden increase of the spot size at 4 mA where switching between these modes occurs. This means that the $LP_{01}^{(+1)}$ mode experiences much larger index guiding than the $LP_{01}^{(0)}$ mode in accordance with Fig. 2.

To understand the measurements theoretically, the circularly symmetric oxidized VCSEL structure can be approximated by a cylindrical waveguide with an effective index step Δn given by

$$\Delta n = \Delta n_{fc} + \frac{\partial n}{\partial T}\Delta T + \Delta n_{ox} \quad . \tag{1}$$

The first term represents the free carrier induced refractive index and for simplicity is set to a constant value of [7] $\Delta n_{fc} = -10^{-3}$. The second term represents the temperature dependent change of the refractive index where $\partial n/\partial T = 4 \cdot 10^{-4}$ K^{-1} and ΔT is the temperature difference between the center and the edge of the active region approximated by [7]

$$\Delta T = \frac{P_{abs}}{2\pi d\sigma} \tag{2}$$

where P_{abs} is the dissipated electrical power and $\sigma = 0.44$ W/(Kcm) the thermal conductivity of GaAs. The heat is assumed to be distributed within a sheet of thickness d encompassing the full n-GaAs spacer plus an equivalent of 40 DBR pairs. The last term in Eq. (1) describes the induced refractive index difference, based on the cavity resonance with and without the oxide aperture [3]. The e^{-2}-beam half-width w of the fundamental Gaussian mode can be obtained as in [8] under the assumption of a step index profile

$$w = \frac{D_a}{2\sqrt{\ln\left(\pi D_a \sqrt{2n_0\Delta n}/\lambda\right)}} \tag{3}$$

whereas the assumption of parabolic index profile gives w in the form

$$w = \sqrt{\frac{\lambda D_a}{2\pi\sqrt{2n_0\Delta n}}} \tag{4}$$

where λ is the wavelength of the emitted laser and $n_0 = 3.3$ the average refractive index in the VCSEL. This value is considered as that in the core of the cylindarical waveguide while for the cladding it is assumed as $n(r) = n_0 - \Delta n$ at the radial position $r = D_a/2$.
The oxide induced index difference Δn_{ox} is calculated to give $3 \cdot 10^{-3}$ for $\mathrm{LP}_{01}^{(+1)}$ and $4 \cdot 10^{-4}$ for $\mathrm{LP}_{01}^{(0)}$. According to these calculations the $\mathrm{LP}_{01}^{(+1)}$ mode experiences an induced oxide index nearly ten times that of $\mathrm{LP}_{01}^{(0)}$. Therefore the oxide induced index dominates the $\mathrm{LP}_{01}^{(+1)}$ guiding and the index profile is well approximated by a step profile. This in turn results in a spot size described by Eq. (3) which agrees well with the measured spot size as illustrated by the dashed curve in Fig. 5. Using Eq. (4) fails in reproducing these data as seen from the dotted curve in the same figure. For the weakly confined mode $\mathrm{LP}_{01}^{(0)}$ the situation is different since at 4 mA the induced thermal lensing is dominant and the index profile is approximated well by a parabolic profile. Eq. (4) fits the experimental data well as seen from the solid curve in the same figure. At the switching point these calculations show $17\,\%$ spot size shrinkage for the strongly confined mode $\mathrm{LP}_{01}^{(+1)}$ which is agreement with the measured value. If a transition from step-to parabolic-like guiding is not taken into account, this value is increased to $34\,\%$.

B) Far field analysis

Figure 6 represents the measured e^{-2}-beam half angle θ in far field approach for the same case considered in Fig. 5. These measurements are defined by open squares for $\mathrm{LP}_{01}^{(+1)}$ mode and the open circles for $\mathrm{LP}_{01}^{(0)}$ and it seems to stand on the same foot as the near field in describing the

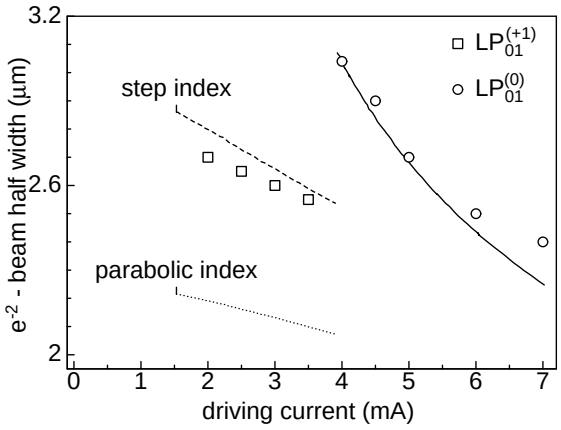

Fig. 5. Measured beam radius (open squares and circles) for the same VCSEL devices described in Fig. 3, calculated solid and dashed curves using Eq. (4) and dotted curve using Eq. (3).

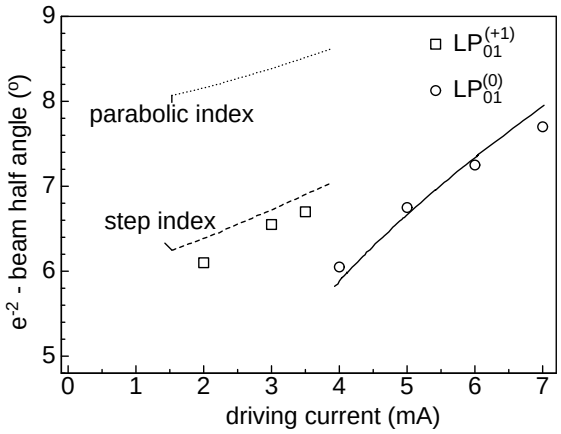

Fig. 6. Measured beam divergence half angle (open squares and circles) for the same VCSEL devices described in Fig. 5 and calculated values (solid,dashed and dotted curves).

lasing mode switching between these two longitudinal modes i.e. to show a sudden decrease in the divergence angle at 4mA. Also, the familiar formula $\theta = \lambda/(\pi w)$ could reproduce the measured data as seen in Fig. 6 by the solid and dashed curves while the dotted curve fails to reproduce the data as in the case of near field analysis.
To explain the dip observed in the optical output power at the switching point, two reasons may be drawn. Firstly, our near and far field analysis had confirmed the excitation of a weakly confined fundamental transverse mode of large spot size at this point and as a result we attribute that dip to excess scattering losses resulting from the oxide aperture. Secondly, extrapolation of the power curve in Fig. 3 from that dip at which the weakly confined mode is excited till zero gives a threshold current for the weakly confined mode larger than that of the strongly confined one. Since the optical power is directly proportional to the difference between both the pumping and threshold currents [9], we can expect the output power to be reduced at 4mA.

4. Conclusion

We have shown the longitudinal mode switching on the fundamental transverse mode in the extended cavity VCSELs which is unknown in regular structures. We have analyzed this behavior by consistent spectral as well as near and far field analysis. The lasing mode switching between two longitudinal modes in the same VCSEL device clearly shows the importance of oxide aperture induced waveguiding in such devices. The simple procedure followed throughout the present work for calculating the spot size predicts well the observed data. Due to the different overlap with oxide aperture, the modes are either dominantly guided by the built-in effective index step or the thermally induced index profile. In addition, the inversely dependence of ΔT with spacer thickness reduces the thermal lensing as the spacer thickness is increased. Physically, this means the homostructure spacer acts as a heat spreading layer, distributing the

heat generated over the whole volume and consequently reducing the accumulation of heat in the active region.

References

[1] D. L. Huffaker and D. G. Deppe, "Improved performance of oxide-confined vertical-cavity surface-emitting lasers using a tunnel injetion active region", Appl. Phys. Lett., 71, pp. 1449–1451, 1997.

[2] R. Jäger, M. Grabherr, C. Jung, R. Michazik, G. Reiner, B. Weigl, and K. J. Ebeling, "57% Wallplug efficiency oxide-confined 850 nm wavelength GaAs VCSEL's", Electron. Lett., 33, pp. 330–331, 1997.

[3] G.R. Hadley "Effective index model for vertical-cavity surface-emitting lasers", Opt. Lett.,20, pp. 1483–1485, 1995.

[4] D.G. Deppe and D.L. Huffaker, "High spatial coherence vertical-cavity surface-emitting laser using a long monolithic cavity", Electron. Lett., 33, pp. 211–213, 1997.

[5] H.J. Unold, S.W.Z. Mahmoud, R. Jäger, M. Kicherer, M.C. Riedl and K.J. Ebeling, "submitted for publication to IEEE Photonics Technology Letters".

[6] G. Grau, W. Freude, Optishe Nachrichtentechnik, (Springer Verlag, Berlin 1991).

[7] N.K. Dutta, L.W. Tu, g. Zydzik, Y.H. Wang, and A.Y. Cho, "Anomalous temporal response of gain guided surface emitting lasers", Electron. Lett., 27, pp. 208–210, 1991.

[8] A.W. Snyder and J.D. Love, Optical waveguide theory, Champan & Hall, London, 1991.

[9] K.J. Ebeling, Integrated Optoelectronics (Springer Verlag, Berlin, 1993).

Extremely Low-Noise High-Speed VCSELs for Optical Interconnects

Max Kicherer

When looking into high-speed data transmission using data rates greater than $10\,Gb/s$ *the noise behavior of the transmitter becomes more and more important. Vertical-cavity surface-emitting lasers (VCSELs) emitting at* $850\,nm$ *wavelength are characterised for this purpose. Relative intensity noise (RIN) and small signal modulation measurements have been performed and resulting spectra are fitted to theoretical curves in order to obtain internal device parameters. Different operation regimes, where transverse single- or multi-mode emission occurs, are investigated. At low temperatures the quantum efficiency of the VCSEL is increased, leading to photon-number fluctuations* $1.4\,dB$ *below the shot noise limit. A special electrical probing is used to minimize parasitics and to inhibit RF-interference.*

1. Introduction

Demonstrated CMOS speeds in the few GHz range together with the demand for ultra large scale integration turn optoelectronic interconnect technology into one of of the ideal building blocks for future high performance data links. Owing to the surface-normal operation and many other favorable properties like low power dissipation, high-speed modulation, and Si IC compatible low-cost manufacturing, VCSELs are going to be the preferred choice for the transmitter part. Single channel as well as one-dimensional fiber ribbonized parallel interconnect modules using VCSEL technology are already on the market [1, 2, 3]. Inter- and intra-cabinet data links as well as optical backplanes in advanced computer environments are target for these components [4]. In future Si IC generations electrical interconnects are foreseen to be a major bottleneck. This will open up a new area of Si CMOS and III/V optoelectronic component interaction and integration.

2. Device structure

Fig. 1 shows a schematic drawing of the crossection of a VCSEL emitting at $850\,\mathrm{nm}$. Layers are grown by solid sorce molecular beam epitaxy. The active region is formed by three $8\,\mathrm{nm}$ thick GaAs quantum wells (QWs) embedded in $Al_{0.2}Ga_{0.8}As$ barriers. The lower n-type Si-doped and the upper p-type C-doped Bragg reflector consists of $Al_{0.2}Ga_{0.8}As/Al_{0.9}Ga_{0.1}As$ quarter-wavelength layer pairs, with graded interfaces and δ-doping to reduce series resistance [5]. Current is injected through the upper Bragg reflector by a ring contact. Current confinement

is achieved by selective lateral oxidation of a $30\,\mathrm{nm}$ thick AlAs layer after mesa etching [6]. Stable single-mode emission is enforced by small oxide aperture and low optical confinement [5]. Small diameter mesa with steep side-walls are required to obtain a low oxide capacitance. Therefore, mesa are formed by chemically assisted ion beam etching (CAIBE). The mesa is passivated and a second etching step gives access to the n-doped GaAs substrate on which a large area n-contact is evaporated. After planarization with photosensitive polyimide the n-contact is electroplated up to the height of the p-contact [7].

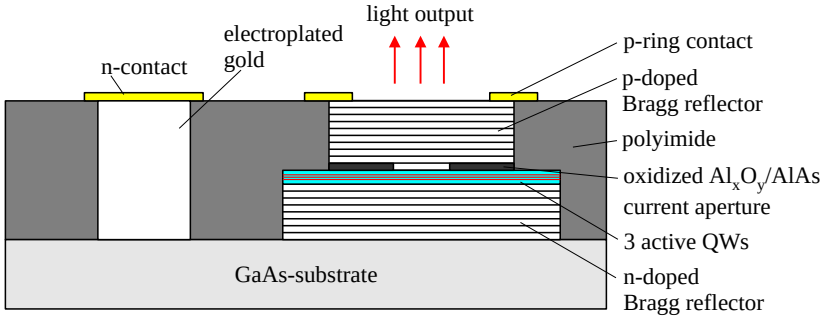

Fig. 1. Schematic drawing of the crossection of a top emittig VCSEL. The n-contact is electroplated up to the height of the p-contact.

3. Measurement setup

Fig. 2 shows the setup for RIN measurements. The VCSEL is driven by a current source in order to suppress pump current fluctuations [10]. The included bias-T serves as a low-pass filter. For measuring intensity noise, in the low frequency region, a large area Si PIN photodiode is used as light to current converter. The responsivity of the diode is approximately $0.55\,\mathrm{A/W}$ at the VCSEL emission wavelength of about $850\,\mathrm{nm}$, corresponding to a quantum efficiency of $80\,\%$. In order to measure high frequency noise components, a smaller $16\mathrm{x}16\,\mu\mathrm{m}^2$ InGaAs PIN photodiode with a bandwidth of $14\,\mathrm{GHz}$ is used. Its responsivity is approximately $0.45\,\mathrm{A/W}$. The photodiodes are always biased using a bias-T. The average photocurrent I_{ph}, which is proportional to the average light intensity, can be measured at the dc output of the bias-T. The ac current is fed to a low noise RF amplifier with a $50\,\Omega$ input resistance. For the larger detector a bandwidth exceeding $300\,\mathrm{MHz}$ is achieved. The output signal of the amplifier is transmitted to an electrical spectrum analyzer to record the power spectral density of the photocurrent. From

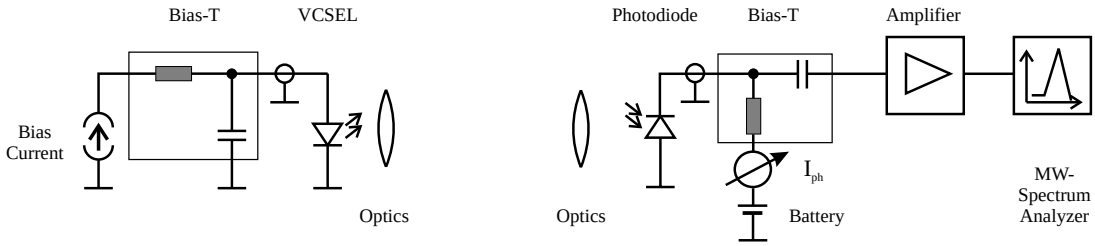

Fig. 2. Measurement setup for RIN measurements on VCSELs. Different photodiodes and amplifiers may be used, depending on the frequency range of interest.

the relation between average photocurrent I_{ph} measured at the bias-T and the power spectral density of the photocurrent at the amplifier input P_{AC}, the RIN_D is calculated according to [8]

$$RIN_D = \frac{P_{AC}}{I_{ph}^2 \cdot 50\Omega}. \tag{1}$$

For shot noise calibration the large area photodiode can be illuminated with a red-filtered halogen lamp, with the optical power adjusted to get the same average photocurrent as with the VCSEL. The shot noise limited $RIN_{D,shot}$ is given by

$$RIN_{D,shot} = \frac{2q_0}{I_{ph}}. \tag{2}$$

Calculated and measured values are in good agreement for different photodiodes. Care is taken to exclude saturation effects of the photodiode due to different spatial power density distributions of the incident light on the detector surface. Variations of the spot diameter on the photodiode at high power levels gave no changes in the measured photocurrent power spectral density.

4. Measurement results

The laser under study here has a threshold current of $I_{th} = 1.1\,\mathrm{mA}$ and emits in a single transverse mode over the whole operation range. Fig. 3 shows measured RIN_D spectra for various driving currents of this VCSEL. Fitted theoretical curves are included for three of the curves. From the theoretical description a linear dependency of the damping constant γ on the squared resonance frequency ν_r^2 can be deduced [9].

$$\gamma = K\nu_r^2 + \frac{1}{\chi\tau_{w,sp}} \tag{3}$$

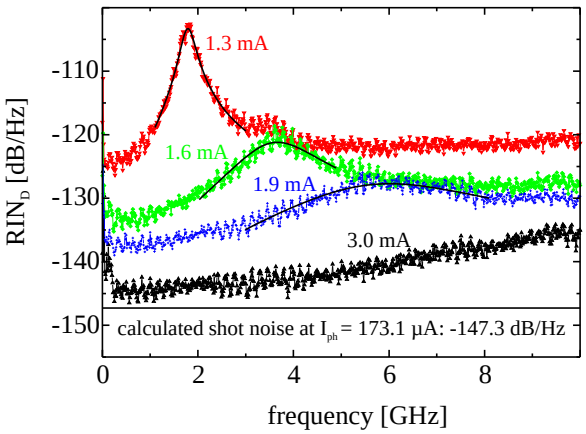

Fig. 3. Measured RIN_D spectra and fitted theoretical curves. The calculated shot noise level for the maximum photocurrent is shown as well.

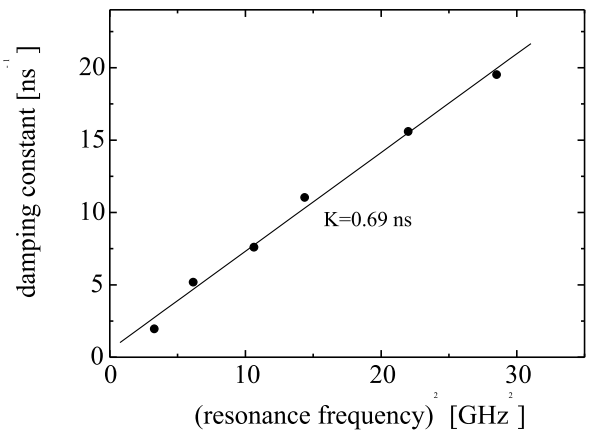

Fig. 4. Extracted values of damping constant versus squared resonance frequency. The slope of this plot is called the K-factor.

Where $\tau_{w,sp}$ denotes the spontaniou carrier lifetime and χ is a carrier transport factor. Extracted values are plotted in Fig. 4. The proportionality factor K is determined from the slope. It can be used to calculate the maximum modulation bandwidth $\nu_{3dB,max}$ of the intrinsic laser diode according to

$$\nu_{3dB,max} = \sqrt{2}\frac{2\pi}{K}. \tag{4}$$

Here it yields $\nu_{3dB,max} = 13\,\mathrm{GHz}$. Fig. 5 shows measured small signal modulation resonse curves for the same laser, again at different driving currents. The maximum bandwidth deter-

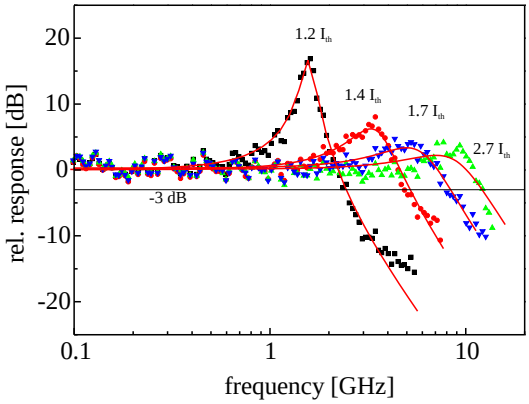

Fig. 5. Measured modulation resonse curves and fitted theoretical curves for different driving currents.

mined from these is about $12\,\mathrm{GHz}$. The good agreement of measured bandwidth and predicted bandwidth from RIN mesasurements gives no evidence of parasitics, like transport effects. In that sense the VCSEL under investigation shows purely damping limited behavior.

In Fig. 3 the calculated shot noise level for a photocurrent of $173.1\,\mu\mathrm{A}$ is shown as a horizontal line. This photocurrent is generated, when the laser is operated at a driving current of $3\,\mathrm{mA}$. In the low frequency range, the laser noise lies only a few dB above the shot noise limit.

For a different laser we have measured the low frequency RIN of the VCSEL at low temperatures. This is done to prevent early rollover of the light-current characteristics and to increase the single-mode operation range as well as the quantum efficiency. The resonance frequency of the cavity of this laser is detuned to the short wavelength side of the gain curve. Therefore, low substrate temperatures give reasonably good matching of the resonance frequency and the gain curve, depending on the bias point. No rollover of the characteristics occurs up to a current density of approximately $180\,\mathrm{kA/cm^2}$. Measurement of the emission spectrum shows operation in the fundamental mode up to currents of $3.5\,\mathrm{mA}$ with a side mode suppression of better than $30\,\mathrm{dB}$. For higher currents higher order modes begin to lase. The overall maximum quantum efficiency of the system is as high as $40\,\%$. In Fig. 6, the intensity noise of the VCSEL measured in a $1\,\mathrm{MHz}$ band around $55\,\mathrm{MHz}$ is displayed as a function of photocurrent. For comparison, the measured shot noise from the halogen lamp is also shown. From the intensity noise and the average current induced in the photodiode the relative intensity noise of the VCSEL is calculated and drawn as open circles. Above threshold, with increasing photocurrent the VCSEL intensity noise drops very fast reaching shot noise level at a photocurrent of $250\,\mu\mathrm{A}$. At a photocurrent of approximately $0.5\,\mathrm{mA}$ polarization instability causes a slight increase of

intensity noise above the shot noise level. At $1.14\,\mathrm{mA}$ photocurrent, intensity noise is $1.4\,\mathrm{dB}$ below the shot noise level. With further increased laser current, at $1.3\,\mathrm{mA}$ photocurrent a higher order mode starts lasing which results in higher intensity noise. For still higher laser currents a stable operation range is reached, and intensity noise again drops below the shot noise level. The general noise versus photocurrent characteristic is not influenced by temperature, while the increased quantum efficiency allows for an extended laser operation range and higher level of squeezing. Theoretically, from the overall quantum efficiency of the measuring system of $37\,\%$ at the corresponding bias point, a maximum amplitude squeezing of 2 dB can be expected assuming poissonian loss mechanisms [11]. The measured figure of $1.4\,\mathrm{dB}$ below the shot noise level is in excellent agreement with this theoretical prediction.

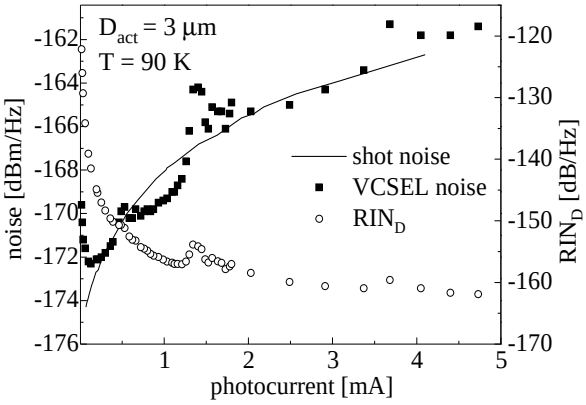

Fig. 6. Measured amplitude noise and RIN of VCSEL. For comparison the measured shot noise from a halogen lamp is included as the solid line.

5. Conclusion

We have investigated intensity noise of high performance transverse single- and multi-mode VCSELs in the $850\,\mathrm{nm}$ wavelength regime, where high quantum efficiency Si photodiodes can be used. Damping limited operation of a single-mode VCSEL has been demonstrated at room temperature. In a single-mode VCSEL emitter Si photodiode detector transmitting system with an overall quantum efficiency of $37\,\%$ an intensity noise of $1.4\,\mathrm{dB}$ below the shot noise limit has been observed at $90\,\mathrm{K}$ operating temerature of the laser. This figure is the largest amount of squeezing ever reported for VCSELs. Polarization instability, mode competition noise and thermal rollover determine the noise characteristics at room temperature. Further investigation of the non linear effects involved remains to be conducted.

6. Acknowledgment

This work was supported by the “Deutsche Forschungsgemeinschaft”.

References

[1] H. Karstensen, L. Melchior, V. Plickert, K. Drögemüller, J. Blanck, T. Wipijewski, H.-D. Wolf, J. Wieland, G. Jeiter, R. Dal'Ara, and M. Blaser, "Parallel optical link (PAROLI) for multichannel gigabit rate interconnects," in *48th Electron. Comp. and Technol. Conf., ECTC'98*, pp. 747–754, Seattle, WA, USA, May 1998.

[2] L.J. Norton, F. Carney, N. Choi, C.K.Y. Chun, R.K. Denton Jr., D. Diaz, J. Knapp, M. Meyering, C. Ngo, S. Planer, G. Raskin, E. Reyes, J. Sauvageau, D.B. Schwartz, S.G. Shook, J. Yoder and Y. Wen, "OPTOBUS^{TM} I: A production parallel fiber optical interconnect", in *Proc. 47th Electron. Comp. & Technol. Conf., ECTC*, pp. 204-209, San Jose, CA, USA, May 1997.

[3] Y.S. Liu, J. Rowlette, Y. Liu, and A. Nahata, "High density optical interconnect for board and backplane applications using polymer waveguides and VCSEL array devices", in *Proc. IEEE Lasers and Electro.-Opt. Soc. Ann. Meet., LEOS'98,*, vol. 2, pp379-380, Orlando, FL, USA, Dec. 1998.

[4] F.A.P. Tooley, "Challenges in optically interconnecting electronics", *IEEE J. Sel. Top. Quantum Electron.*, vol. 2, pp. 3-13, April 1996.

[5] B. Weigl, M. Grabherr, C. Jung, R. Jäger, G. Reiner, R. Michalzik, D. Sowada, and K.J. Ebeling, "High-performance oxide-confined GaAs VCSEL's", *IEEE J. Sel. Top. Quantum Electron.*, vol. 3, pp. 409-415, 1997.

[6] D.L. Huffaker, D.G. Deppe, K. Kumar, and T.J. Rogers, "Native-oxide defined ring contact for low threshold vertical-cavity lasers, *Appl. Phys. Lett.*, vol. 65, pp. 97-99, 1994.

[7] D. Wiedenmann, R. King, C. Jung, R. Jäger, R. Michalzik, P. Schnitzer, M. Kicherer, and K. J. Ebeling, "Design and Analysis of Single-Mode Oxidized VCSEL's for High-Speed Optical Interconnects," *IEEE J. Select. Topics Quantum Electron.* vol. 5, pp. 503-511, May/June 1999.

[8] K.J. Ebeling, *Integrated Optoelectronics*, Berlin: Springer-Verlag, 1993.

[9] K. Petermann, *Laser Diode Modulation and Noise*, Dordrecht: Kluwer Academic Publishers, 1991

[10] Y. Yamamoto, S. Machida, and O. Nilsson, "Amplitude squeezing in a pump-noise-suppressed laser oscillator", *Phys. Rev. A*, vol. 34, pp. 4025-4042, 1986.

[11] H.A. Bachor, P. Rottengatter, and C.M. Savage, "Correlation Effects in Light Sources with High Quantum Efficiency", *Appl. Phys. B*, vol. 55, pp. 258-264, 1992.

2.5 Gbit/s Data Transmission with Single-Mode GaAs VCSELs Over a -20°C to 100°C Temperature Range

Felix Mederer

Single-mode GaAs based vertical-cavity surface-emitting lasers (VCSELs) are being investigated for high bit-rate data transmission in an industrially relevant temperature range between -20°C and 100°C. The bit-error rate (BER) for 2.5 Gbit/s transmission over 250 m of graded index multimode fibre (MMF) is better than 10^{-11} for all temperatures under fixed bias and modulation conditions. The temperature dependent power penalty for 250 m MMF transmission is as low as 0.009 dB/K.

1. Introduction

Vertical-cavity surface-emitting lasers have become promising candidates for low-cost applications in optical interconnects like Gigabit-Ethernet or mobile infotainment links like the D2B in-car bus. GaAs or AlGaAs based VCSELs with threshold currents in the sub-100 μA range [1] and threshold voltages close to the bandgap voltage in combination with extremely high wallplug efficiencies over a large operation range [2] help to reduce power consumption and dissipated heat in system applications. Reported single-mode emission of 4.8 mW [3] and modulation bandwidths of 21.5 GHz [4] show the capability for ultra fast optical fiber links up to 12.5 Gbit/s data rates [5]. Earlier studies on temperature dependent data transmission at 1 Gbit/s showed power penalties in the range of 0.05 dB/K [6]. Here we report on 2.5 Gbit/s data transmission over 250 m MMF in an industrially relevant temperature range of $-20°$C to $100°$C using high-performance selectively oxidised single-mode GaAs VCSELs.

2. Experiment

The temperature behaviour of VCSELs can be optimized by adjusting the length of the Fabry-Perot resonator (FPR) and the refractive index profiles of the Bragg-reflector layers relative to the gain peak of the quantum wells. With increasing temperature, refractive indices of Bragg reflector and active layers increase resulting in a cavity mode shift of 70 pm/K whereas the peak gain shifts at a higher rate of about 0.3 nm/K. If, for a given temperature, the cavity mode is on the long wavelength side of the gain peak VCSEL performance will increase with increasing temperature. The device employed in the experiments is a selectively oxidised GaAs VCSEL

with optimised mode offset. The active diameter is about 3 μm. The VCSEL is mounted on a Peltier element for temperature control and wire-bonded to an SMA socket to keep the feeding lines as short as possible. The bias current of 2.5 mA and a 2.5 Gbit/s non-return-to-zero (NRZ) pseudo-random bit sequence signal (PRBS) with $V_{pp} = 0.6$ V are combined in a bias-tee.

The light is launched butt-coupled into a 250 m long 50 μm core diameter MMF and at the far end the light is passed through a variable attenuator and fed to a Germanium avalanche photodiode (APD). The electrical signal is preamplified and analysed with a BER detector or a fast sampling oscilloscope.

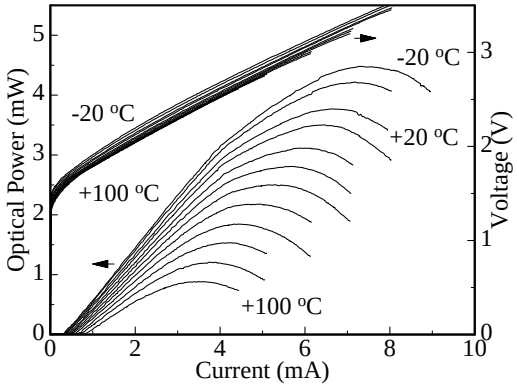

Fig. 1. Temperature-dependent output characteristics of selectively oxidised GaAs VCSEL with 3 μm active diameter.

Fig. 1 illustrates the output characteristics of the VCSEL for various heat sink temperatures between -20°C and 100°C. Threshold current and threshold voltage vary between 0.3 mA at 1.69 V for -20°C and 0.78 mA at 1.74 V for 100°C. The maximum output power varies between 4.51 mW at -20°C and 0.94 mW at 100°C for driving currents of 7.35 mA and 3.5 mA, respectively.

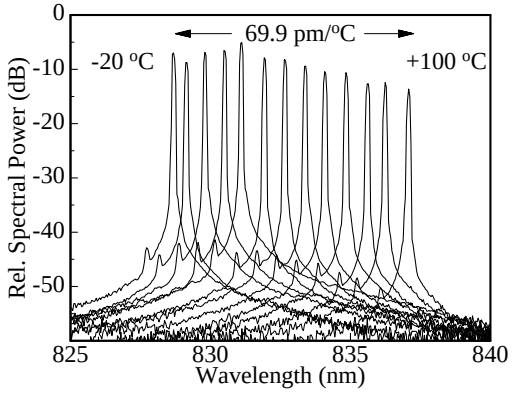

Fig. 2. Temperature dependent CW-spectra of 3 μm GaAs VCSEL at a fixed driving current of 3 mA.

The continuous wave spectra for 3 mA driving current displayed in Fig. 2 all show single-mode emission with peak wavelengths increasing from 828.7 nm at -20°C to 837.1 nm at 100°C

which is on the short wavelength side of the gain peak. The emission remains single-mode up to 4 mA driving current for all temperatures. The observed thermally induced temperature shift of 69.9 pm/K is in good accordance with the value of 60 pm/K given in [7].

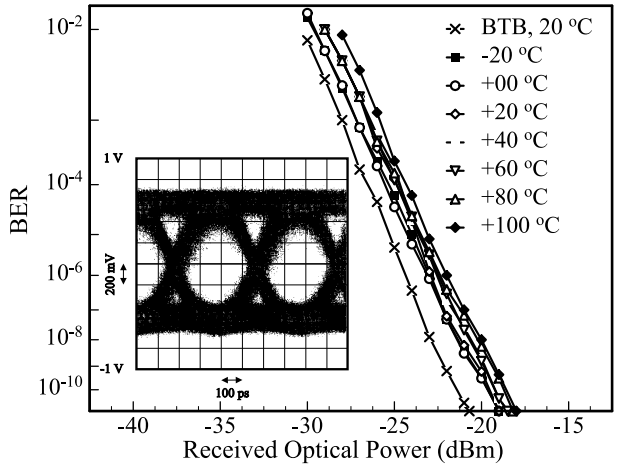

Fig. 3. Eye diagram at $100°$C for a BER of 10^{-11} and temperature dependent bit-error rate characteristics at 2.5 Gbit/s and $2^{31}-1$ word length for 250 m MMF transmission.

The inset of Fig. 3 displays the eye pattern recorded for 2.5 Gbit/s PRBS with $2^{31}-1$ wordlength at $100°$C. For all temperatures, the eye pattern is wide-open, symmetric, and shows no remarkable relaxation oscillations. The results of the transmission experiments for back-to-back testing (BTB) and 250 m MMF transmission are summarized in Fig. 3 where different symbols denote the various temperatures: filled squares $-20°$C, circles $0°$C, diamonds $20°$C, open squares $40°$C, down-triangles $60°$C, up-triangles $80°$C,and filled diamonds $100°$C. At all temperatures the BER for 2.5 Gbit/s data transmission over 250 m MMF remains better than 10^{-11}. At $20°$C a received optical power of -19.0 dBm for 250 m MMF data transmission and -20.5 dBm for BTB is necessary to achieve a BER of 10^{-11}. The maximum power penalty, compared to BTB, observed for transmission at $100°$C is 3 dB. The $100°$C-transmission shows the highest on-off ratio of 6.3 dB while the lowest on-off ratio of 5.6 dB is observed for -20$°$C transmission.

3. Conclusion

We have successfully demonstrated 2.5 Gbit/s PRBS data transmission over 250 m of MMF for temperatures from $-20°$C to $100°$C using a high-performance single-mode VCSEL source operated at fixed 2.5 mA bias current and fixed modulation voltage. Data transmission characteristics are nearly independent of temperature. BER remains better than 10^{-11} for all temperatures. The experiments clearly demonstrate that VCSELs can easily fulfill extended temperature requirements of advanced high-speed optical interconnect systems.

References

[1] D.G. Deppe, D.L. Huffaker, T. Oh, H. Deng, Q. Deng, "Low-threshold vertical-cavity surface-emitting lasers based on oxide-confined and high contrast distributed Bragg Reflectors", *IEEE J. Sel. Topics Quantum Electron.,* vol. 3, pp. 893–904, 1997.

[2] R. Jäger, M. Grabherr, C. Jung, R. Michalzik, G. Reiner, B. Weigl, and K.J. Ebeling, "57 % wallplug efficiency oxide-confined 850 nm wavelength VCSELs", *Electron. Lett.,* vol. 33, pp. 330–331, 1997.

[3] C. Jung, M. Grabherr, R. Jäger, P. Schnitzer, D. Wiedenmann, R. Michalzik, U. Martin, S. Müller, and K.J. Ebeling, "4.8 mW single-mode oxide confined top-surface emitting vertical-cavity laser diode", *Electron. Lett.,* vol. 33, pp. 1790–1791, 1997.

[4] K.L. Lear, V.M. Hietala, H.Q. Hou, M. Ochiai, J.J. Banas, B.E. Hammons, J.C. Zolper, and S.P. Kilcoyne, "Small and large signal modulation of 850 nm oxide-confined vertical cavity surface emitting lasers", *OSA Trends in Optics and Photonics,* vol. 15, pp. 69–74, 1997.

[5] F. Mederer, C. Jung, R. Jäger, M. Kicherer, R. Michalzik, P. Schnitzer, D. Wiedenmann, and K.J. Ebeling, "12.5 Gbit/s data rate fiber transmission using single-mode selectively oxidized GaAS VCSEL at λ = 850 nm", *in Proc. LEOS Annual Meeting 1999,* vol.2, pp.697-698, San Francisco, USA, 1999.

[6] M. Kajita, H. Kosaka, M. Yamada, Y. Sugimoto, K. Kurata, and T. Tanabe, "1 Gb/s modulation characteristics of a vertical-cavity surface-emitting laser array module", *IEEE Photon. Technol. Lett.,* vol. 9, pp. 146–148, 1997.

[7] B. Tell, F. Brown-Goebeler, R.E. Leibenguth, F.M. Baez, and Y.H. Lee, "Temperature dependence of GaAs-AlGaAs vertical cavity surface emitting lasers", *Appl. Phys. Lett.,* col. 60, pp. 683–685, 1992.

VCSEL Arrays for Fiber Optical Interconnects

Roger King and Rainer Michalzik

In this paper, we report on transmitter technologies for Gb/s speed datacom systems. Primarily to enable direct flip-chip integration with silicon CMOS circuits for highly parallel interchip interconnects, we have fabricated two-dimensional vertical-cavity surface-emitting laser (VCSEL) arrays featuring 4×8 elements on a 250 μm pitch. Arrays emitting in the 980 nm spectral region exhibit excellent homogeneity and operation data like 0.8 mA threshold current, below 1.5 V threshold voltage, 1 mW output power at 2 mA current, and more than 35 % conversion efficiency in the 2 to 5 mW power range. Bottom emission of 850 nm arrays is enabled by etching holes into the opaque GaAs substrate. Due to less efficient heat removal, devices are currently limited to about 2 mW light output at 6 mA current.

1. Introduction

Similarly as in telecommunications, the demand for higher bit rates is also prevalent in the optical local area network (LAN) arena. Within the latest deployed technology generation, the Gigabit Ethernet (GbE) solution is on its way to find widespread use in local area backbone networks. Among the different physical realizations, GbE transceivers based on short-wavelength 850 nm VCSELs combined with graded-index multimode fibers (MMFs) are especially cost-effective and can be almost considered as commodity products. Since past trends indicate that current backbone speeds will move to the desktop level with a few years delay, intensive work on 10 Gb/s LAN systems has been initiated.

The present paper focuses on some of our latest progress in the fabrication of two-dimensional VCSEL arrays. The devices themselves have been mainly developed within the framework of a joint project funded by the European Commission, aiming to provide solutions for the direct optical interconnection between electronic integrated circuits [1]. Whereas clock frequencies of the latest available data processors have already reached the 1 GHz range, the layout of the VCSELs even allows for modulation speeds in excess of 10 GHz.

2. Two-Dimensional VCSEL Arrays

Apart from single-transmitter modules as for GbE or fiber ribbon based one-dimensional links [2], the much esteemed VCSEL capabilities are most obviously exploited in two-dimensional arrayed systems, which can offer massively parallel data transmission and might thus help to avoid the electrical interconnect bottleneck to be expected in future high performance computer

environments [3]. For this application space, we have fabricated two-dimensional VCSEL arrays, which allow direct flip-chip hybridization onto electronic circuits. Device and array design and processing as well as static and dynamic characteristics of 980 nm wavelength arrays have been described in [4] in some detail. Prototype arrays are delivered to partners in the joint European OIIC (Optically Interconnected Integrated Circuits) project [1] and are integrated into system-level interconnect demonstrators. Continuous improvements in the design and fabrication routine have led to present devices characteristics shown in Fig. 1.

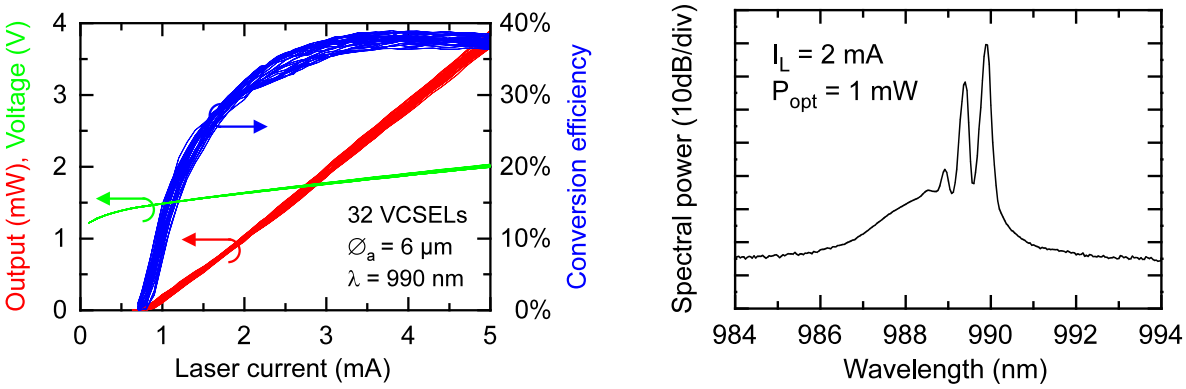

Fig. 1. Laser characteristics of a 990 nm wavelength, 4×8 elements bottom-emitting VCSEL array (left) and optical spectrum of a single device at 2 mA driving current, corresponding to 1 mW optical output power (right).

The left hand side summarizes optical output power, driving voltage, and power conversion efficiency for all 32 elements of a 4×8 VCSEL array, where an individual active diameter of 6 μm has been adjusted through selective oxidation of a single AlAs current aperture layer. Devices are arranged with 250 μm pitch and each unit cell of the array contains individual bondable p- and n-contacts. The molecular beam epitaxially grown arrays show excellent homogeneity and feature average threshold currents and voltages of 0.8 mA and 1.45 V, respectively, and provide 1 mW optical output power at 2 mA driving current. A peak power conversion efficiency of 37 % is achieved for output powers of about 3 mW. By direct microwave probing, previous generation array elements have already been employed for 12.5 Gb/s data transmission over 100 m multimode fiber or 1.6 km standard singlemode fiber [4]. For the present application, where optical interconnection between laser and detector arrays is accomplished through large area POF bundles placed on top of the chips without additional optics, transverse multimode VCSEL operation, as seen in theoptical spectrum in the right hand side of Fig. 1, is perfectly acceptable. If required, transverse singlemode operation can be achieved with smaller active diameter arrays. Devices with about 3 μm diameter delivering up to 3 mW fundamental mode output power at 30 dB sidemode suppression ratio have been demonstrated before [4].

Mainly for reasons of compatibility with the 770 to 860 nm wavelength range, defined in GbE as a standard on the below-1 æm side of the optical spectrum [5], there is also interest to provide integrable short-wavelength VCSEL arrays. Unfortunately, since the GaAs substrate is now highly absorptive, hybrid integration with the driving circuits demands for additional processing steps. As one of the alternatives, bottom-emitting arrays have recently been realized by

means of wafer bonding to a transparent substrate [6], [7], so that devices can be conveniently handled like their 980 nm counterparts. As an intermediate solution, we have fabricated bottom-emitting VCSEL arrays by partially removing the GaAs substrate for light output coupling, as schematically shown in Fig. 2.

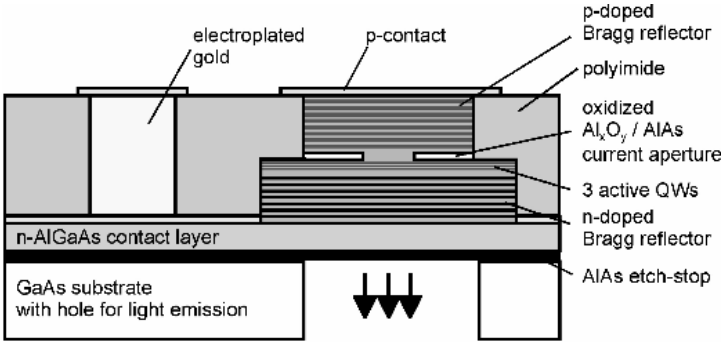

Fig. 2. Schematics of a 850 nm wavelength bottom-emitting VCSEL array element suitable for flip-chip bonding.

The device layout is equivalent to that of the 980 nm arrays [4], except for an additional transparent n-AlGaAs contact layer and a AlAs etch-stop layer. After mechanically polishing down the substrate to about 120 μm thickness, chemically assisted ion beam etching with argon and chlorine gas is employed to define about 80 μm diameter holes centered to the active laser area. Roughly the last 10 μm of the substrate are removed with a citric acid based etchant, before the AlAs etch-stop layer is selectively etched with hydrofluoric acid in the exposed area.

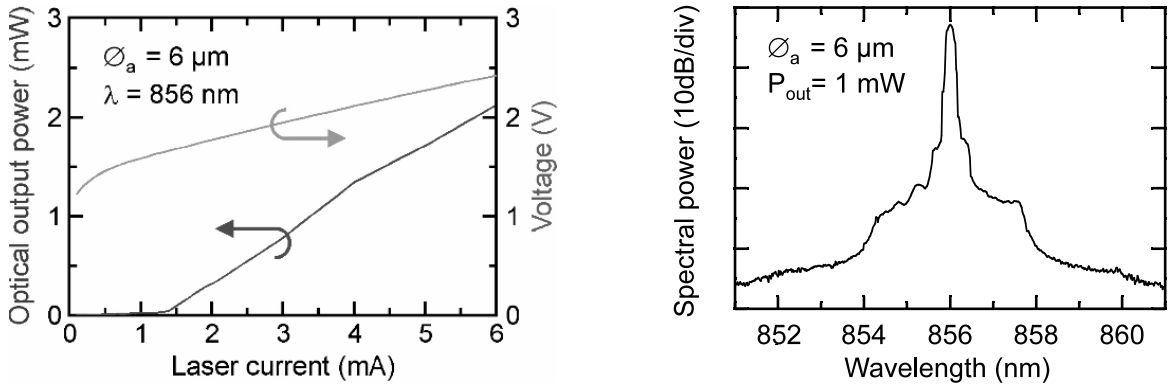

Fig. 3. Operation characteristics (left) and emission spectrum (right) of a 856 nm wavelength bottom-emitting VCSEL.

For testing, arrays were fixed to a copper plate with a recess for light emission. Unfortunately, in conjunction with insufficient heat removal from the array holder, the increase of thermal resistance induced by the etched hole underneath the device prevented the VCSELs from lasing in continuous wave (cw) mode at room temperature. The critical role of heat removal is evidenced

by the fact that cw lasing is possible with just a drop of water being put on the substrate surface. Fig. 3 shows the light-current-voltage characteristics as well as the optical spectrum of a 6 μm active diameter device under this operation condition. Threshold current and voltage are around 1.4 mA and 1.7 V, respectively, and about 2 mW optical output power is emitted at 6 mA driving current. Even at 1 mW output power, lasing at 856 nm wavelength is observed predominantly in the fundamental mode before higher order modes emerge. Considerable improvements in lasing behavior are expected from a revised VCSEL design with an intracavity contact and a smaller outcoupling window. Likewise, the final flip-chip bonding process should assist in heat removal from the emitter array.

3. Conclusion

In this paper, we have first presented operation characteristics of two-dimensional integrable 4×8 elements VCSEL arrays for use in highly parallel short-distance optical interconnects. Whereas 980 nm wavelength arrays are routinely fabricated at high quality and are currently employed in interchip interconnect prototypes, 850 nm bottom-emitting arrays still require more careful consideration of heat spreading properties.

References

[1] "See URL http://www.intec.rug.ac.be/oiic."

[2] H. Karstensen et al., *Proc. 48th Electron. Comp. & Technol. Conf., ECTC*, pp. 747-754. Seattle, WA, USA, May 1998.

[3] *The Semiconductor Industry Association's (SIA's) National Technology Roadmap for Semiconductors*, 1994 and 1997 editions and 1998 Update, "see URL http://www.itrs.net/ntrs/publntrs.nsf."

[4] R. King et al., *Optoelectronic Interconnects VI, J.P. Bristow, S. Tang (Eds.), Proc. SPIE 3632*, pp. 363- 372, 1999.

[5] *IEEE 802.3z Gigabit Ethernet standard, 1000BASE-SX physical layer*

[6] K.D. Choquette et al., *Electron. Lett.*, **34**, pp. 1404-1405, 1998.

[7] C.-K. Lin et al., *IEEE Photon. Technol. Lett.*, **11**, pp. 1542-1544, 1999.

2.5 Gbit/s Data Transmission over 10 km Standard Single-Mode Fiber Using InGaAs VCSELs at 1.13 μm Emission Wavelength

Jürgen Joos and Irene Ecker

Vertical-cavity surface-emitting lasers with an InGaAs quantum well, operating at 1129 nm have been fabricated. Due to lateral single-mode behavior and narrow far-field angles the devices are versatile sources for optical fiber links. Bit error rates (BER) of less than 10^{-11} are demonstrated for 2.5 Gbit/s data transmission over 10 km standard single-mode fiber.

1. Introduction

Vertical-cavity surface-emitting lasers (VCSELs) with emission wavelengths beyond 1 μm are extremely attractive sources for long-distance optical communication. Even though there has been much effort in developing long-wavelength VCSELs there is much more success in fabricating high-performance near-infrared (850 nm and 980 nm) devices [1]. Nevertheless, there have been remarkable results in data transmission experiments using double-fused VCSELs [2, 3]. However, due to complicated processing this conception has lost importance with respect to new technologies of GaAs-based long-wavelength VCSELs. Recently there has been great success in fabricating devices with active materials including Sb [4], InAs quantum dots [5], and GaInNAs [6]. We present single-mode vertical-cavity lasers with a highly strained InGaAs quantum well emititing at 1129 nm wavelength, and demonstrate 2.5 Gbit/s data transmission over 10 km optical fiber.

2. Device fabrication

The VCSEL devices are grown by solid source molecular beam epitaxy. The active zone consists of a single 7 nm thick $In_{0.33}Ga_{0.67}As$ quantum well embedded between GaAs cladding layers. The quantum well thickness and composition is kept slightly below the critical thickness, calculated according to the Matthew-Blakeslee formula. The p-type and n-type AlGaAs-GaAs Bragg reflectors are doped using carbon and silicon, respectively. After epitaxial growth and wet chemical mesa etching, the current aperture with an active diameter of about 6 μm is defined. This is carried out by selective oxidation of an AlAs layer in a hot water vapor environment. Further fabrication steps are Ti-Pt-Au top metal contact evaporation, passivation layer deposition, Ge-Ni-Au bottom metal contact evaporation, bond pad deposition, and wire bonding. The device structure is shown in Fig. 1.

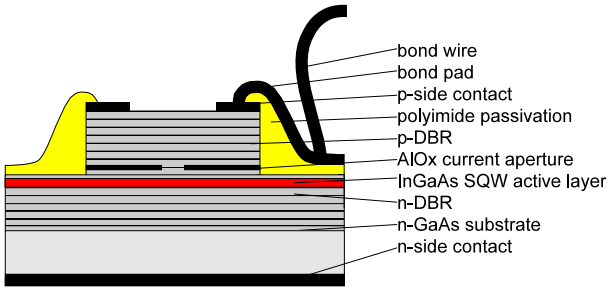

Fig. 1. Structure of a single InGaAs quantum well VCSEL

3. Device properties

In Fig. 2 and 3 the CW room temperature characteristics and the optical spectrum are depicted, respectively.

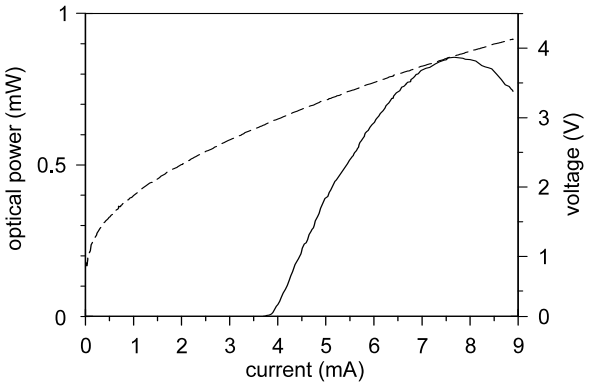

Fig. 2. Characteristics of 6 μm diameter long-wavelength InGaAs VCSEL

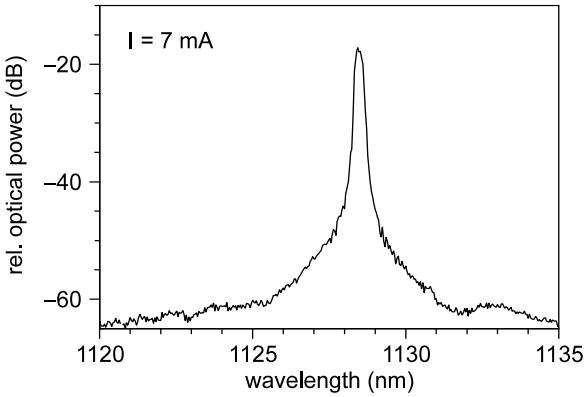

Fig. 3. CW emission spectrum of 6 μm diameter long-wavelength InGaAs VCSEL

The threshold current of the devices is 3.9 mA. While I-P-measurements were carried out using a large area photo detector, the spectrum was measured after butt-coupling into a 50 μm diameter fiber and exhibits transversal fundamental-mode emission at 1129 nm. Even beyond thermal rollover at about two times threshold current there is no visible side-mode. The peak width is limited by the resolution of the spectrum analyzer of 0.1 nm. Throughout the measurements the devices were not thermally mounted but simply attached to a copper carrier.

Fig. 4 shows the measured far field characteristics of the VCSEL and for comparison the far field of the standard single mode fiber used for data transmission experiments. Both of the far field measurements were carried out by recording the angular distribution of the optical power at a distance of 30 cm to the device. According to

$$2\Theta_{1/e} = \frac{2\lambda}{\pi w_0} \tag{1}$$

describing the relation between the $1/e^2$-width of the far field angle $\Theta_{1/e}$, the beam waist radius w_0, and the wavelength λ for Gaussian beams, the beam waist diameter was calculated to be 6.1 μm and therefore coincides very well with the active device diameter.

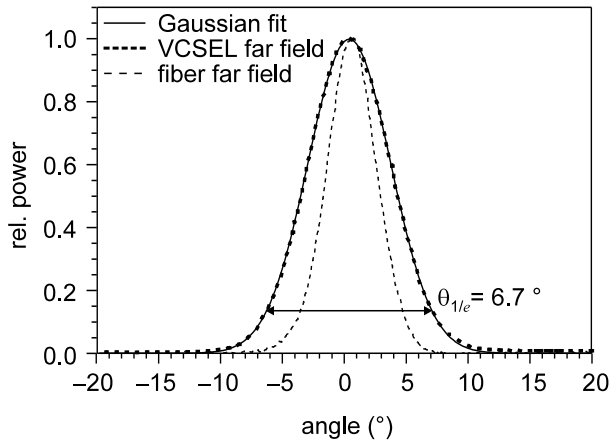

Fig. 4. Far field of 6 μm single-mode VCSEL and standard single-mode fiber.

Using the data from Fig. 4, the beam diameter of the fiber was calculated to be 10.2 μm. The output beam of the VCSEL reaches this value at a distance of 34 μm. This moderate beam widening allows coupling from the VCSEL into a standard single-mode fiber with measured efficiencies of greater than 90 %.

4. Dynamic properties

Fig. 5 shows RIN spectra measured at various bias currents. The RIN measurements were carried out by placing a $16\times16\,\mu\text{m}^2$ InGaAs photo diode directly in front of the laser device. Increasing current leads to decreasing noise not too far above the shot noise limit, which is located at -151 dB/Hz for a photo current of 375 μA, corresponding to 6.2 mA laser driving current. However, by further optimizing the threshold current density, a still lower noise, even below shot noise [7], could be expected. In order to describe the dynamic characteristics of the devices, the modulation efficiency has been examinated. The results are depicted in Fig. 6. From the slope of the fitting curve a modulation efficiency factor of $M_{\text{eff}} = 1.34\,\text{GHz/mA}^{1/2}$ has been extracted. After all emission wavelength has to be weighed against noise and RF characteristics of the devices.

Another measure of dynamic behavior, the so-called K-factor [8], is related to the intrinsic maximum 3 dB corner frequency by

$$\nu_{\max} = \sqrt{2}\frac{2\pi}{K}\,. \tag{2}$$

It is derived from its proportionality to the squared resonance frequency. According to Fig. 7 a K-factor of 2.51 ns was found, which corresponds to a corner frequency of $\nu_{\max} = 3.54\,\text{GHz}$.

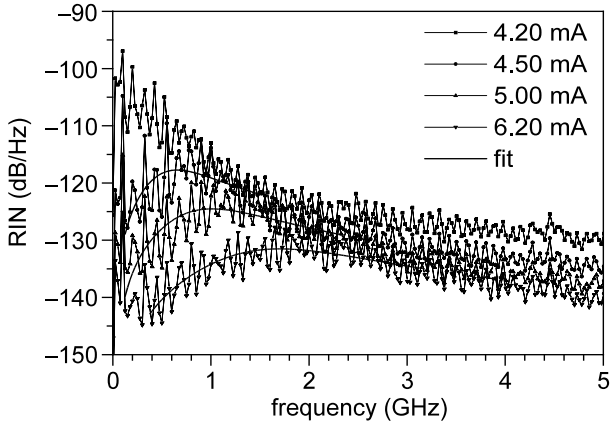

Fig. 5. VCSEL relative intensity noise for various bias currents.

The single quantum well as active layer is expected to be the reason for these moderate values. A large carrier density in the quantum well is required in order to provide sufficient gain, which in its turn leads to reduced differential gain $\partial g/\partial n$. However, by using two or more quantum wells the overall strain in the active region increases and the critical thickness could be exceeded.

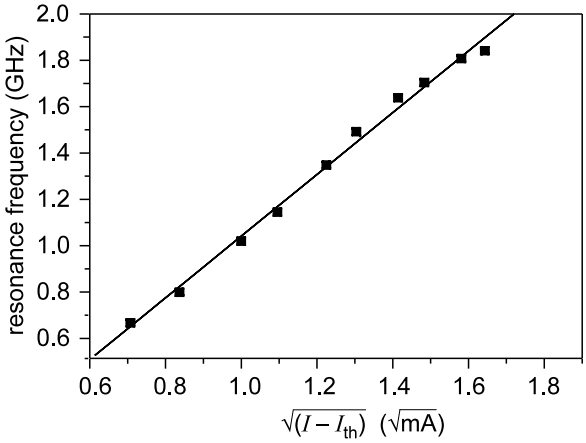

Fig. 6. Modulation efficiency.

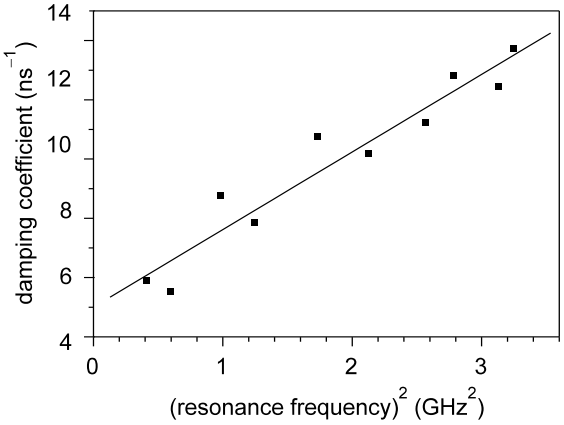

Fig. 7. Relation between damping coefficient and resonance frequency squared. The slope defines the K-factor.

5. Data transmission

Based on the preceding results, data transmission experiments were carried out. The device is driven at a bias current of 6 mA. A 2.5 Gbit/s pseudo-random bit sequence (PRBS) with $V_{pp} = 0.4$ V is added by means of a bias-tee. The reason for choosing this high bias current and hence the low modulation ectinction ratio is the increasing noise at lower currents, which

was approved by varying both of the values for optimum transmission results. The used word length of $2^7 - 1$ is standard for data encoding in LANs as e.g., Gigabit Ethernet using 8B/10B encoding. The optical signal passes a variable attenuator in order to adjust the optical power. It is detected by a 2 GHz bandwidth Ge pin-photo diode. The signal is monitored with an electrical sampling oscilloscope and analyzed with a BER decoder. The data transmission results are shown in Fig. 8 where open circles refer to back-to-back testing and plain diamonds denote transmission over 10 km standard single mode fiber. The comparatively low power penalty for 10 km transmission of 1 dB proofs the almost negligible amount of fiber dispersion. Thus, the limiting factor for going to distances larger than 10 km is absorption rather than dispersion. The eye diagram which was recorded at a bit-error rate of 10^{-11} is symmetric and wide open.

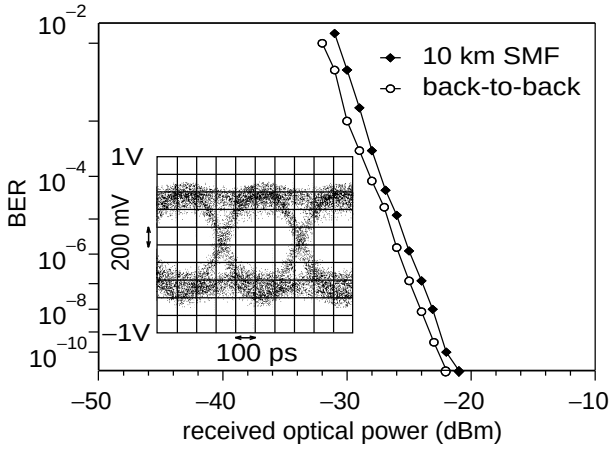

Fig. 8. Bit error rate (BER) characteristics for 2.5 Gbit/s data transmission over 10 km of standard single-mode fiber (SMF) and back-to-back testing. The inset eye diagram was recorded at BER $= 10^{-11}$.

6. Conclusion

We have demonstrated high-performance single-mode VCSELs with a single $In_{0.33}Ga_{0.67}As$ quantum well emitting at 1129 nm wavelength. The devices exhibit a far field angle of $\theta_{1/e} = 6.7\,^\circ$, an intrinsic corner frequency of 3.54 GHz, and a K-factor of 2.51 ns. Error-free data transmission was achieved with 2.5 Gbit/s PRBS over 10 km standard single-mode fiber.

Acknowledgments

This work is supported by the Volkswagen Stiftung which is gratefully acknowledged.

References

[1] D. Wiedenmann, R. King, C. Jung, R. Jäger, R. Michalzik, P. Schnitzer, M. Kicherer, and K.J. Ebeling "Design and analysis of single-mode oxidized VCSEL's for high-speed optical interconnects ", *IEEE J. Sel. Topics Quantum Electron.,* vol 5, pp 503-511, 1999

[2] S.Z. Zhang, N.M. Margalit, T.H. Reynolds, J.E. Bowers, "1.54-μm vertical-cavity surface-emitting laser transmission at 2.5 Gb/s", *IEEE Photon. Technol. Lett.,* vol. 9, pp. 374-376, 1997.

[3] V. Jayaraman, J.C. Geske, M.H. MacDougal, F.H. Peters, T.D. Lowes, and T.T. Char, "Uniform threshold current, continuous-wave, singlemode 1300nm vertical cavity lasers from 0 to 70 °C", *Electron. Lett.,* vol. 34, pp. 1405-1407, 1998

[4] T. Anan, M. Yamada, K. Tokutome, S. Sugou, K. Nishi, and A. Kamei, "Room-temperature pulsed operation of GaAsSb/GaAs vertical-cavity surface-emitting lasers", *Electron. Lett.,* vol. 35, pp. 903-904, 1999

[5] D.L. Huffaker, G. Park, Z. Zhou, O.B. Shchekin, D.G. Deppe, "1.3 μm room-temperature GaAs-based quantum-dot laser", *Appl. Phys. Lett.,* vol. 73, pp. 2564-2566, 1998

[6] K. Nakahara, M. Kondow, T. Kitatani, M.C. Larson, K. Uomi, "1.3-μm continuous-wave lasing operation in GaInNAs quantum-well lasers", *IEEE Photon. Technol. Lett.,* vol. 10, pp. 487-488, 1998

[7] D. Wiedenmann, P. Schnitzer, C. Jung, M. Grabherr, R. Jäger, R. Michalzik, K.J. Ebeling, "Noise characteristics of 850 nm single-mode vertical cavity surface emitting lasers", *Appl. Phys. Lett.,* vol. 73, pp. 717-719, 1998.

[8] R. Michalzik, R. King, D. Wiedenmann, P. Schnitzer, K.J. Ebeling, "Modeling and application of VCSELs for optical interconects", *Proc. Optoelectronics '99, Physics and simulation of optoelectronic devices VII,* vol. 3625, San Jose, California, USA, Jan., 1999.

CW Room Temperature Operation of a Diode Cascade VCSEL

Thomas Knödl

We have fabricated the first room temperature, continuous-wave operating diode cascade InGaAs-AlGaAs quantum well vertical cavity surface emitting laser with two active pn-junctions coupled by an Esaki junction at 988 nm wavelength.

1. Introduction

Vertical cavity surface emitting lasers (VCSELs) are considered as excellent candidates for optical interconnect applications due to low threshold currents, high wallplug efficiency and high-speed modulation capabilities [1]. On the other hand, common VCSEL devices are characterized by the extremely low roundtrip gain in the cavity that requires high mirror reflectivity. Therefore, thermal rollover limits high-power applications of VCSEL structures due to internal heating. To overcome this distinct disadvantage, diode cascade VCSEL structures are proposed to reduce threshold current and heighten output power by increasing the roundtrip gain [2]. Moreover, such a VCSEL could exhibit high differential quantum efficiencies well exceeding unity. Thus, cascade structures may also be interesting for low-noise applications due to an expected improvement in the noise figure. However, the devices can only be demonstrated up to 175 K in continuous-wave (CW) operation [3]. Here, we present results of the first CW, room temperature operating diode cascade VCSEL at 988 nm wavelength as previously reported [4].

2. Device Structure and Fabrication

The basic mechanism in cascade laser structures is carrier recycling that, in this work, is achieved by exploiting the idea of interband carrier tunneling between active regions as indicated in Fig. 1. Considering an electron injected in the conduction band on the right hand side of Fig. 1 making an optical transition towards the top of the valence band in the quantum well, is then recycled into a conduction band electron by the Esaki junction and starts the same process again. Thus, electrons are cascading down a potential staircase, emitting a photon at each step.

Fig. 2 shows a schematic diagram of the device structure that is grown by molecular beam epitaxy. The diode cascade VCSEL contains two active pn-junctions in series, each of which comprises three undoped 8 nm thick $In_{0.2}Ga_{0.8}As$ quantum wells separated by 10 nm thick

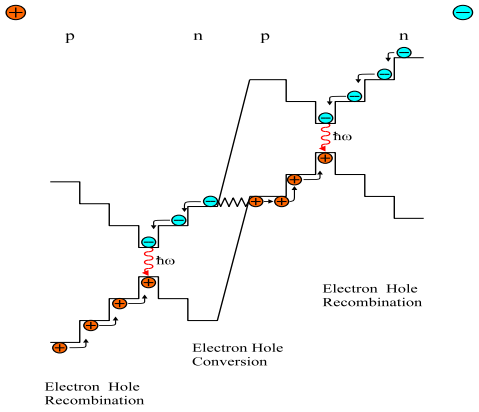

Fig. 1. Schematic energy band diagram of the epitaxially stacked VCSEL under forward bias.

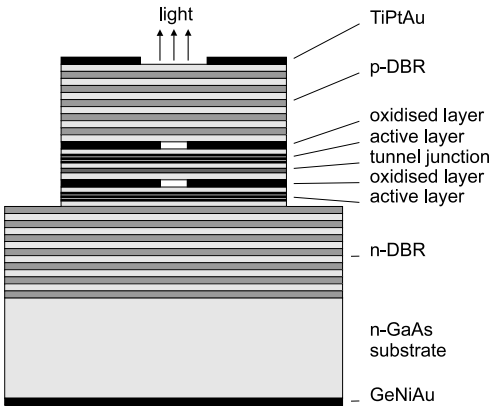

Fig. 2. Device schematic of a diode cascade VCSEL structure.

GaAs barriers. The active regions are coupled by a highly doped GaAs(p^+)-$In_{0.1}Ga_{0.9}As$(n^+)-GaAs(n^+) Esaki junction of 40 nm thickness to realize a low resistance quasi-Ohmic intercontact. For the p- and n-type doping we use C and Si, respectively. The reverse biased Esaki junction is placed in a node of the standing wave pattern to reduce free-carrier absorption. Current confinement is achieved by mesa etching and subsequent selective oxidation of two 30 nm AlAs layers incorporated above each active region. The second AlAs oxidation layer above the bottom-most laser junction is implemented to reduce current spreading. A ring contact deposited on the mesa allows for top surface emission.

3. Esaki Junction

The performance of diode cascade VCSELs essentially depend on the implementation of low resistance tunnel junctions to minimize additional device heating. However, the realization of low resistance Esaki junctions is dominated by the n-type doping compensation effect in GaAs. With increasing n-dopant species concentration, eventually the dopant begins to substitute on the acceptor sites limiting the maximum donor incorporation. Fig. 3 shows the n-type doping dependence of the zero-bias specific resistance on various GaAs Esaki junctions at a fixed p-type doping level of p$\approx 1\times10^{20}$ cm^{-3}. The resistance of the tunnel devices are determined by a four-terminal measurement, including the contact resistivity. The minimum specific resistance of 3.3×10^{-4} Ωcm^2 is obtained for n$\approx 2.6\times10^{19}$ cm^{-3}. Further improvement of the zero-bias specific resistance up to 1.3×10^{-4} Ωcm^2 is demonstrated by introducing an $In_{0.1}Ga_{0.9}As$ layer in the barrier region to reduce the energy gap and increasing the tunneling current. The current-voltage characteristic of a GaAs(p^+)-GaAs(n^+) tunnel diode in comparison with that of a GaAs(p^+)-$In_{0.1}Ga_{0.9}As$(n^+)-GaAs(n^+) is shown in Fig. 4. The device diameter is 150 μm with a p- and n-type doping level of 1×10^{20} cm^{-3} and 2.5×10^{19} cm^{-3}, respectively.

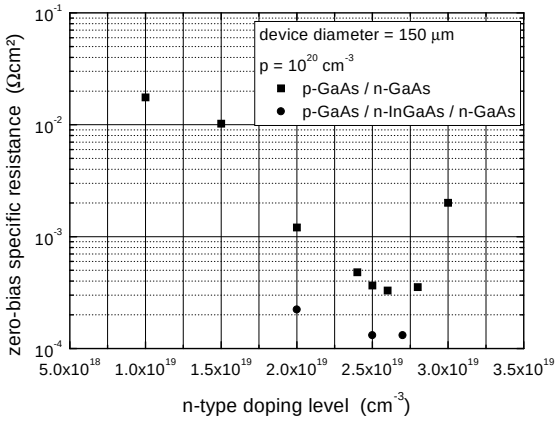

Fig. 3. Zero-bias specific resitance of various Esaki junctions with respect to the n-type doping level.

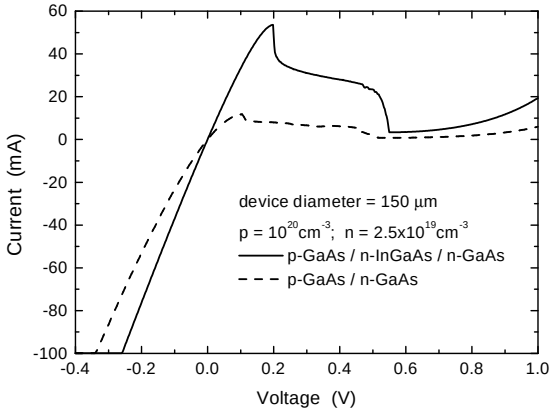

Fig. 4. I-V characteristic of a GaAs- and GaAs/InGaAs Esaki junction.

4. Diode Cascade VCSEL

Fig. 5 shows the CW, room temperature output and voltage characteristic for a fabricated diode cascade VCSEL with 10 μm oxide apertures. At threshold, the emission wavelength is located at 988 nm with a current of 2.5 mA as shown in Fig. 5. The threshold voltage of 3.3 V is about

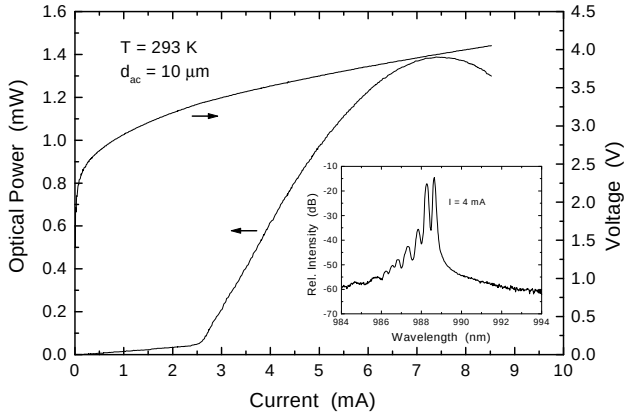

Fig. 5. CW optical output power and voltage versus laser current at room temperature of a diode cascade VCSEL. The measured active diameter is about 10 μm. The insert shows the optical spectrum at a driving current of 4 mA.

0.8 V higher than twice the bandgap voltage and the differential resistance is 113 Ω, indicating a successful implementation of a low resistance Esaki junction. Maximum output power of about 1.39 mW is given at a driving current of 7 mA. The obtained differential quantum efficiency is 33 %.

Low temperature measurements of the diode cascade VCSEL with a differential quantum efficiency exceeding 100 % at 150 K confirm the successful implementation of the cascade concept as shown in Fig. 6. The observed temperature dependence of the threshold current and the differential quantum efficiency is illustrated in Fig. 7. A minimum threshold current of about 2.7 kA/cm^2 is found at 273 K, when the gain peak of the quantum wells is aligned to the cavity resonance. We assume that the decreasing differential quantum efficiency with temperature is related to leakage current and absorption effects in the cavity.

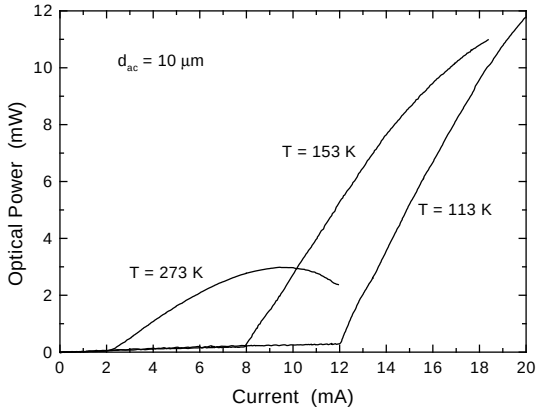

Fig. 6. CW output characteristic at various device temperatures of a diode cascade VCSEL. The active device diameter is about 10 μm.

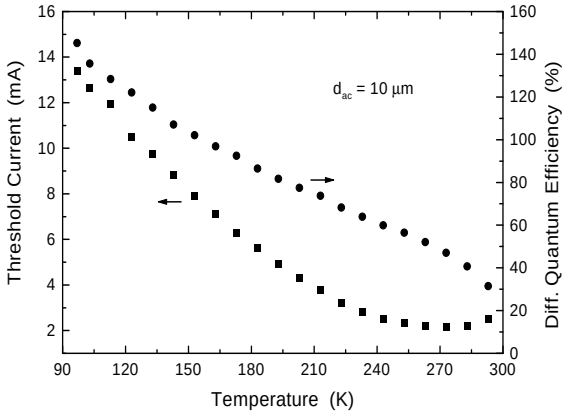

Fig. 7. Threshold current and differential quantum efficiency as a function of the device temperature of a diode cascade VCSEL.

From pulsed measurements (100 ns, duty-cycle 1 %) we observed an increase in the differential quantum efficiency of about 8 %, also indicating that thermal effects due to the Esaki junction play no dominating role in the device.

5. Conclusion

In conclusion we have demonstrated the first CW operating diode cascade VCSEL at room temperature coupled by a low resistance Esaki junction. Further work will include optimising the Esaki junction and the cascade device structure, increasing the number of active regions in the cavity, and the investigation of the modulation properties of diode cascade VCSELs.

References

[1] R. King et al., *Proc. of SPIE on Optoelectronic Interconnects VI*, vol. 3632, pp. 363–372, San Jose, CA, Jan. 1999.

[2] Y. Kotaki et al., *Conf. Solid State Devices and Material*, pp. 607–639, Kobe, Japan, 1984

[3] W. Schmid et al., *Electron. Lett.*, vol. 34, pp. 553–555, 1998.

[4] T. Knödl et al., *Proc. of IEEE LEOS '99*, vol. 2, pp. 143–144, San Francisco, Ca, Nov. 1999.

kW/cm^2 VCSEL Arrays for High Power Applications

Michael Miller and Martin Grabherr

High beam qualities at high optical output powers make VCSELs attractive light sources for various applications like printing, engraving or pumping of solid state lasers. We report on mounted AlGaAs-GaAs two-dimensional VCSEL arrays of 0.123 mm^2 size emitting 1.4 W cw optical output power at 10 °C. The emitting wavelength of these bottom emitting VCSELs is 980 nm. The power density spatially averaged over the cleaved laser chip is as high as 1.1 kW/cm^2. Narrow circular far-fields below 12 ° FWHM allow easy focusing of the light to a spot size of less than 100 μm resulting in a power density of above 10 kW/cm^2. Mounting of the VCSEL array is very convenient since there is no need to take care of precise facet alignment as required for conventional edge emitting laser arrays. Simple mounting on copper heat sinks or microchannel coolers leads to inexpensive laser modules with output powers in the Watt regime. Lifetime testing for more than 7000 hours at room temperature performed at 1 A current corresponding to an output power of about 440 mW has shown a degradation rate of about 1 % per 1000 hours which is very promising for industrial applications.

1. Introduction

With the introduction of a vertical-cavity surface-emitting laser diode the cornerstone of a very promising device was laid. Main advantages of such devices include the free design of the cross-sectional area of the cavity, single longitudinal mode emission due to the very short effective resonator of about 1 μm length, transverse mode control by appropriate choice of the mesa diameter [1]. The enormous potential of single-mode devices is shown in optical data communication with data rates of 12.5 Gbit/s at bit error rates of less than 1×10^{-11} [2]. Another enormous advantage of the vertical outcoupling of the optical beam is the possibility to form two-dimensional arrays being used by many groups for highly parallel optical links [3, 4]. One can easily process neighboring devices with a spacing of 10 μm and the dimensions of an array are then practically given by the area of the wafer. Improvements of the epitaxial material, optimized processing like wet oxidation of the current aperture, improved device design and an established mounting technique for heat removal have led to VCSELs that emit optical powers of some hundreds of Milliwatts or even Watts for VCSEL arrays [5, 6]. Due to favorable beam profile, uncritical alignment tolerances for mounting, resistance against COMD (catastrophic optical mirror damage) and high reliability, VCSELs represent a dedicated light source for various fields of medium to high power applications like printing, engraving, marking, material treatment or even free space data transmission.

2. Array Fabrication

The epitaxial structure of the VCSEL devices is grown by solid source molecular beam epitaxy (MBE) on GaAs substrate and is shown schematically in Fig. 1. The p-type Bragg mirror

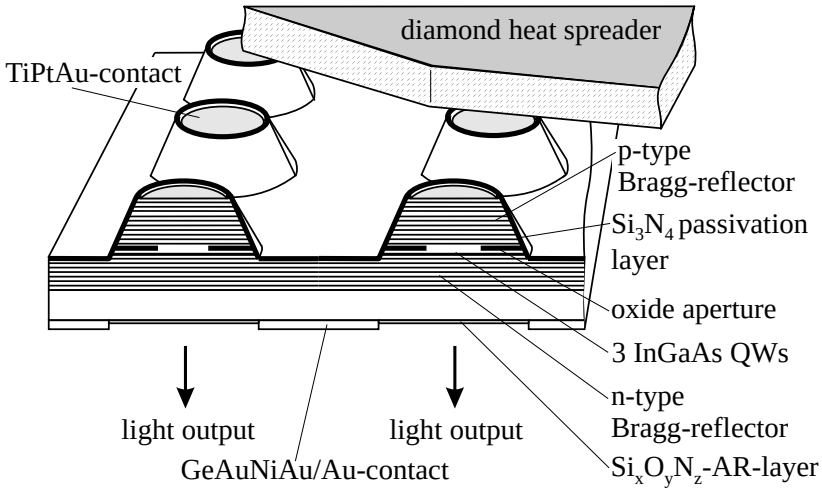

Fig. 1. Schematic drawing of a two-dimensional bottom emitting VCSEL array soldered on diamond heat spreader.

is made up by 30 pairs of λ/4-thick AlGaAs-GaAs layers and is doped with carbon. The n-type Bragg mirror consists of 20.5 pairs of the same material and is doped with silicon. The outcoupling ratio between the upper and lower mirror is about 1:30. To minimize the dissipated power and the absorption in the resonator the doping has to be modulated between individual layers of the Bragg mirrors to reduce differential electrical resistance and light absorption. The mask design of the array consists of 19 elements in a honeycomb-like arrangement to obtain tightest packaging. The diameter of the mesas is 80 μm and the center to center spacing of

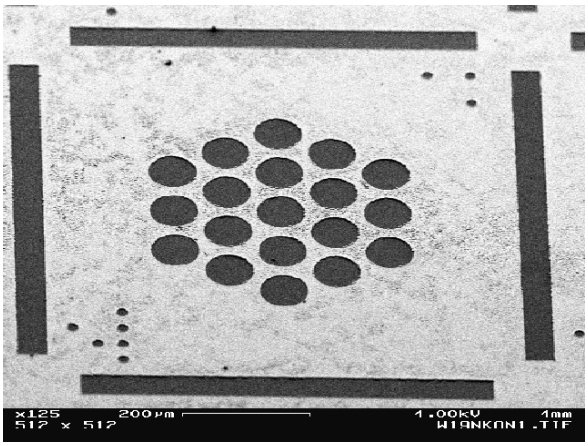

Fig. 2. N-type contact with emission windows and trenches for cleaving.

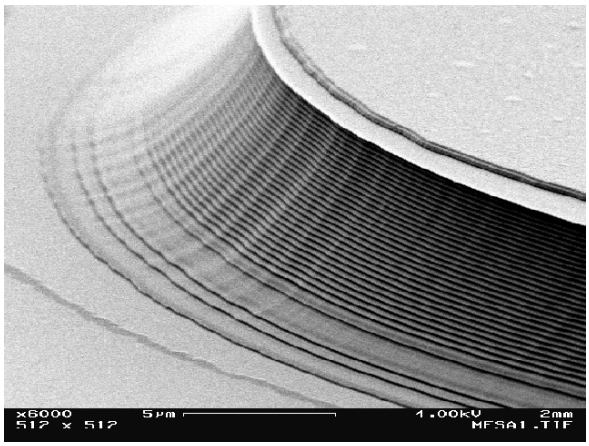

Fig. 3. Wet chemically etched mesa with p-type Bragg stack and active region.

neighboring elements is 100 μm as shown in Fig. 2. The mesas are wet chemically etched down to the active region through the 30 nm thick AlAs layer in the p-doped region of the cladding

layer next to the active layer as can be seen in Fig. 3. To form the current aperture the AlAs is selectively oxidized to a depth of 15 μm resulting in an active diameter of 50 μm for each device in the array. After thinning and polishing the substrate to a thickness of less than 200 μm an anti-reflection (AR) coating consisting of Si_xN_y is deposited on the back side of the substrate using a PECVD system. Subsequently, the emission windows are protected with photoresist and the surrounding area is etched with CAIBE or RIE. On the etched region an n-type GeAuNiAu contact is evaporated and lift-off is used to open the emission windows. On top of the mesas a full p-type TiPtAu contact is evaporated. As the final step a 1 μm thick Au layer is electroplated on the n-type metallization. Fig. 2 shows the emission windows and the trenches for cleaving the array. After processing, the basic characteristics of the devices are recorded on wafer before cleaving.

3. Basic Characteristics

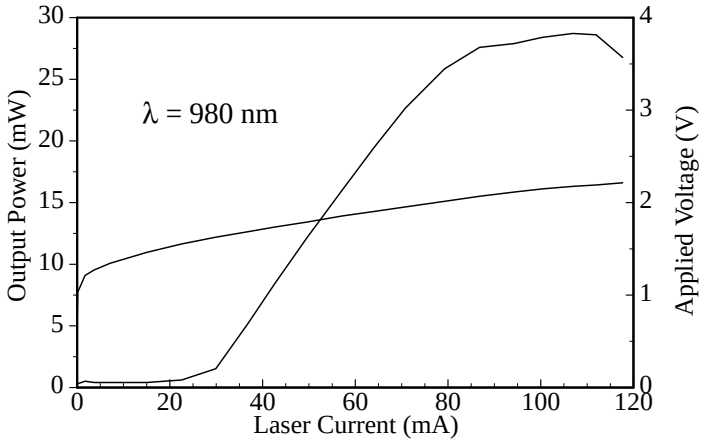

Fig. 4. Typical output characteristics of a single device with an active diameter of 50 μm.

Fig. 4 presents the typical output characteristics for a device with an active diameter of 50 μm. The basic characteristics of this VCSEL are the V-I-behavior to determine kink voltage of 1.4 V, threshold voltage of 1.6 V and differential resistance of 7.5 Ω in the linear region. Also the L-I-behavior in the unmounted state for a single device in the array is very important to get information about the maximum output power which is about 30 mW for this non heat sunk device. The threshold current can be read from the graph to be about 27 mA. The differential quantum efficiency of 43 % is determined from the slope in the linear region of the output power curve. From the known area of the active region the threshold current density of 1.38 kA/cm^2 is obtained. The combination of V-I and L-I-behavior results in the conversion efficiency by dividing the optical output power by the electrical input power which reaches a maximum of about 18 % for unmounted devices. The output characteristics of all 19 single devices of the array have to be extremely homogeneous because after mounting all devices are driven in parallel and current crowding in an element may destroy it. A very important factor for device performance is the thermal resistance since the optical output power strongly depends on the internal heating

resulting in thermal roll-over of the L-I-characteristic. The thermal resistance

$$R_{th} = \frac{\Delta T_{hs}}{\Delta P_{diss}} = \frac{(\Delta\lambda/\Delta P_{diss})}{(\Delta\lambda/\Delta T_{hs})} \tag{1}$$

defined by the ratio of temperature rise ΔT_{hs} due to the dissipated electrical power ΔP_{diss} can be obtained from the redshift $\Delta\lambda$ of the emitted wavelength of an individual mode due to increased dissipated power at constant heat sink temperature and the wavelength shift due to altered heat sink temperature at constant dissipated power. To obtain higher optical output power an improved mounting technique for heat removal is required in particular if several devices are driven in parallel. Due to the outcoupling of the light through the substrate the wavelength

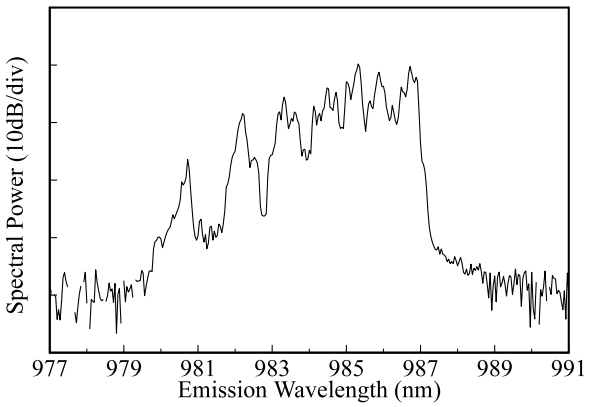

Fig. 5. Emission spectrum of the VCSEL array at a current of 2 A.

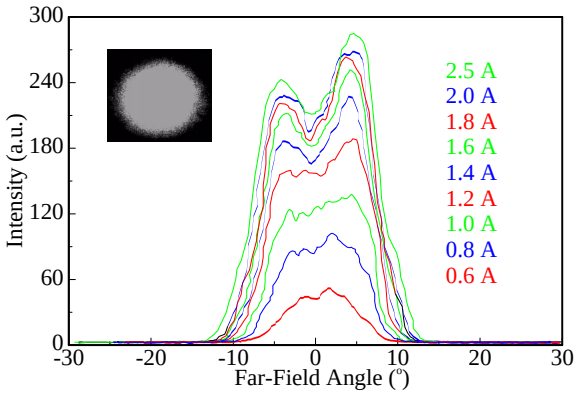

Fig. 6. Far-field pattern and cross sections at different currents.

limited to above 900 nm to avoid fundamental absorption in the substrate. The spectrum of the VCSEL array shown in Fig. 5 is centered at 984 nm. The 10 dB down span of the emitted spectrum is about 5 nm. Two factors are responsible for the spectral broadening namely the strong multi-mode emission behavior of each device in the array and the slight layer thickness variation due to non optimized MBE growth resulting in a wavelength shift of about 3.5 nm across the array of 450 μm width.

The cross sectional far-field angle in Fig. 6 is recorded by a photo diode which is rotated over the semi-circle of the emission direction. The inset shows the circular-symmetric far-field pattern on a focusing screen. For low driving currents the beam shape can be described by a Gaussian profile whereas at higher currents a doughnut-like profile occurs. For all driving currents FWHM of the far-field angle is below 12° which is very favorable for focusing or collimating optics because astigmatism is much weaker as compared to edge emitting lasers.

4. Mounted Arrays

Thermal behavior has a strong influence on the optical output characteristics because thermal rollover limits maximum power. From experimental results we know that the point of thermal

turn-off occurs at an internal temperature of about 200°C [7]. If one can reduce heat generation by lower electrical series resistances or suppress temperature rise by increased thermal conductivity the output power will increase accordingly. The specific thermal conductivity of

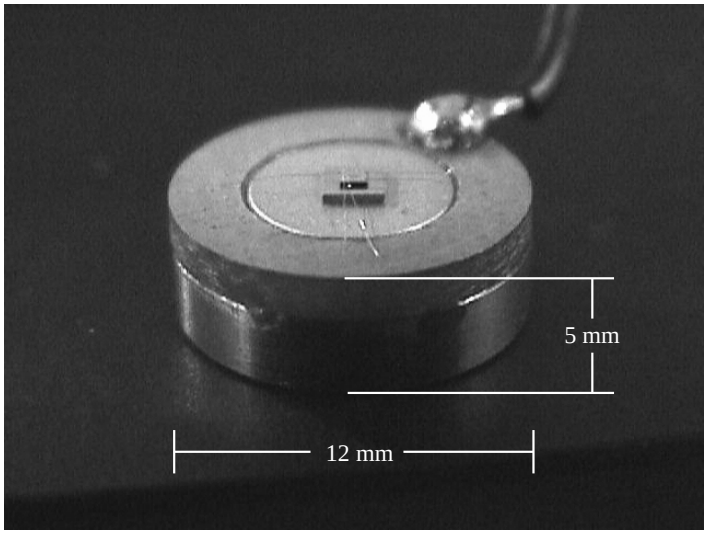

Fig. 7. Mounted VCSEL-array on metallized diamond and copper heat sink.

GaAs is about $\lambda_{GaAs} = 44$ W/K·m. Heat dissipation can be strongly increased by soldering the chip up-side down on a diamond heat spreader ($\lambda_{Dia} \geq 1000$ W/K·m) or a copper heat sink ($\lambda_{Co} \approx 400$ W/K·m). For mounting the array is first cleaved with the dimensions of 800×800 μm^2 and soldered with eutectic $Au_{80}Sn_{20}$ on a metallized diamond of 2×2 mm^2 area as can be seen in Fig. 7. This module is then soldered on a copper heat sink using eutectic $Au_{80}Sn_{20}$. Both solderings are realized in only one heating-up step at a temperature of about 290°C. The copper heat sink has a diameter of 12 mm and a height of 5 mm. The thermal capacitance of this small volume is not big enough to drive the array satisfactory in cw mode. For this reason a thread is drilled in the backside of the copper to mount this heat sink easily on a bigger heat sink with higher thermal capacitance using a screw. The heat sink provides the common p-contact for all devices in the array so that all elements are operated in parallel. After mounting the array is bonded on the galvanic n-contact with bond wires to an insulated

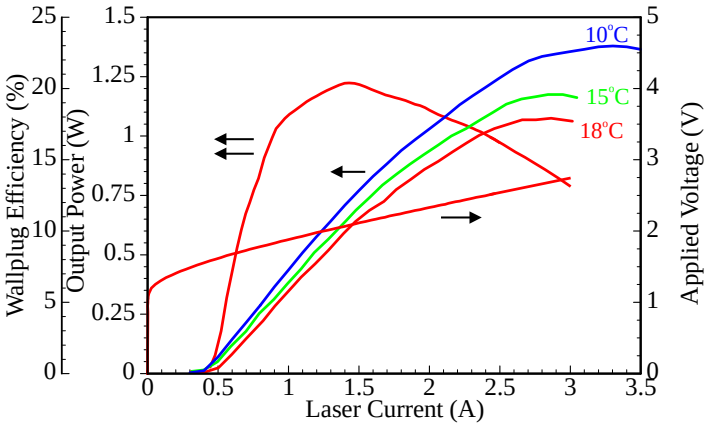

Fig. 8. Output characteristics of a mounted VCSEL-array at different heat sink temperatures.

copper plate for current supply. With an expected driving current of about 3 to 4 A, eight wires with a diameter of 30 μm were bonded to guarantee a low resistance electrical connection. The module can be driven as a passive heat sink or connected to a Peltier element for active cooling. Fig. 8 shows the output characteristics of a mounted VCSEL array consisting of 19 elements with an active diameter of 50 μm for different heat sink temperatures. The threshold current varies from 480 mA at 18°C to 400 mA at 10°C indicating a slight detuning of gain and cavity resonance caused by internal heating due to the dissipated power at threshold. The maximum output power at room temperature of 1.08 Watt increases up to 1.4 Watt at 10°C. If we take a chip size close to the honeycomb-like arrangement of the lasers into account the spatially averaged power density at 1.4 Watt is as high as 1.15 kW/cm^2. By reducing the diameter of the focal spot by a factor of 3 with a lens the power density increases above 10 kW/cm^2 which is promising for many applications. The differential resistance is 0.48 Ω which is slightly larger

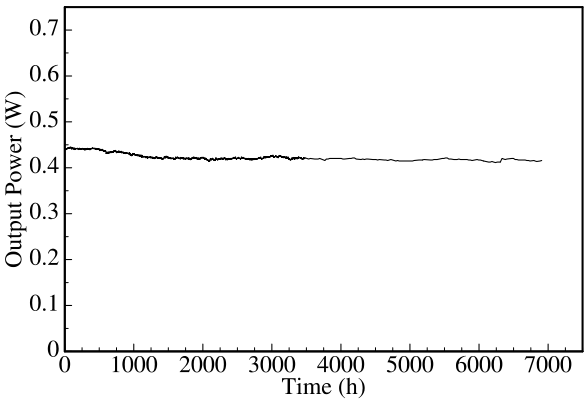

Fig. 9. Lifetime testing of a VCSEL-array at a current of 1 A and a corresponding output power of about 440 mW.

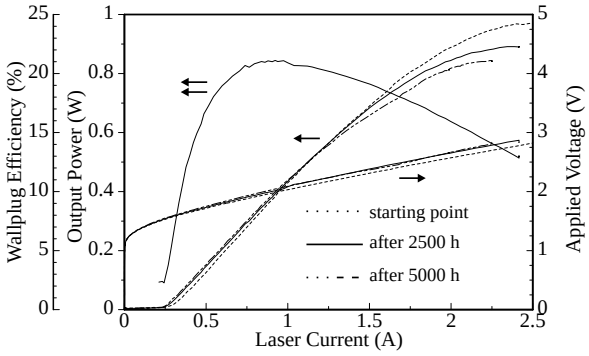

Fig. 10. Output characteristics of the array at the beginning, after 2500 hours and after 5000 hours of duty.

than that of 19 lasers with 7.5 Ω driven in parallel. The discrepancy is due to additional ohmic losses in the bond and solder connections. The maximum conversion efficiency exceeds 20 % for all temperatures at 3 times threshold and the maximum output power is reached at 6 to 7 times threshold. The differential conversion efficiency is larger than 50 % but there is still some place for improvements by optimizing the mirror reflectivities and minimizing the absorption by changing the doping profile. Fig. 9 illustrates lifetime testing of an array driven at a current of 1 A corresponding to an optical output power of 440 mW. The array mounted on a microchannel cooler fabricated by the ILT Fraunhofer Institut at Aachen is operated for more than 7000 hours at room temperature. The total degradation rate is about 7 % corresponding to 1 % per 1000 hours. The slight variation of output power over short periods of time can be explained by fluctuations of the water temperature. The output characteristics at the beginning of the test, at 2500 hours, and at 5000 hours are given in Fig. 10. The minor decrease of the threshold current may be caused by burn-in effects.

5. Conclusion

We have fabricated and characterized high-power VCSEL arrays consisting of 19 single devices with active diameters of 50 μm emitting at a wavelength of 980 nm. Maximum output power is 1.08 Watt for cw operation at room temperature and 1.4 Watt at a heat sink temperature of $10\,^{\circ}$C. Simple focusing to a spot size of about 100 μm diameter yields cw power densities in excess of 10 kW/cm^2. Applications for this power regime are marking of foils, joining or cutting of plastics and pumping of solid state lasers. In the future, we plan to design new heat sinks for larger arrays consisting of about 50 to 100 single devices. With a target optical power of about 10 Watts we have to deal with approximately 100 Watts of dissipated power at a soldered area of about 0.25 to 0.5 mm^2.

References

[1] C. Jung, R. Jäger, M. Grabherr, P. Schnitzer, R. Michalzik, B. Weigl, S. Müller, and K. J. Ebeling, "4.8 mW singlemode oxide confined top-surface emitting vertical-cavity laser diodes," *Electron. Lett.* **33**, pp. 1790–1791, 1997.

[2] F. Mederer, C. Jung, R. Jäger, M. Kicherer, R. Michalzik, P. Schnitzer, D. Wiedenmann, and K. Ebeling, "12.5 Gbit/s data rate fiber transmission using single-mode selectively oxidized GaAs VCSEL at λ = 850 nm," in *LEOS Annual Meeting 1999*, vol. 2, pp. 697–698, (San Francisco, USA), Nov. 1999.

[3] H. Karstensen, L. Melchior, V. Plickert, K. Drögemüller, J. Blanck, T. Wipijewski, H.-D. Wolf, J. Wieland, G. Jeiter, R. Dal'Ara, and M. Blaser, "Parallel optical link (PAROLI) for multichannel gigabit rate interconnects," in *48th Electron. Comp. and Technol. Conf., ECTC'98*, pp. 747–754, (Seattle, WA, USA), May 1998.

[4] D. Wiedenmann, R. King, C. Jung, R. Jäger, R. Michalzik, P. Schnitzer, M. Kicherer, and K. J. Ebeling, "Design and Analysis of Single-Mode Oxidized VCSEL's for High-Speed Optical Interconnects," *IEEE J. Select. Topics Quantum Electron.* **5**, pp. 503–511, 1999.

[5] M. Grabherr, M. Miller, R. Jäger, R. Michalzik, U. Martin, H. Unold, and K. J. Ebeling, "High-Power VCSEL's: Single Devices and Densely Packed 2-D-Arrays," *IEEE J. Select. Topics Quantum Electron.* **5**, pp. 495–502, 1999.

[6] D. Francis, H. Chen, W. Yuen, G. Li, and C. Chang-Hasnain, "Monolithic 2D-VCSEL array with >2W CW output power," in *IEEE Int. Semiconductor Laser Conf. (ISLC)*, pp. 99–100, (Nara, Japan), Oct. 1998.

[7] B. Weigl, M. Grabherr, C. Jung, R. Jäger, G. Reiner, R. Michalzik, D. Sowada, and K. J. Ebeling, "High-Performance Oxide-Confined GaAs VCSEL's," *IEEE J. Select. Topics Quantum Electron.* **3**, pp. 409–415, 1997.

Visible Red Single-Mode Vertical-Cavity Top-Surface-Emitting Lasers with GaAs Quantum Wells

Roland Jäger and Martin Grabherr

We have designed and fabricated vertical-cavity surface-emitting lasers (VCSELs) for 700 nm to 800 nm wavelength emission range using four 6 nm GaAs quantum wells (QWs). A 3 μm active diameter laser exhibits a threshold current of 3.5 mA in continuous-wave (CW) operation at an emission wavelength of 749.5 nm. Using pulsed operation condition with a pulse length of 8 nsec. and a duty cycle of 0.8 % a 2 μm active diameter laser shows a threshold current of 20 mA at an emission wavelength of 710.5 nm.

1. Introduction

Visible red emitting VCSELs are promising devices for use in numerous applications such as plastic optical fibre communications, barcode readers, chemical sensing, laser printing and displays. Most of the reported VCSELs for the 700 nm to 800 nm rage use AlGaAs QWs [1]-[3] or GaAs/AlAs Superlattices [4, 5] providing the gain maximum well matched to the4 resonance wavelength. Due to the high chemically activity of aluminum atoms to the rest gases in the growth chamber the quality of AlAs or AlGaAs is reduced by nonradiative traps. This influences fundamental laser characteristics and especially the aging behaviour. To overcome this problem we have designed and fabricated a VCSEL structure based on four 6 nm GaAs QWs showing the gain maximum at nominally 830 nm. To reach visible wavelengths, the optical cavity of the VCSEL is designed for emission below 800 nm. Due to the high quality of the GaAs QWs, the sampled gain on the short wavelength side of the gain spectrum is comparable to the low optical gain of Aluminum containing QW's.

2. VCSEL design and fabrication

Fig. 1 shows a schematic of a selectively oxidized top-emitting VCSEL. The layers are grown by solid source molecular beam epitaxy. The active region consists of four 6 nm thick GaAs quantum wells embedded in $Al_{0.3}Ga_{0.7}As$ barriers. The nominal gain maximum of this active zone is 830 nm [6]. To prevent funtamental absorbtion in the laser structure only $Al_xGa_{1-x}As$ layers with a minimum AlAs content of 30 % can be used. The lower n-type Si-doped and the

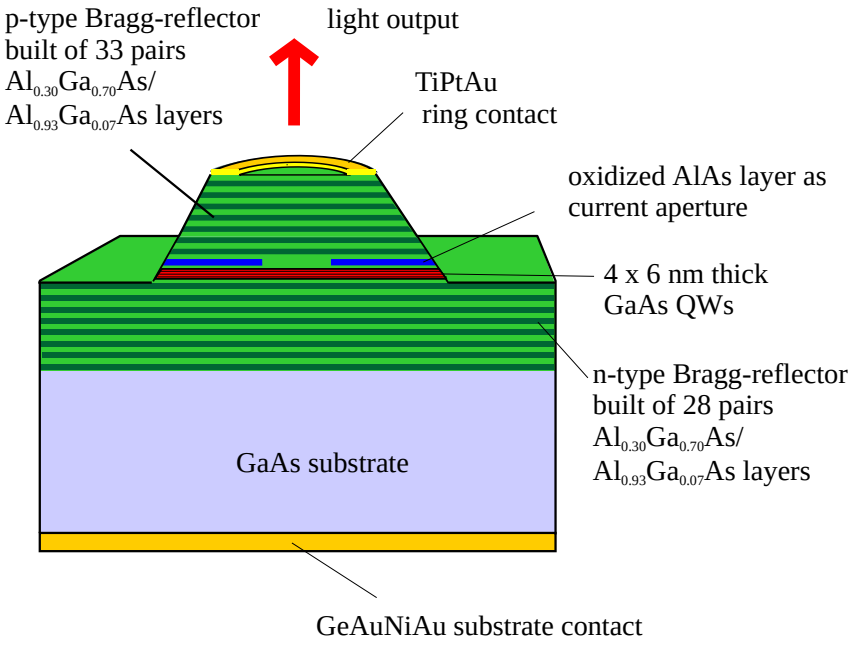

Fig. 1. Cross-sectional view of a top-emitting GaAs VCSEL.

upper p-type C-doped Bragg reflectors consist of 38 and 27 $Al_{0.3}Ga_{0.7}As$-$Al_{0.9}Ga_{0.1}As$ quarter wavelength layer pairs, respectively, with graded interfaces and δ-doping to reduce series resistance. Lateral current confinement is achieved by selective wet oxidation of a 30 nm thin AlAs layer after wet-chemical mesa etching. Single-mode operation is enforced by a small oxide aperture. Shifting the AlAs layer towards the node of the standing wave pattern in the cavity reduces the built-in effective index guiding and the optical losses resulting in increased single-mode output power. After selective oxidation a Ti/Pt/Au ring contact is deposited on the top of the mesa. A broad area Ge/Au/Ni/Au n-contact is evaporated on the backside of the substrate and both contacts are annealed at 410 °C.

3. Characteristics

Fig. 2 shows the optical and electrical characteristics of a VCSEL with 3 μm diameter oxide aperture under CW operation. Threshold current and threshold voltage amount to 3.5 mA and 3.0 V, respectively. The maximum optical output power of 0.3 mW is restricted by thermal roll-over. The differential resistance of 180 Ω at a driving current of 4 mA is typical for these small area devices. The driving voltage of the array is fully compatible with advanced 3.3 V CMOS technology.
Fig. 3 shows emission spectra in CW operation. The emission wavelength of the VCSEL is 749.5 nm on the fundamental transverse mode showing single-mode operation. The side-mode suppression ratio (SMSR) is more than 20 dB.

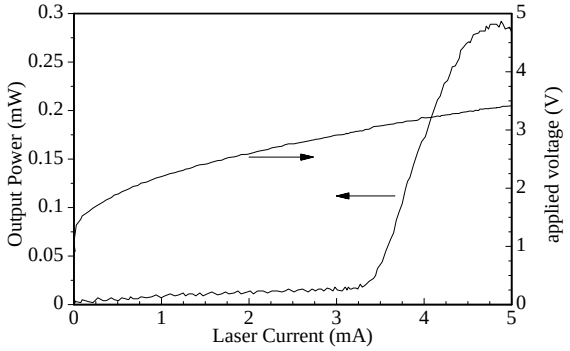

Fig. 2. Optical and electrical characteristics of a typical VCSEL with 3 μm diameter oxide aperture under CW operation. The threshold current is 3.5 mA.

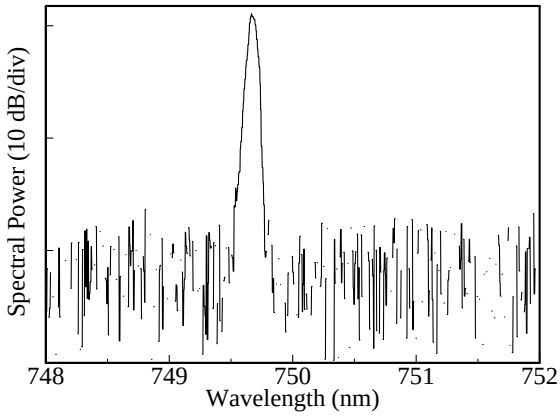

Fig. 3. Optical spectrum of the VCSEL with a current aperture of 3 μm. The laser oscillates at a wavelength of 749.5 nm on the fundamental transverse mode showing single-mode operation.

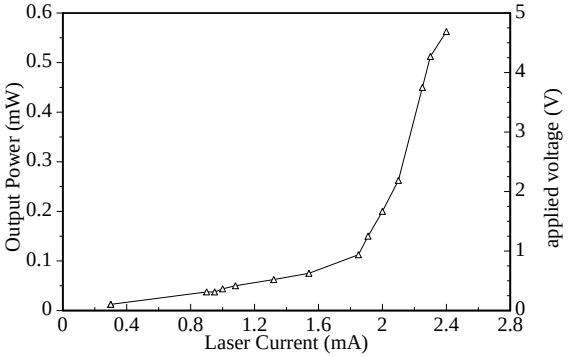

Fig. 4. Optical and electrical characteristics of a VCSEL with 2 μm diameter oxide aperture under pulsed operation with a pulse length of 8 nsec. and a duty cycle of 0.8 %. The threshold current is 20 mA.

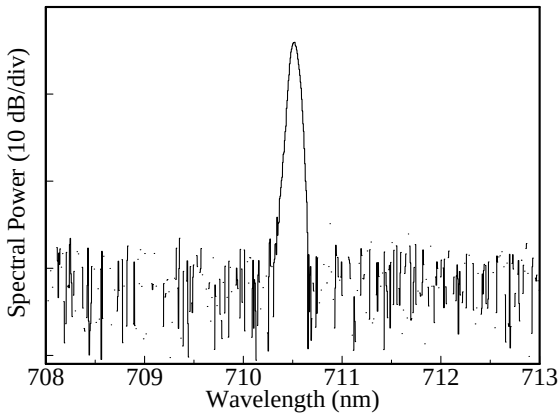

Fig. 5. Optical spectrum of the 2 μm current aperture VCSEL under pulsed operation. The laser oscillates at a wavelength of 710.5 nm on the fundamental transverse mode.

Fig. 4 shows the optical and electrical characteristics of a 710.5 nm VCSEL in pulsed operation with a pulse length of 8 nsec. and a duty cycle of 0.8 %. Threshold current is 20 mA. Fig. 5 shows emission spectra of this VCSEL. The emission wavelength is 710.5 nm on the fundamental transverse mode showing single-mode operation with a SMSR of more than 20 dB.

4. Conclusion

In summary, we have fabricated 710.5 nm and 749.5 nm emission wavelength VCSELs in pulsed and CW operation, respectively, showing more than 0.2 mW transverse single-mode output power. In spite of the large shift between the gain maximum of AlAs free QWs and cavity resonance it was possible to demonstrate CW operation up to a mismatch of 80 nm. Under pulsed condition this shift was even higher reaching a value of 120 nm. This is, to our best knowledge, the highest ever reported detuning for VCSEL operation.

References

[1] H.-E. Shin, Y.-G. Ju, J.-H. Shin, J.-H. Ser, T. Kim, E.-K. Lee, I. Kim, and Y.-H. Lee, '780 nm oxidised vertical-cavvity surface-emitting lasers with $Al_{0.11}Ga_{0.89}As$ quantum wells', *Electron. Lett.*, vol. 32, pp. 1287–1288, 1996.

[2] H.Q. Hou, M. Hagerott Crawford, R.J. Hickman, and B.E. Hammons, 'Room-temperature continuous wave operation of all-AlGaAs visible ($\tilde{7}$00 nm) vertical-cavity surface emitting lasers', *Electron. Lett.*, vol. 32, pp. 1986-1987, 1996.

[3] K.H. Gulden, M. Moser, S. Lscher, and H.P. Schweizer, 'High performance near-IR (765 nm) AlAs/AlGaAs vertical cavity surface emitting lasers', *Electron. Lett.*, vol. 31, pp. 2176-1178, 1995.

[4] Y.H. Lee, B. Tell, K.F. Brown-Goebeler, R.E. Leibenguth, and V.D. Mattera, 'Deep-Red Continuous Wave Top-Surface-Emitting Vertical-Cavity AlGaAs Superlattice Lasers', *IEEE Photon. Technol. Lett.*, vol. 3, pp. 108-109, 1991.

[5] C.S. Shim, J.Y. Yoo, Y.H. Lee, and S.Y. Shin, 'Electrical and Optical Properties of Deep-Red Top-Surface-Emitting Lasers', *IEEE Photon. Technol. Lett.*, vol. 4, pp. 1084-1086, 1992.

[6] E. Zielinski, H. Schweizer, S. Hausser, R. Stuber, M.H. Pilkuhn, and G. Weimann, 'Systematics of Laser Operation in GaAs/AlGaAs Multiquantum Well Heterostructures', *IEEE J. Quantum Electron.*, vol. 23, pp. 969-976, 1987.

Gas Source Molecular Beam Epitaxy of GaAsSb Based Laser Diodes for the Long Wavelength Range

Irene Ecker, Susanne Menzel and Jürgen Joos

We report on the growth of GaAsSb/GaAs laser diodes with Gas Source Molecular Beam Epitaxy (GSMBE). Broad area edge emitting devices are demonstrated which oscillate at wavelengths up to 1242 nm.

1. Introduction

For fiber communication emission wavelengths of 1.3 and 1.55 μm are of great interest. Especially **V**ertical **C**avity **S**urface **E**mitting **L**asers (VCSELs) are ideally suited as transmitter for optical fiber interconnects because of their radial symmetric beam profile which allows high coupling efficiencies into silica fibers [1].

To combine the advantages of common VCSELs at 850 and 980 nm —**D**istributed **B**ragg **R**eflectors (DBR) consisting of AlGaAs/GaAs and lateral current confinement provided by oxiation—with the advantage of emission wavelength at the dispersion and the attenuation minimum of silica glas fiber respectively a material system for the active region of laser diodes based on GaAs is desirable. Recently the materials GaInNAs [2, 3] and GaAsSb [4] seem to be most promising for long wavelength devices.

In our department the growth of GaInNAs using the alternative nitrogen precursors NH_3 and dimethylhydrazine (DMHy) as well as of GaAsSb is investigated. In Fig. 1 the photoluminescence (PL) spectra of a GaInNAs and a GaAsSb sample at an emission wavelength of about 1250 nm are compared. From the logarithmic scale it can be clearly recognized that the PL intensity of the GaAsSb sample is nearly by a factor 1000 higher than that of GaInNAs. Because of this result we decided to fabricate GaAsSb/GaAs **D**ouble **Q**uantum **W**ell (DQW) laser diodes.

2. Epitaxial Growth of GaAsSb with GSMBE

Epitaxial growth is carried out in a modified Riber 32 P GSMBE. The group-III-elements Ga and Al are provided elementally by effusion cells. The hydride arsine (AsH_3) serves as group-V-precursor and is injected through an **H**igh **T**emperature **I**njector (HTI). The group-V-element Sb is provided by a cracker cell. Si is used as n-type dopant. For p-doping CBr_4 is injected through a **L**ow **T**emperature **I**njector (LTI). As substrate Si-doped (100) GaAs of epi-ready quality is used for all samples.

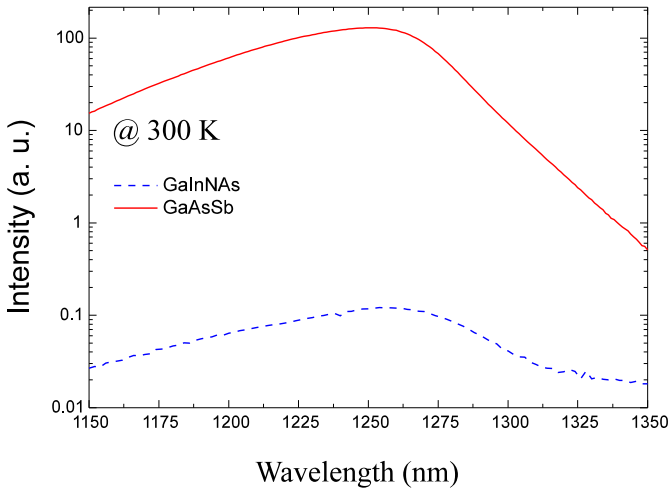

Fig. 1. Comparison of photoluminescence spectra of a GaInNAs sample, grown with the alternative N precursor DMHy, and a GaAsSb sample.

The schematic structure of the investigated edge emitters and the corresponding band diagram is depicted in Fig. 2. The active zone consists of two GaAsSb quantum wells which are embedded in GaAs and sandwiched within a graded index (GRIN) AlGaAs confinement structure and a p- or n-doped AlGaAs layer respectively. A p-doped GaAs contact layer completes the structure.

The course of the band lineup of GaAsSb in GaAs is not clear until now. Ji et al. [5] have claimed a type II heterostructure whereas Prins et al. [6] have determined a type I heterostructure. The hypothesis of a type II heterostructure is more common, however.

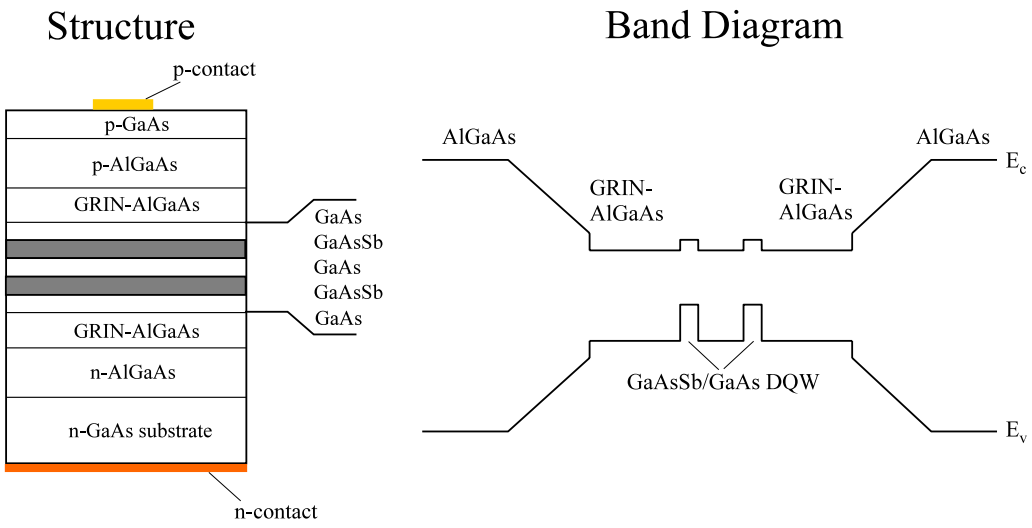

Fig. 2. Schematic structure and band diagram of GaAsSb double quantum well laser diode.

3. Device Fabrication

The processing of the broad area laser test structure is carried out as follows. As first step Ti/Pt/Au stripes with variable widths are deposited on the highly p-doped GaAs cap layer by means of evaporation and lift-off technique. Prior to the metallization the GaAs surface is cleaned with a short HF etching step. Carrier confinement is achieved by wet chemical etching using a sulfuric acid. The etch process is stopped above the active area. After that, the laser sample is thinned from the substrate side to a thickness of about 120 μm by chemo-mechanical polishing in a Br-methanol solution. A Ge/Ni/Au broad area n-contact is evaporated on the polished GaAs substrate. Both contacts are annealed at 410 °C for 10 seconds in a **R**apid **T**hermal **A**nnealer (RTA). Cleaving the sample into individual lasers with a definite length is the final processing step. Fig. 3 shows the schematic of the edge emitting laser diodes.

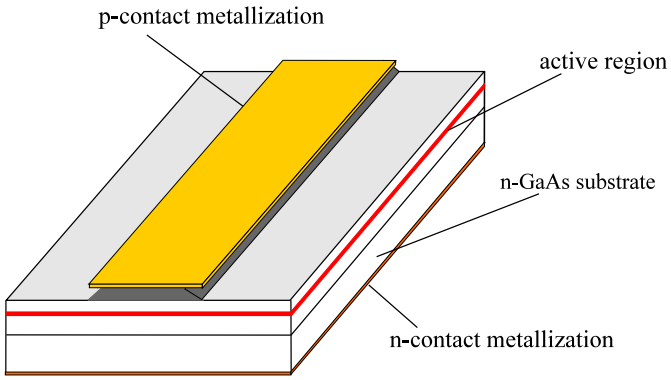

Fig. 3. Device structure of a GaAsSb/GaAs DQW edge emitting laser.

4. Characterization and Device Performance

Fig. 4 shows the room-temperature light-current characteristics of a device with two GaAsSb QWs with an Sb-content over 30 percent. The barrier between the QWs consists of a 15 nm thick GaAs layer. The investigated structure has a length of 800 μm and a width of 20 μm. The device is measured under pulsed operation. The pulse length is 100 ns and the repetition rate 50 kHz. The threshold current density is calculated to be 0.65 kA/cm^2. The corresponding laser spectrum is shown in Fig. 5. The DQW laser diode has an emission wavelength of 1221 nm.

With similar device structures, containing more antimony, laser diodes with emission wavelengths up to 1242 nm are achieved.

5. Summary

We successfully grew GaAsSb/GaAs laser diodes, which emit in the long wavelength range. Broad area diodes were fabricated, which show laser oscillation at 1242 nm. Further investigations will focus on improvements concerning the device characteristics of edge emitting laser diodes and on epitaxial growth of VCSELs.

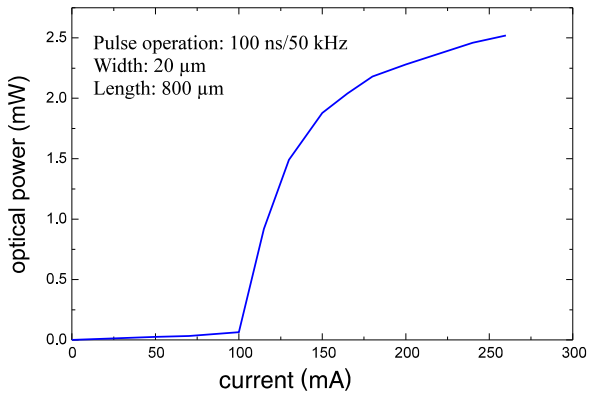

Fig. 4. Light output-current characteristics of GaAsSb/GaAs DQW laser diode under pulsed operation at room temperature.

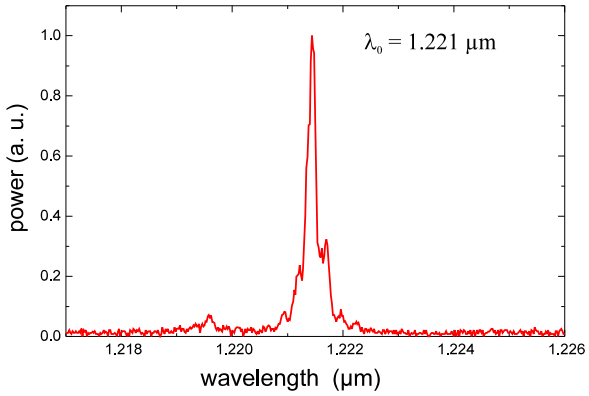

Fig. 5. Emission spectrum of GaAsSb/GaAs laser. The laser oscillates at a wavelength of 1221 nm.

References

[1] K. Tai, G. Hasnain, J.D. Wynn, R.J. Fischer, Y.H. Wang, B. Weir, J. Gamelin, and A.Y. Cho, "90 % Coupling of Top Surface Emitting GaAs/AlGaAs Quantum Well Laser Output into 8 μm Diameter Core Silica Fiber", *Electron. Lett.*, vol. 26, pp. 1628–1629, 1990.

[2] M. Kondow, K. Uomi, A. Niwa, T. Kitatani, S. Watahiki and Y. Yazawa, "GaInNAs: A Novel Material for Long-Wavelength-Range Laser Diodes with Excellent High-Temperature Performance", *Jpn. J. Appl. Phys.*, vol. 35, no. 2B, pp. 1273–1275, 1996.

[3] A. Yu. Egorov, D. Bernklau, D. Livshits, V. Ustinov, Zh. I. Alferov and H. Riechert, "High Power CW operation of InGaAsN lasers at 1.3 μm", *Electron. Lett.*, vol. 35, no. 19, pp. 1643–1644, 1999.

[4] T. Anan, K. Nishi, S. Sugou, M. Yamada, K. Tokutume and A. Gomyo, "GaAsSb: A novel material for 1.3 μm VCSELs", *Electron. Lett.*, vol. 37, no. 3B, pp. 1603–1607, 1998.

[5] G. Ji, S. Agarwala, D. Huang, J. Chyi, and H. Morkoç, "Band lineup in strained $GaAs_{1-x}Sb_x$/GaAs layer multiple quantum wells grown by molecular-beam epitaxy", *Phys. Rev. B*, vol. 38, no. 15, pp. 10571–10577, 1988.

[6] A. D. Prins, D. J. Dunstan, J. D. Lambkin, E. P. O'Reilly, A. R. Adams, R. Pritchard, W. S. Truscott and K. E. Singer, "Evidence of type-I band offsets in strained $GaAs_{1-x}Sb_x$/GaAs quantum wells from high-pressure photoluminescence", *Phys. Rev. B*, vol. 47, no. 4, pp. 2191–2196, 1993.

Ph.D. Theses

[1] Jörg Heerlein, “Laserdioden hoher optischer Ausgangsleistung im Materialsystem InGaAs-AlGaAs-GaAs”, Ph.D. Thesis, Department of Optoelectronics, 1999.

[2] Christian Jung, “Herstellung und Optimierung einmodiger selektiv oxidierter Vertikallaserdioden für die Flip-Chip Technologie”, Ph.D. Thesis, Department of Optoelectronics, 1999.

[3] Hin Yiu Anthony Chung, “Gasquellen-Molekularstrahlepitaxie von InGaAsP Mehrfach-Quantentopf Laserdioden für den Wellenlängenbereich von 1300 nm bis 1500 nm”, Ph.D. Thesis, Department of Optoelectronics, 1999.

[4] Dieter Wiedenmann, “Dynamische Eigenschaften und Rauschen selektiv oxidierter Vertikallaserdioden”, Ph.D. Thesis, Department of Optoelectronics, 1999.

[5] Bernhard Weigl, “Technologie und Charakterisierung hocheffizienter InGaAs-Vertikallaserdioden”, Ph.D. Thesis, Department of Optoelectronics, 1999.

[6] Jochen Heinrich, “Vertikallaser als optische Sendeelemente in Datenbussen für den Einsatz in mobilen Systemen”, Ph.D. Thesis, Department of Optoelectronics, 1999.

[7] Arthur Pelzmann, “Charakterisierung und Optimierung von Leuchtdioden auf der Basis von GaN”, Ph.D. Thesis, Department of Optoelectronics, 1999.

Diploma Theses and Semester Projects

[1] Raphael Ehrbrecht, "Hybridintegration von zweidimensionalen Vertikallaserdiodenarrays mit planaren Hochfrequenz-Leitungen", Diploma Thesis, Department of Optoelectronics, 1999.

[2] Cüneyt Gürel, "Herstellung und Charakterisierung von Halbleiter-Laserdioden mit gekrümmten Resonatoren", Diploma Thesis, Department of Optoelectronics, 1999.

[3] Stephane Lendroit, "Realisation de lasers a cavite verticale emettant un rayonnement de logueur d´onde 850 nm au transvers de leur substrat", Diploma Thesis, Department of Optoelectronics, 1999.

[4] Marcus Scherer, "Optimierung der Kontakttechnologie für GaN basierende Leuchtdioden", Diploma Thesis, Department of Optoelectronics, 1999.

[5] Michael C. Riedl, "Herstellung und Charakterisierung transversal einmodiger oberflächenemittierender Laserdioden mit Vertikalresonator großer aktiver Durchmesser", Diploma Thesis, Department of Optoelectronics, 1999.

[6] Raphael Ehrbrecht, "Aufbau einer Temperaturregelung zur Vermessung von Vertikallaserdioden im Temperaturbereich von -40 bis 85 °C", Semester Project, Department of Optoelectronics, 1999.

[7] Michael C. Riedl, "Stabilisierung der Fundamentalmode in Oberflächenemittern durch modenselektive Reflektivitätsverteilung", Semester Project, Department of Optoelectronics, 1999.

[8] Christoph Schwörer, "Untersuchung des Einflusses der Verstimmung zwischen Resonanzwellenlänge und Wellenlänge des maximalen Gewinns auf die intrinsischen dynamischen Eigenschaften von Vertikallaserdioden", Semester Project, Department of Optoelectronics, 1999.

[9] Daniel Supper, "Herstellung von Gold-Zinn Lot und Prozessierung von strukturierten Wärmesenken", Semester Project, Department of Optoelectronics, 1999.

[10] Markus Bschorr, "Temperaturverhalten von p- und n-Kontakten auf GaAs", Semester Project, Department of Optoelectronics, 1999.

[11] Axel Straub, "Nasschemische Nanostrukturierung zur Erhöhung der Auskoppeleffizienz von GaN-basierenden Leuchtdioden", Semester Project, Department of Optoelectronics, 1999.

[12] Jan Grünenpütt, "Untersuchung statischer Emissionseigenschaften an vertikal emittierenden Laserdioden auf verkipptem Substrat", Semester Project, Department of Optoelectronics, 1999.

[13] Sven-Silvius Schad, "Temperaturverhalten von GaN basierenden Leuchtdioden", Semester Project, Department of Optoelectronics, 1999.

[14] Christoph Eichler, "Charakterisierung des elektrischen Kennlinienverhaltens von GaN-basierenden LED- und Laserstrukturen", Semester Project, Department of Optoelectronics, 1999.

Talks

[1] H.Y.A. Chung, C. Wang, M. Kamp, K.J. Ebeling, R. Beccard, and M. Heuken, "Hydride vapour phase epitaxy of GaN on Sapphire", DGKK-Arbeitskreis, *Epitaxie von III/V- Halbleitern*, Stuttgart-Büsnau, Germany, Dec., 1999.

[2] H.Y.A. Chung, C. Wang, C. Kirchner, M. Seyboth, V. Schwegler, M. Scherer, M. Kamp, K.J. Ebeling, R. Beccard, and M. Heuken, "Hydride vapour phase epitaxy growth of GaN layers under reduced reactor pressure", *presented at ISBLLED 2000*, Berlin, Germany, Mar., 2000.

[3] K.J. Ebeling, "Eigenschaften und Anwendungen neuartiger Laserdioden mit Vertikalresonator", *Kolloquium Lasertechnik*, Frauenhofer Institut für Lasertechnik, Aachen, Germany, Feb., 1999.

[4] K.J. Ebeling, "Mikrooptische Systeme, Vertikallaserdioden: Eigenschaften und Anwendungen", *WE-Heraeus-Seminar*, DPG-Schule für Physik, Bad Honnef, Germany, Feb., 1999.

[5] K.J. Ebeling, "Vertikallaserdioden als Lichtquellen in Mikrosystemen", *Graduiertenkolleg Mikrosystemtechnik*, Universität Kassel, Germany, July, 1999.

[6] K.J. Ebeling, "Low noise single-mode VCSELs for high speed optical data transmission", *European Research Conf. Quantum Optics*, Cala Vinas, Mallorca, Oct., 1999.

[7] K.J. Ebeling, "Neuartige Halbleiterlaserquellen für die optische Informationstechnik", *Physikalisches Kolloquium*, Universität Oldenburg, Germany, Oct., 1999.

[8] K.J. Ebeling, "Hochbitratige optische Datenübertragung mit selektiv oxidierten Vertikallaserdioden", *Photonik-Seminar*, Institut für Hochfrequenztechnik und Quantenelektronik, Universität Karlsruhe, Germany, Dec., 1999.

[9] I. Ecker, S. Menzel, M. Kamp, and K.J. Ebeling, "Wachstum von GaNAs- und GaInNAs-Schichten mittels Gasquellen-Molekularstrahlepitaxie", *VW Photonik Symposium*, Duisburg, Germany, Sep., 1999.

[10] M. Golling, H.Y.A. Chung, K.J. Ebeling, G. Stareev, and J. Mähnß, "Kohlenstofftetrabromid (CBr_4) und Siliziumtetrabromid ($SiBr_4$) als alternative Dotierquellen in der Gasquellen-MBE", DGKK-Arbeitskreis, *"Epitaxie von III/V- Halbleitern"*, Stuttgart-Büsnau, Germany, Dec., 1999.

[11] M. Golling, "Wachstum von InGaP/InAlGaP für optoelektronische Anwendungen", *MBE Workshop 99*, Phys. Inst. der Univ. Würzburg, Würzburg, Germany, Sept., 1999.

[12] M. Grabherr, "Grundlegende Untersuchungen zur Technologie von Hochleistungsdiodenlasern – Teilvorhaben: Leistungslaserdioden mit Vertikalresonator", *Jahrestagung Laser 2000, NOVALAS*, Freiburg, Germany, Feb., 1999.

[13] M. Kamp, "GaN-Technologie Bauelemente mit 14% Fehlanpassung und 1010 Versetzungen/cm^2", *Ferdinand-Braun Institut für Höchstfrequenztechnik*, Berlin, Germany, Mar., 1999.

[14] M. Kamp, "Neue Halbleiter für die Optoelektronik: Quantenpunkte und Nitride für IR bis UV", *WE-Heraeus-Ferienkurs für Physik, Technologie und Anwendungen von Gruppe III Nitriden*, Magdeburg, Germany, Sep., 1999.

[15] M. Kamp, V. Schwegler, C. Kirchner, M. Seyboth, H.Y.C. Chung, and K.J. Ebeling, "Charakterisierung GaN-basierender LEDs und Laserstrukturen unter Strominjektion,", *VW Photonik Symposium*, Duisburg, Germany, Sep., 1999.

[16] M. Kamp, V. Schwegler, C. Kirchner, H.Y.A. Chung, C. Wang, M. Seyboth, M. Scherer, and K.J. Ebeling, "GaN-based light emitters on quasi-substrates", *accepted for presentation at ISBLLED 2000*, Berlin, Germany, Mar., 2000.

[17] C. Kirchner, F. Eberhard, V. Schwegler, M. Kamp, K.J. Ebeling, K. Kornitzer, K. Thonke, R. Sauer, P. Prystawko, M. Leszczynski, I. Grzegory, and S. Porowski, "Homoepitaxial growth of high quality GaN by MOVPE", *EW MOVPE VIII*, Prag, Czechoslovakia, June, 1999.

[18] F. Mederer, "Experimente mit GI-POF", *ITG-FG 5.4.1 Optische Polymerfasern*, Stuttgart, Germany, Sept., 1999.

[19] F. Mederer, R. Jäger, M. Kicherer, H. Unold, and K.J. Ebeling, "GaAs-basierende VCSEL für hochbtratige optische Datenübertragung", *DPG Frühjahrstagung*, Regensburg, Germany, Mar., 2000.

[20] R. Michalzik, K.J. Ebeling, R. King, C. Jung, J. Joos, F. Mederer, R. Jäger, and G. Giaretta, "Efficient VCSELs and arrays for high-speed data transmission", *1999 OSA Annual Meeting*, Santa Clara, CA, USA, Sep., 1999.

[21] M. Miller, "Growth and characterization of passive and active VCSRs (Vertical Cavity Semiconductor Resonators) for creation of spatial solitons", *PIANOS Review Meeting*, Brussels, Belgium, Dec., 1999.

[22] M. Miller, "Grundlegende Untersuchungen zur Technologie von Hochleistungsdiodenlasern-Teilvorhaben: Leistungslaserdioden mit Vertikalresonator", *Jahrestagung Laser 2000, NOVALAS*, Düsseldorf, Germany, Oct., 1999.

[23] P. Unger, "Halbleiterlaser – Physik, Technologie und Anwendung", *Physikalisches Kolloquium*, Universität Kaiserslautern, Germany, Jan., 1999.

[24] P. Unger, "Patterning of nanometer-scale structures by dry-etching techniques", *Micro- and Nanostructures: Development, Characterization, Application*, Seminar des Graduiertenkollegs, *Molecular organization and dyamics of interfaces and surfaces*, University of Ulm, Germany, May, 1999.

[25] P. Unger, "New concepts for high-power semiconductor diode lasers", *CLEO Europe, EQEC Focus Meetings, Novel lasers and devices – basic aspects*, Munich, Germany, June, 1999.

[26] P. Unger, "Halbleiter-Diodenlaser-Physik, Technologie, Anwendung", *Physikalisches Kolloquium*, Universität Kiel, Germany, Nov., 1999.

[27] P. Unger, "Physik und Anwendung von Halbleiter-Laserdioden", Seminar des Graduiertenkollegs, *Nanoelektronische, Mikromechanische und Mikrooptische Systeme*, Ruhr Universität Bochum, Germany, Nov., 1999.

[28] V. Schwegler, C. Kirchner, and M. Kamp, "Properties and Progress in GaN Homoepitaxy", Photonics Center, University of Boston, Boston, USA, Nov., 1999.

[29] M. Brunfaut, J. Depreitere, W. Meeus, J.M. Van Campenhout, H. Melchior, R. Annen, P. Zenklusen, R. Baets, L. Vanwassenhove, J. Hall, B. Wittman, P. Heremans, R. King, H. Thienpont, and J. Van Koetsem, "The OIIC optoelectronic FPGA demonstrator", *MEL-ARI OPTO third annual workshop*, Athens, Greece, Oct., 1999.

[30] I. Daumiller, P. Schmid, E. Kohn, C. Kirchner, M. Kamp, and K.J. Ebeling, "Dispersion-free AlN/n-GaN HFET structure", *WOCSEMAD 99*, New Orleans, USA, Feb., 1999.

[31] J.P. Hall, R. Baets, R. Annen, P. Zenclusen, K.J. Ebeling, A. Neyer, B. Wittmann, V. Baukens, and H. Thienpont, "Components for 1 Gbit/s/channel, 2-D array optically interconnected CMOS for the OIIC 'Gigalink Demonstrator", *MEL-ARI OPTO third annual workshop*, Athens, Greece, Oct., 1999.

[32] R.A. Talalaev, E.V. Yakolev, S.Y. Karpov, Y.M. Makarov, C. Kirchner, and M. Kamp, "Analysis of indium incorporation efficiency during metal organic vapor phase epitaxy of InGaN", *Proceedings of EW-MOVPE*, Prag, CSR, 1999.

Publications and Conference Contributions

[1] H.Y.A. Chung, G. Stareev, J. Joos, M. Golling, J. Mähnß, and K.J. Ebeling, "Gas source MBE growth of 1.3 μm-InGaAsP quantum wells GRINSCH laser showing low threshold current density and high output power", *J. Crystal Growth*, vol. 201/202, pp. 909–913, 1999.

[2] F. Eberhard, M. Schauler, E. Deichsel, C. Kirchner, and P. Unger, "Comparison of the etching behavior of GaAs and GaN in a chemically-assisted ion-beam etching system", *Microelectronic Engineering*, vol. 46, pp. 323–326, 1999.

[3] M. Grabherr, M. Miller, R. Jäger, R. Michalzik, U. Martin, H. Unold, and K.J. Ebeling, "High–power VCSELs: single devices and densely packed 2-D-arrays", *IEEE J. Selected Topics Quantum Electron.*, vol. 5, pp. 495–502, 1999.

[4] M. Grabherr, M. Miller, R. Jäger, and K.J. Ebeling, "Reliable 1 W VCSEL module for high optical power density", in Proc. *IEEE 12th Annual Meeting LEOS'99*, vol. 1, pp. 265–266, San Francisco, CA, USA, Nov., 1999.

[5] J. Heerlein, S. Gruber, M. Grabherr, R. Jäger, and P. Unger, "Highly-efficient laterally oxidized λ = 950 nm InGaAs/AlGaAs single-mode lasers", *IEEE J. Selected Topics Quantum Electron.*, vol. 5, pp. 701–705, 1999.

[6] R. Jäger, D. Wiedenmann, M. Grabherr, C. Jung, M. Kicherer, R. King, F. Mederer, M. Miller, P. Schnitzer, and K.J. Ebeling, "Shot noise limited VCSEL for high speed fiber optic data transmission (invited)", in *ISPA'99, SPIE Proc.*, vol. 3896, pp. 116–132, Nanyang, Singapore, Nov., 1999.

[7] R. Jäger, J. Heerlein, E. Deichsel, and P. Unger, "63 % wallplug efficiency MBE grown InGaAs/AlGaAs broad-area laser diodes and arrays with carbon p-type doping using CBr_4", *J. Crystal Growth*, vol. 201/202, pp. 882–885, 1999.

[8] J. Joos, F. Mederer, M. Kicherer, I. Ecker, R. Jäger, W. Schmid, M. Grabherr, and K.J. Ebeling, "1129 nm InGaAs VCSELs for 2.5 Gbit/s data transmission over 10 km standard single-mode fiber", in Proc. *ECOC'99*, vol. 2, pp. 296–297, Nice, France, Sept., 1999.

[9] G. Jost, E. Deichsel, J. Heerlein, R. Jäger, R. King, U. Martin, and P. Unger, "3 Gb/s high-power optical data transmission system", in Proc. *International Microwave and Optoelectronics Conference, IMOC'99*, Rio de Janeiro, Brazil, Aug., 1999.

[10] C. Jung, R. King, R. Jäger, M. Grabherr, F. Eberhard, R. Rösch, U. Martin, D. Wiedenmann, H.J. Unold, R. Michalzik, and K.J. Ebeling, "64 channel flip-chip mounted selectively oxidized GaAs VCSEL array for parallel optical interconnects", in *Vertical-Cavity Surface-Emitting Lasers III, SPIE Proc.*, vol. 3627, pp. 143–151, San Jose, CA, USA, Jan., 1999.

[11] C. Jung, R. King, M. Grabherr, F. Eberhard, R. Michalzik, and K.J. Ebeling, "Highly efficient oxide-confined VCSEL arrays for parallel optical interconnects", *J. Opt. A, Pure Appl. Opt.*, vol. 1, pp. 272–275, 1999.

[12] M. Kamp, A. Pelzmann, C. Kirchner, M. Mayer, K.J. Ebeling, M. Leszczynski, I. Grzegory, T. Suski, and S. Porowski, "GaN homoepitaxy for Device Applications (invited)", *MRS Internet J. Nitride Semicond. Res. 4S1, G10.2*, 1999.

[13] R. King, R. Michalzik, D. Wiedenmann, R. Jäger, P. Schitzer, T. Knödl, and K. J. Ebeling, "2D VCSEL arrays for chip-level optical interconnects", in *Vertical-Cavity Surface-Emitting Lasers III, SPIE Proc.*, vol. 3632, pp. 363–372, San Jose, CA, USA, Jan., 1999.

[14] R. King, P. Schnitzer, F. Mederer, M. Kicherer, R. Jäger, and K.J. Ebeling, "Vertikallaserdioden – Schlüsselkomponenten für die optische Datenübertragung auf Chipebene", in *ITG Workshop, Photonische Integration und Aufbautechnik, Artikel 14*, Berlin, Germany, 1999.

[15] C. Kirchner, V. Schwegler, F. Eberhard, M. Kamp, K.J. Ebeling, K. Kornitzer, T. Ebner, K. Thonke, R. Sauer, P. Prystawko, M. Leszczynski, I. Grzegory, and S. Porowski, "Homoepitaxial growth of GaN by metalorganic vapor phase epitaxy: a benchmark for GaN technology", *Appl. Phys. Lett.*, vol. 75, pp. 1098–1100, 1999.

[16] T. Knödl, R. Jäger, M. Grabherr, R. King, M. Kicherer, M. Miller, F. Mederer, and K.J. Ebeling, "CW room temperature operation of a diode cascade InGaAs-AlGaAs quantum well VCSEL", in Proc. *IEEE 12th Annual Meeting LEOS'99*, vol. 1, pp. 143–144, San Francisco, CA, USA, Nov., 1999.

[17] T. Knödl, H.K.H. Choy, J.L. Pan, R. King, R. Jäger, G. Lullo, J.F. Ahadian, R.J. Ram, Jr. C.G. Fonstad, and K.J. Ebeling, "RCE photodetectors based on VCSEL structures", *IEEE Photon. Technol. Lett.*, vol. 11, pp. 1289–1291, 1999.

[18] M. Mayer, A. Pelzmann, H.Y.A. Chung, M. Kamp, and K.J. Ebeling, "Reactive MBE of group III nitrides: high quality homoepitaxial GaN and ultra-violet emitting diodes", *J. Cryst. Growth*, vol. 201/202, pp. 318–322, 1999.

[19] F. Mederer, C. Jung, R. Jäger, M. Kicherer, R. Michalzik, P. Schnitzer, D. Wiedenmann, and K.J. Ebeling, "12.5 Gbit/s data rate fiber transmission using single-mode selectively oxidized GaAs VCSELs at λ=850 nm", in *Proc. IEEE 12th Annual Meeting LEOS'99*, vol. 2, pp. 697–698, San Francisco, CA, USA, Nov., 1999.

[20] F. Mederer, R. Jäger, P. Schnitzer, , H. Unold, M. Kicherer, K.J. Ebeling, M. Naritomi, and R. Yoshida, "Multi-Gigabit/s perfluorinated garded-index plastic-optical-fiber data links with butt-coupled single-mode InGaAs VCSEL", in *ISPA'99, SPIE Proc.*, vol. 3896, pp. 273–280, Nanyang, Singapore, Nov., 1999.

[21] R. Michalzik, R. King, D. Wiedenmann, P. Schnitzer, and K. J. Ebeling, "Modeling and application of VCSELs for optical interconnection (invited)", in *Physics and simulation of optoelectronic devices VII, SPIE Proc.*, vol. 3625, San Jose, CA, USA, Jan., 1999.

[22] R. Michalzik, G. Giaretta, A.J. Ritger, and Q.L. Williams, "10 Gb/s VCSEL based data transmission over 1.6 km of new generation 850 nm multimode fiber", in *Proc. IEEE 12th Annual Meeting LEOS'99,* postdeadline paper, *PD1.6,* San Francisco, CA, USA, Nov., 1999.

[23] M. Schauler, F. Eberhard, C. Kirchner, V. Schwegler, A. Pelzmann, M. Kamp, K.J. Ebeling, F. Bertram, T. Riemann, J. Christen, P. Prystawko, M. Leszczynski, I. Grzegory, and S. Porowski, "Dry-etching of GaN substrates for high-quality homoepitaxy", *Appl. Phys. Lett.*, vol. 74, pp. 1123–1125, 1999.

[24] W. Schmid, F. Eberhard, M. Schauler, M. Grabherr, R. King, M. Miller, E. Deichsel, G. Stareev, U. Martin, R. Jäger, J. Joos, R. Michalzik, and K.J. Ebeling, "Infrared light-emitting diodes with lateral outcoupling taper for high extraction efficiency", in *Light-emitting diodes: research, manufacturing, and applications III, SPIE Proc.*, vol. 3621, pp. 198–205, San Jose, CA, USA, Jan., 1999.

[25] P. Schnitzer, M. Grabherr, R. Jäger, F. Mederer, R. Michalzik, D. Wiedenmann, and K.J. Ebeling, "GaAs VCSEL's at λ = 780 and 835 nm for short distance 2.5 Gb/s plastic optical fiber data links", *IEEE Photon. Technol. Lett.*, vol. 11, pp. 767–777, 1999.

[26] P. Schnitzer, F. Mederer, H.J. Unold, R. Jäger, M. Kicherer, K.J. Ebeling, M. Naritomi, and R. Yoshida, "7 Gb/s data rate transmission using InGaAs VCSEL at λ = 950 nm and perfluorinated GI POF", in Proc. *International POF Conference '99*, pp. 209–210, Chiba, Japan, July, 1999.

[27] V. Schwegler, C. Kirchner, M. Seyboth, M. Kamp, K.J. Ebeling, Yu. Melnik, A. Nikolaev, D. Tsvetkov, and V. Dmitriev, "GaN/SiC quasi-substrates for GaN-based LEDs", *Phys. Stat. Sol. (A)*, vol. 176, pp. 99–102, 1999.

[28] V. Schwegler, S.S. Schadt, C. Kirchner, M. Seyboth, M. Kamp, K.J. Ebeling, V.E. Kudryashov, A.N. Turkin, A.E. Yunovich, U. Stempfle, A. Link, W. Limmer, and R. Sauer, "Ohmic heating of LEDs during operation: determination of the junction temperature and its influence on device performance", *Phys. Stat. Sol. (A)*, vol. 176, pp. 783–786, 1999.

[29] P. Unger, "New concepts for high-power semiconductor diode lasers in novel lasers and devices – basic aspects", *OSA Technical Digest*, p. 38, 1999.

[30] H.J. Unold, M. Grabherr, F. Eberhard, F. Mederer, R. Jäger, M. Riedl, and K.J. Ebeling, "An increased-area oxidized single-fundamental mode VCSEL with a self-aligned shallow etched surface relief", *Electron. Lett.*, vol. 35, pp. 1340–1341, 1999.

[31] D. Wiedenmann, R. King, C. Jung, R. Jäger, R. Michalzik, P. Schnitzer, M. Kicherer, and K.J. Ebeling, "Design and analysis of single-mode oxidized VCSELs for high-speed optical interconnects", *IEEE J. Selected Topics Quantum Electron.*, vol. 5, pp. 503–511, 1999.

[32] D. Wiedenmann, M. Kicherer, C. Jung, M. Grabherr, M. Miller, R. Jäger, and K.J. Ebeling, "Sub-poissonean intensity noise from vertical-cavity surface-emitting lasers", *Appl. Phys. Lett.*, vol. 75, pp. 3075–3077, 1999.

[33] C. Bozdog, H. Przybylinska, G. D. Watkins, V. Härle, F. Scholz, M. Mayer, M. Kamp, R.J. Molnar, and B. Molnar, "Optical detection of electron paramagnetic resonance in electron-irradiated GaN", *Phys. Rev. B*, vol. 59, pp. 12 480 – 12 486, 1999.

[34] G. Giaretta, F. Mederer, R. Michalzik, W. White, R. Jäger, G. Shevchuk, T. Onishi, M. Naritomi, R. Yoshida, P. Schnitzer, H. Unold, M. Kicherer, K. Al-Hemyari, J.A. Valdmanis, M. Nuss, X. Quan, and K.J. Ebeling, "Demonstration of 500 nm wide Transmission window at multi-Gb/s data rates in low-loss plastic optical fiber", in *Proc. ECOC'99*, vol. 2, pp. 240–241, Nice, France, Sept., 1999.

[35] R. Cheung, S. Withanage, R.J. Reeves, S.A. Brown, I. Ben-Yaacov, C. Kirchner, and M. Kamp, "Reactive ion etched-induced effects on the near-band-edge luminescence in GaN", *Appl. Phys. Lett.*, vol. 74, pp. 3185–3187, 1999.

[36] H. Martinsson, J.A. Vukušić, M. Grabherr, R. Michalzik, R. Jäger, K.J. Ebeling, and A. Larsson, "Transverse mode selection in large area oxide-confined vertical-cavity surface-emitting lasers using a shallow surface relief", *IEEE Photon. Technol. Lett.*, vol. 11, pp. 1536–1538, 1999.

[37] P. Prystawko, M. Leszczynski, A. Sliwinski, H. Teisseyre, T. Suski, M. Bockowski, S. Porowski, J. Domagała, C. Kirchner, A. Pelzmann, M. Schauler, and M. Kamp, "Epitaxy of ternary nitrides on GaN single crystal", *J. Crystal Growth*, vol. 198/199, pp. 1061–1065, 1999.

[38] B. Wittmann, A. Neyer, F. Mederer, R. King, and R. Michalzik, "Optical interconnect based on 62-μm-core POF", in Proc. *International POF Conference '99*, pp. 140–143, Chiba, Japan, July, 1999.

[39] T. Ackemann, J.R. Tredicce, R. Jäger, and K.J. Ebeling, "Spatial Structure of broad-area vertical-cavity surface-emitting lasers", in Proc. *Quantum Electronics and Laser Sciences Conference 1999, OSA Technical Digest Series*, p. 228, Baltimore, MD, USA, May, 1999.

[40] D. Mistele, J. Aderhold, H. Klausing, T. Rotter, O. Semchinova, J. Stemmer, D. Uffmann, J. Graul, C. Ahrens, F. Eberhard, M. Mayer, M. Schauler, and M. Kamp, "Influence of preetching on specific contact parameters for metal-GaN contacts", *Semiconductor Science and Technology*, vol. 14, pp. 637–641, 1999.

[41] C. Bozdog, H. Przybylinska, G.D. Watkins, V. Härle, F. Scholz, M. Mayer, M. Kamp, R.J. Molnar, A.E. Wickenden, D.D. Koleske, and R.L. Henry, "Optical detection of electron paramagnetic resonance in electron-irradiated GaN", *Phys. Rev. B*, vol. 59, pp. 12479–12486, 1999.

[42] I. Daumiller, C. Kirchner, M. Kamp, K.J. Ebeling, and E. Kohn, " Evaluation of the temperature stability of AlGaN/GaN heterostructure FETs", *IEEE Electron Device Lett.*, vol. 20, pp. 448–451, 1999.

[43] K. Kornitzer, M. Grehl, K. Thonke, R. Sauer, C. Kirchner, V. Schwegler, M. Kamp, M. Leszczynski, I. Grzegory, and S. Porowski, "High resolution PL spectra of donor- and acceptor-bound excitons in homoepitaxial GaN-layers", *Phys. Rev. Lett.*, vol. 60, pp. 1471–1473, 1999.

[44] I. Daumiller, E. Kohn, C. Kirchner, M. Kamp, K.J. Ebeling, L. Pond, and C.E. Wetzel, "DC and RF characteristics of AlN/GaN doped channel heterostructure field effect transistors", *Electron. Lett.*, vol. 35, pp. 1588–1590, 1999.

[45] A. Link, K. Bitzer, W. Limmer, R. Sauer, C. Kirchner, V. Schwegler, M. Kamp, D. Ebling, and K.W. Benz, "Temperature dependence of the E2 and A1 (LO) phonons in GaN and AlN", *J. Appl. Phys.*, vol. 86, pp. 6256–6260, 1999.

[46] K. Kornitzer, T. Ebner, M. Grehl, K. Thonke, R. Sauer, C. Kirchner, V. Schwegler, F. Eberhard, M. Kamp, K.J. Ebeling, M. Leszczynski, I. Grzegory, and S. Porowski, "High resolution photoluminescence and reflectance spectra of homoepitaxial GaN layers", *Phys. Stat. Sol. (B)*, vol. 216, pp. 5–10, 1999.

[47] S.A. Brown, R.J. Reeves, C.S. Haase, R. Cheung, C. Kirchner, and M. Kamp, "Reactive ion etched GaN: metastable defects and yellow luminescence", *Appl. Phys. Lett.*, vol. 75, pp. 3285–3287, 1999.

[48] I. Daumiller, P. Schmid, C. Kirchner, M. Kamp, L. Pond, K.J. Ebeling, C.E. Wetzel, and E. Kohn, "DC and RF characterization of AlN/GaN HFETs", *Phys. Stat. Sol. (A)*, vol. 176, pp. 179–182, 1999.

[49] P. Fischer, M. Zacharias, J. Christen, V. Schwegler, C. Kirchner, and M. Kamp, "Scanning electroluminescence microscopy – a powerful novel characterization tool for light emitting diodes", *Phys. Stat. Sol. (A)*, vol. 176, pp. 119–124, 1999.

[50] S. Heppel, R. Wirth, J. Off, F. Scholz, A. Hangleiter, H. Obloh, J. Wagner, C. Kirchner, and M. Kamp, "Mode conversion in GaN based laser structures on sapphire due to the birefringence of the nitrides", *Phys. Stat. Sol. (A)*, vol. 176, pp. 73–78, 1999.

[51] R. Cheung, R.J. Reeves, B. Rong, S.A. Brown, E.J.M. Fakkeldij, E. van der Drift, and M. Kamp, "High resolution reactive ion etching of GaN and etch-induced effects", *J. Vac. Sci. Technol. B*, vol. 17, pp. 2759–2763, 1999.

[52] B. Wittmann, M. Jöhnck, A. Neyer, F. Mederer, R. King, and R. Michalzik, "POF-based interconnects for intracomputer applications", *IEEE J. Sel. Top. Quantum Electron.*, vol. 5, pp. 1243–1248, 1999.

[53] G. Giaretta, R. Michalzik, W. White, G. Shevchuk, T. Onishi, M. Naritomi, R. Yoshida, M. Nuss, and X. Quan, "11 Gbps data transmission through 100 m of perfluorinated graded index polymer optical fiber", in *POF World '99*, p. 30, San Jose, CA, USA, June, 1999.

Submitted Publications and Conference Contributions

[1] K.J. Ebeling, R. King, M. Kicherer, F. Mederer, H. Unold, J. Joos, R. Jäger, I. Ecker, and M. Golling, "Low-noise high-speed VCSELs and arrays for optical interconnects", in Proc. *Int. Symp. on Ultra-Parallel Optoelectronics*, Kawasaki, Japan, Feb., 2000.

[2] K.J. Ebeling, F. Mederer, H. Unold, T. Knödl, M. Kicherer, M. Golling, R. Jäger, and R. Michalzik, "High performance VCSELs for Optical Data Links", in *Fifth Optoelectronics and Communications Conf., OECC 2000*, Makuhari Messe, Chiba, Japan, July, 2000, to be presented.

[3] J. Joos, F. Mederer, M. Kicherer, I. Ecker, R. Jäger, W. Schmid, M. Grabherr, and K.J. Ebeling, "2.5 Gbit/s data transmission over 10 km standard single-mode fiber using InGaAs VCSELs at 1.13 μm emission wavelength", *IEEE Photon. Technol. Lett.*, vol. 12, pp. 344–346, 2000.

[4] M. Kamp and H. Riechert, "MBE growth of GaN and related compounds", Book Chapter in *Properties of GaN and Related Compounds, J.H.Edgar (ed.), INSPEC Datas Review Reries*, pp. 426–439, 2000.

[5] M. Kamp, "Solutions for heteroepitaxial growth of GaN and their impact on devices (invited)", *Optical and Quantum Electronics (special issue)*, 2000, in press.

[6] M. Kamp, A. Pelzmann, C. Kirchner, M. Mayer, and K.J. Ebeling, "Progress in GaN homoepitaxy (invited)", *Semiconductor Science and Technology*, 2000, in press.

[7] M. Kicherer, D. Wiedenmann, and K.J. Ebeling, "High speed phenomena in vertical-cavity surface-emitting laser diodes", *Nonlinear Optics*, 2000, in press.

[8] C. Kirchner, V. Schwegler, F. Eberhard, M. Kamp, K.J. Ebeling, P. Prystawko, M. Leszczynski, I. Grzegory, and S. Porowski, "MOVPE homoepitaxy of high-quality GaN: crystal growth and devices (invited)", *Progress in Crystal Growth*, 2000, in press.

[9] F. Mederer, R. Jäger, P. Schnitzer, H. Unold, M. Kicherer, K.J. Ebeling, M. Natomi, and R. Yoshida, "Multi-Gigabit/s graded-index POF data link with butt-coupled single-mode InGaAs VCSEL", *IEEE Photon. Technol. Lett.*, vol. 12, pp. 199–201, 2000.

[10] F. Mederer, M. Kicherer, H. Unold, and K.J. Ebeling, "2.5 Gbit/s data transmission with single-mode GaAs VCSELs over a -20°C to 100°C temperature range", *Electron. Lett.*, vol. 36, pp. 236–238, 2000.

[11] F. Mederer, M. Grabherr, F. Eberhard, I. Ecker, R. Jäger, J. Joos, C. Jung, M. Kicherer, R. King, P. Schnitzer, H. Unold, D. Wiedenmann, and K.J. Ebeling, "High performance selectively oxidized VCSELs and arrays for parallel high-speed optical interconnects", *Advances in Solid State Physics*, 1999, submitted.

[12] F. Mederer, R. Jäger, P. Schnitzer, H. Unold, M. Kicherer, K.J. Ebeling, M. Naritomi, and R. Yoshida, "High performance selectively oxidized VCSEL arrays for Parallel, High-Speed Optical Interconnects", in *ECTC 2000*, Las Vegas, NV, USA, May, 2000, to be presented.

[13] F. Mederer, M. Kicherer, R. Jäger, H. Unold, and K.J. Ebeling, "5 Gbit/s data transmission with single-mode GaAs VCSELs over a 0°C to 80°C temperature range", in *ECOC 2000*, Munich, Germany, Sep., 2000, submitted.

[14] R. Michalzik, R. King, G. Giaretta, R. Jäger, and K.J. Ebeling, "VCSEL arrays for 10 Gb/s multimode fiber optical interconnects", *Optoelectronic Interconnects VII, SPIE Proc.*, vol. 3952, 2000, in press.

[15] R. Michalzik, G. Giaretta, K.W. Goossen, J.A. Walker, and M.C. Nuss, "40 Gb/s coarse WDM data transmission with 825 nm wavelength VCSELs over 320 m of high-performance multimode fiber", in *ECOC 2000*, Munich, Germany, Sep., 2000, submitted.

[16] M. Miller, M. Grabherr, R. Jäger, and K.J. Ebeling, "kW/cm^2 VCSEL array for high power applications", in *Vertical Cavity Surface Emitting Lasers IV, SPIE Proc.*, vol. 3946, San Jose, CA, USA, Jan., 2000, in press.

[17] W. Schmid, F. Eberhard, R. Jäger, R. King, M. Miller, J. Joos, and K.J. Ebeling, "45 % quantum-efficiency light-emitting diodes with radial outcoupling taper", in *Light-Emitting Diodes: Research, Manufacturing, and Applications IV, SPIE Proc.*, vol. 3938, San Jose, CA, USA, Jan., 2000, in press.

[18] V. Schwegler, M. Seyboth, C. Kirchner, M. Scherer, M. Kamp, P. Fischer, J. Christen, and M. Zacharias, "Spatially resolved electroluminescence of InGaN-MQW-LEDs", *MRS Internet J. Nitride Semicond. Res.*, 2000, in press.

[19] V. Schwegler, M. Seyboth, S.S. Schadt, M. Scherer, C. Kirchner, M. Kamp, U. Stempfle, W. Limmer, and R. Sauer, "Temperature distribution in InGaN-MQW LEDs under operation", *MRS Internet J. Nitride Semicond. Res.*, 2000, in press.

[20] P. Unger, "Introduction to power diode lasers Book Chapter in High-Power Diode Lasers–Fundamentals, Technology, Applications", *Applied Physics*, vol. 78, 2000, in press.

[21] H.J. Unold, S.W.Z. Mahmoud, F. Eberhard, R. Jäger, and K.J. Ebeling, "Large-area single-mode selectively oxidized VCSELs: approaches and experimental", in *Vertical Cavity Surface Emitting Lasers IV, SPIE Proc.*, vol. 3946, San Jose, CA, USA, Jan., 2000, in press.

[22] H.J. Unold, S.W.Z. Mahmoud, R. Jäger, M. Kicherer, M.C. Riedl, and K.J. Ebeling, "Improving single-mode VCSEL performance by introducing a long monolithic cavity", *IEEE Photon. Technol. Lett.*, vol. 12, 2000, submitted.

[23] I. Daumiller, C. Kirchner, M. Kamp, K.J. Ebeling J. Off, F. Scholz, and E. Kohn, "Material requirements for high temperature GaN based heterojunction FETs", *Mat. Sci. Eng. B*, 2000, submitted.

[24] I. Daumiller, C. Kirchner, M. Kamp, K.J. Ebeling, L. Pond, C.E. Wetzel, and E. Kohn, "Evaluation of AlGaN/GaN HFETs up to 750 °C", *Electron. Device Lett.*, 2000, submitted.

[25] A. Bramati, J.-P. Hermier, A.Z. Khoury, E. Giacobino, P. Schnitzer, R. Michalzik, K.J. Ebeling, J.P. Poizat, and P. Grangier, "Spatial distribution of the intensity noise of a VCSEL", *Optics Lett.*, 2000, submitted.

[26] T. Ackemann, S. Barland, M. Cara, S. Balle, J.R. Tredicce, R. Jäger, M. Grabherr, M. Miller, and K.J. Ebeling, "Spatial mode structure of bottom-emitting broad-area vertical-cavity surface-emitting lasers", *J. Opt. B: Quantum Semiclass. Opt.*, 2000, in press.

[27] T. Ackemann, S. Barland, M. Giudice, J.R. Tredicce, R. Jäger, M. Grabherr, M. Miller, and K.J. Ebeling, "Spatial structures in vertical-cavity semiconductor amplifiers", in *NOEK 2000*, Marburg, Germany, Apr., 2000, submitted.

[28] P. Fischer, J. Christen, M. Zacharias, V. Schwegler, C. Kirchner, and M. Kamp, "Spatially resolved imaging of the spectral emission characteristic of an InGaN/GaN-MQW-Light-Emitting Diode by scanning electroluminescence microscopy", *Jpn. J. Appl. Phys.*, 2000, in press.

[29] M. Zacharias, P. Fischer, J. Christen, M. Hiramatsu, and M. Kamp, "Scanning photoluminescence and electroluminescence microscopy of semiconductor nanostructures and devices", in *Electrochemical Society Meeting*, Hawaii, 1999.

[30] N. Armani, G. Salviati, C. Zanotti-Fregonara, E. Gombia, M. Albrecht, H.P. Strunk, M. Mayer, M. Kamp, and A. Gasparotto, "Deep level related yellow luminescence in p-type GaN grown by MBE on (0001) sapphire", *MRS Internet J. Nitride Semicond. Res.*, 2000, in press.

[31] C. Affolderbach, A. Nagel, S. Knappe, C. Jung, D. Wiedenmann, and R. Wynands, "Nonlinear spectroscopy with a vertical-cavity surface-emitting laser (VCSEL)", *Appl. Phys. B: Lasers and Optics*, vol. 70, pp. 407–413, 2000.

Jingle Bells

Jingle bells, jingle bells, jingle all the way,
oh what fun it is to ride in a one horse open sleigh.

Laser light, laser light, lasers all the day
Oh what fun it is tonight with the lasers far away.

Beim ersten dicken Run
Glaubte sein Suszeptor dran,
Von Hin Yiu wir berichten
Er wächst jetzt dünne Schichten.

Sechzig wurd sie heuer,
Sie ist uns lieb und teuer.
Ihr wisst schon lang um wen es geht,
von Sophie ist die Red.

Sieben Doktorn gabs dieses Jahr,
Da war er immer da,
Sonst ziehts Joachim häufig fort
Von diesem schönen Ort.

Zum Atemschutz sollt er,
doch war er viel zu schwer,
Nun muss er erst mal fasten
Ohne Plätzchen im Brotkasten.

Sie wurde fünfzig Jahr
Christine ist ja klar.
Ordnung hält nur der,
Dem das Suchen fällt zu schwer.

Frau Menzel darf nicht fehlen
Beim Diplomanden quälen.
Sie lässt sich ungern plagen
Von ihren vielen Fragen.

Montag früh am Morgen,
die Kiddies machen Sorgen,
Drum ruft uns einfach Markus an,
Zur Besprechung er nicht kann.

An seinem Platz steht Max,
Und macht fast einen Satz.
Die Laser leuchten schon,
noch völlig ohne Strom.

Sonst überträgt er Daten,
Mit unerreichten Raten.
Doch unser lieber Server
Bringt Felix nur noch Ärger.

Beim Schichtenwachstum Michas,
Trat Ammoniak aus, man riecht das.
Dass er gar nicht der Täter
Erfuhr er erst viel später.

Sorgen von Irene
Sind häufig neue Pläne:
Was neues für die MBE
Tellur wär das Okay?

Beim Gase Installieren
Kann leicht etwas passieren,
Christoph ist schon berüchtigt
H2 sich leicht verflüchtigt.

Rollo ist der Mann,
Der VCSEL wachsen kann,
Und willst du etwas ordern,
Musst du es bei ihm fordern.

Der Hansi war nicht da
Und Gruhli nahm das wahr,
Das Ätzen viel ihm schwer,
Die CAIBE geht nicht mehr.

Bei Computer mag der Peter
Nur UNIX darauf steht er,
Dafür gibt es auch Vossplot,
Das gibts sonst nur im Ostblock.

Auf unsern langen Fluren
Sieht man so manch Frisuren.
Doch Heiko ist der Superstar:
Stets durchgestyltes Haar.

Wer bisher ohne Reim,
Der möge uns verzeihn.
Es blieb noch viel zu sagen,
Wir dieses nicht mehr tun ...

by M. Seyboth, V. Schwegler, J. Kunze and M. Scherer